Mémoire

Auteur : Lambin, Clara
Promoteur(s) : Fettweis, Xavier
Faculté : Faculté des Sciences
Diplôme : Master en sciences géographiques, orientation global change, à finalité approfondie
Année académique : 2020-2021
URI/URL : http://hdl.handle.net/2268.2/12547

UNIVERSITY OF LIÈGE
Faculty of Science
Geography Department

Impact of spatial resolution on wind speed and long-term wind speed variability in South Greenland using the regional climate model MAR

Author:
Clara LAMBIN

Supervisor:
Xavier FETTWEIS

Examiners:
Aurelia HUBERT-FERRARI
Matthias VANMAERCKE

President of jury:
Aurelia HUBERT-FERRARI

A master thesis submitted in fulfilment of the requirements for the degree of Master in geographic sciences, climatology orientation.

Academic year 2020-2021

September 2021

Abstract

Fighting global warming implies replacing fossil fuels by renewable energy sources. Wind has the benefit to be an easily accessible and infinitely renewable resource but is not evenly distributed in space and time. A solution to prevent energy scarcity in a decarbonised world would be the building of a global interconnected grid that provide populated regions with electricity generated in remote but resourceful areas. In this context, it has appeared that Greenland and Europe have complementary wind regimes. In particular, the southern tip of Greenland, Cape Farewell, has gained increasing interest for wind farm development as it is one of the windiest places on Earth.

However, the development of such wind farms requires a better understanding of the wind field in that area, especially over the tundra. Because it is an observation-scarce country regional climate models are useful tools to study the Greenlandic wind regime. In this thesis, the Modèle Atmosphérique Régional (MAR) was used to model the wind speed over Cape Farewell. The model was first validated over the tundra by comparing its outputs with *in situ* observations obtained from various databases including the stations from the Katabata project put in place by the University of Liège. It was found that the model could fairly represent the wind field. Subsequently, the impact of the spatial resolution on the modelling of wind speed was investigated by running MAR at 5, 10, 15 and 20 km resolution and by comparing the outputs with *in situ* observations. It appeared that the improvement of correlation between the model and the observations was not linear as the resolution increased. This is very likely due to a better resolving of the topography by the model in higher resolutions. The resolution also seemed to have a stronger impact in winter when wind speeds are higher. Finally, the long-term wind speed variability over South Greenland was evaluated by analysing simulations of MAR forced by five CMIP6 models between 1981 and 2020 and under the scenario SSP5-8.5 between 2021 and 2100. No significant wind speed change was found between 1981 and 2020. However, a general decrease in wind speed can be expected between 2021 and 2100 in the area likely due to a reduced katabatic forcing over the ice sheet and a diminution in the meridional temperature gradient strength between the mid-latitudes and the Arctic, both induced by global warming. Yet an increase in wind speed is expected along the ice sheet edges due to stronger barrier winds, enhanced by the stronger temperature gradient between the cold ice sheet and the warmer tundra, again as a consequence of global warming.

Résumé

Lutter contre le réchauffement climatique implique de devoir remplacer les énergies fossiles par des énergies renouvelables. Le vent a pour intérêt d'être une ressource facilement accessible et infiniment exploitable mais n'est pas distribuée partout de la même façon et est variable dans le temps. Une solution pour éviter l'intermittence de la production d'énergie dans un monde décarbonisé serait de construire un réseau global qui fournirait les régions peuplées en électricité produite dans des régions reculées mais au vaste potentiel en énergies renouvelables. Dans ce contexte, il est apparu que le Groenland et l'Europe ont des régimes de vent complémentaires. En particulier, la pointe sud du Groenland, le Cap Farewell, reçoit un intérêt croissant pour le développement de parcs éoliens étant donné que c'est une des régions les plus venteuses du monde.

Cependant, l'installation d'éoliennes au sud du Groenland nécessite une bonne connaissance des champs de vent, particulièrement au-dessus de la toundra. Le pays étant pauvre en données d'observations, l'utilisation d'un modèle climatique régional est un outil précieux pour étudier les vents groenlandais. Dans cette étude, le Modèle Atmosphérique Régional (MAR) a été utilisé pour modéliser les vitesses vent au-dessus du Cap Farewell. Le modèle a, dans un premier temps, été validé au-dessus de la toundra en comparant ses résultats avec des données d'observations provenant de différentes bases de données, dont les stations mises en place par l'Université de Liège dans le cadre de son projet Katabata. Il en résulte que le MAR est en bon accord avec les observations. Ensuite, l'impact de la résolution spatiale sur la modélisation des vitesses de vent a été étudiée en faisant tourner le MAR à 5, 10, 15 et 20 km de résolution et en comparant les résultats avec des données d'observations. Il est apparu que l'amélioration de la corrélation entre le modèle et les observations n'augmente pas de manière linéaire à mesure que la résolution s'affine. Ceci est certainement dû au fait que la topographie est mieux résolue par le modèle à haute résolution. La résolution spatiale semble également avoir un impact plus important en hiver lorsque la vitesse du vent est plus grande. Finalement, la variabilité à long terme de la vitesse du vent au sud du Groenland a été étudiée par l'analyse de simulations du MAR forcé avec cinq modèles du CMIP6 entre 1981 et 2020 et sous le scénario SSP5-8.5 entre 2021 et 2100. Aucun changement significatif de vitesse n'a été trouvé entre 1981 et 2020. Cependant, une diminution générale de la vitesse du vent est attendue entre 2021 et 2100 probablement due à une réduction du forçage catabatique au-dessus de l'inlandsis et une diminution de l'intensité du gradient de température méridional entre les moyennes et les hautes latitudes, tous deux induits par le réchauffement climatique. Au contraire, le long des marges de l'inlandsis, une augmentation de la vitesse des vents est attendue à cause d'un renforcement des vents de barrière, générés par un gradient de température plus fort entre l'inlandsis froide et la toundra plus chaude, encore une fois à cause du réchauffement climatique.

Acknowledgements

First of all, I would like to express my sincere gratitude to my supervisor Xavier Fettweis. I thank him for his constant availability whenever I had questions or needed help with this work and for his precious advice.

Secondly, I would like to thank my classmate Antoine Bosly for helping me with many coding issues I encountered while conducting this work. I also thank him and my other classmate Cyril Wuest for the good atmosphere they put this year in our section.

I would like to give a special thanks to Philippe Wanlin and Suzette Chaidron for their thorough revision of English grammar and spelling and their writing advice.

Finally, I want to thank my friends Gaëlle and Camille for their good advice, Corentin for helping me with R and Elise for always keeping me motivated. I also thank them, my family and other friends Manon, Marleen, Lucas G. and Lucas W. for their encouragements and for cheering me up whenever I needed to be.

Table of Contents

List of abbreviations

ABL	Atmospheric Boundary Layer
a.g.l.	Above ground level
a.s.l.	Above sea level
AWS	Automatic Weather Station
CMIP5	Coupled Model Intercomparison Project Phase 5
CMIP6	Coupled Model Intercomparison Project Phase 6
DMI	Danish Meteorological Institute
ECMWF	European Centre for Medium-Range Weather Forecast
ECS	Effective Climate Sensitivity
ESM	Earth System Model
GCM	Global Climate Model
GrIS	Greenland Ice Sheet
MAR	Modèle Atmosphérique Régional
NAO	North Atlantic Oscillation
NESTOR	Nesting Organization for the Preparation of Meteorological and Surface Fields in Regional Climate Models
NOAA	National Oceanic and Atmospheric Administration
NORLAM	Norwegian Limited Area Model
PROMICE	Program for Monitoring of the Greenland Ice Sheet
Polar MM5	Polar version of the 5th generation of Mesoscale-Model.
RACMO2	Regional Atmospheric Climate Model, version 2
RCM	Regional Climate Model
RCP	Representative Concentration Pathway
RMSE	Root mean square error
RMSEc	Centred root mean square error
SISVAT	Soil Ice Snow Vegetation Atmosphere Transfer
SSP	Shared Socioeconomic Pathway
STD	Standard deviation
ULiège	University of Liège
WCRP	World Climate Research Program
WRF	Weather model for Research and Forecasting

Chapter 1: Introduction

1.1 Context and motivations

Global warming due mainly to anthropogenic emissions of greenhouse gases and the utilisation of fossil fuels is threatening the living conditions of human societies in many ways (IPCC, 2021). The rise of the mean sea level, the thinning of freshwater resources, the increased frequency of heatwaves and droughts are examples of climate change impacts, some of which are already taking place (Hitz and Smith, 2004). In order to prevent those impacts from becoming increasingly severe and frequent, the utilisation of cleaner energy sources needs to be further developed instead of polluting and non-renewable ones.

Although decarbonisation of the energy sector would clearly benefit the environment, some remaining issues need to be tackled. Indeed, infinitely renewable resources such as wind and solar radiation are not equally distributed on the planet and are varying over time. Consequently, if the global energy system was to fully rely on renewables, the intermittency of these resources in some regions would lead to an unreliable electricity supply (Radu et al., 2019). Therefore, the idea of a "global grid" (Chatzivasileiadis et al., 2013), i.e., an interconnected global electric system, would address the problem by linking remote yet resourceful locations with other regions in time of need. It has moreover been demonstrated that long-distance power transmission lines needed for such a "grid" are both technologically feasible and economically efficient (Chatzivasileiadis et al., 2013). By linking regions with complementary resource patterns, the energy supply would be homogenized and more reliable (Radu et al., 2019).

As an example of remote yet resourceful location, Greenland has been shown to have a great potential in terms of wind power harvesting (da Silva Soares, 2016; Jakobsen, 2016). Particularly, its southernmost tip, Cape Farewell, is one of the windiest places on Earth due to the specific action of the island's ice sheet on the synoptic circulation and the presence of katabatic winds (Moore et al., 2015). Moreover, it appears that the wind temporal variability of this region is complementary with European wind temporal variability (Radu et al., 2019). This means that in times of low wind power productivity, especially during summer, Europe could be supplied by Greenlandic wind farms to compensate for this production deficit with the implementation of this so-called global grid.

In this context, an accurate evaluation of the wind speed field is necessary for future wind farm development in South Greenland. Because it is an observation-scarce region, the use of regional climate models (RCMs) is an important tool to perform such an evaluation (Ettema et al., 2010b). However, with a highly complex topography and the presence of numerous fjords, challenges arise when modelling the wind field around Cape Farewell. Although various studies have investigated this question, three modelling gaps have been identified which will be addressed in this study.

Firstly, against this global grid background and the interesting interconnection that could be made between Greenland and Europe to build a reliable energy-supplying system based on wind power, the University of Liège (ULiège) has implemented the Katabata project (https://www.katabata-project.uliege.be/) which aims at increasing the wind field knowledge in the surroundings of Cape Farewell. The Modèle Atmosphérique Régional (MAR) developed at ULiège has been used with a view to modelling at high spatial resolution (5km) the wind field in this area (Radu et al., 2019) and three automatic weather stations were installed there in order to increase the *in situ* 10m-wind observation availability. However, the MAR wind speed outputs have only been validated against this kind of *in situ* measurements in Delhasse et al. (2020) for daily data and only over the Greenland ice sheet (GrIS) at a 15km resolution. The lack of MAR wind speed output validation with stations located in the tundra constitutes the first modelling gap, as wind turbines are unlikely to be installed directly on the GrIS because of its ice flow. Moreover, data from the stations of the Katabata project have not been used by Delhasse et al (2020) as they were not available yet. A validation of the MAR model with hourly data has not yet been made either.

Secondly, although multiple RCMs have been used to study the wind in Greenland, very few studies have investigated the importance of spatial resolution of the model on the variability of the wind speed outputs. This kind of study has been carried out by Du Vivier and Cassano (2013) at low spatial resolutions for offshore circulation and by Jakobsen (2016) (see Section 2.4), but it has never been done with MAR. Because the ice sheet margins have such a complex topography, this question is of great importance. Indeed, topographical features such as fjords, mountains or glacial valleys, which are numerous in the ice-free area of Greenland, can influence the wind speed and are not always resolved by the resolution of the model (Jakobsen, 2016).

Thirdly, because the Arctic is the region experiencing the strongest warming due to climate change (Serreze and Francis, 2006), it is of great interest to investigate the long-term wind speed changes in South Greenland to see how wind speed could be affected by the global warming, which can also be useful knowledge for wind farm development. Temperature increases of +1.7°C in summer and +4.4°C in winter were observed over the island over the period 1991-2019 by Hanna et al. (2021). These temperature trends might influence the atmospheric circulation as well as the local wind effects which might eventually have an impact on the wind speed field (Gorter et al., 2013). However, if wind farms were to be installed around Cape Farewell, it is crucial to know if any wind speed trend might occur in the area as it could impact wind power production.

1.2 Objectives and research questions

The use of RCMs is of great importance to model the wind speed field at the southern tip of Greenland, an observation-scarce region, which is a region with great wind power production potential as shown by the ULiège Katabata project and other studies (Jakobsen, 2016; da Silva Soares, 2016). To address the previously mentioned gaps in the modelling of the South Greenlandic wind speed field, this work aims at answering three research questions:

1) Does MAR accurately represent the wind speed over the tundra in South Greenland?
2) To which extent is the wind speed sensitive to the spatial resolution of MAR?
3) Is there any past observed or future expected wind speed trend in South Greenland?

To tackle these questions, the objectives of this work are thus: 1) to validate MAR over the tundra against hourly *in situ* observations, 2) to compare the wind speed outputs at different spatial resolutions and 3) to investigate the long-term wind speed variability of the study area.

1.3 Thesis outline

Chapter 2 gives a description of the observed wind regime around Cape Farewell and a literature review of previous studies that have been conducted in relation with the objectives of this work. The data and methodology used to tackle the different research questions will then

be presented in Chapters 3 and 4 respectively. Objectives 1 and 2 (see Section 1.3) are combined in the methodological process so that Chapter 4 is divided into two distinct parts: “importance of spatial resolution on wind speed” (Section 4.2), which includes the validation of MAR with *in situ* observations, and “temporal wind speed variability” (Section 4.3) which addresses objective 3 (see Section 1.3). An overview of the MAR model will also be given at the beginning of Chapter 4 (Section 4.1). The results and discussion will subsequently be presented in Chapter 5. Finally, conclusions and perspectives will be given in Chapter 6.

Chapter 2: literature review

2.1 Greenland general context

Greenland is one of the largest islands in the world and its ice sheet is the most extensive body of ice in the Northern Hemisphere (Gorter et al., 2013). It is situated at the boundary between the Atlantic and the Arctic Ocean and its location ranges from 59° to 84° North and from 11° to 74° West (da Silva Soares, 2016; Jakobsen, 2016). It covers an area of $2.2*10^6$ km² out of which $4.1*10^5$ km² (roughly 20%) is ice-free (Jakobsen, 2016). The highest point of Greenland, the Gunnbjørn Fjeld mountain, peaks at 3693 m above sea level (a.s.l.) (da Silva Soares, 2016). This mountain as well as the ice sheet extent, peaking at Summit (3250 m), are shown in Figure 2.1.

The topography of Greenland is very contrasting. While the slopes of the ice sheet are smooth and soft-curved, the coastal ice-free area has been shaped by the action of glaciers and meltwater rivers. The terrain off the ice sheet is thus very complex with features such as mountains (with peaks ranging from 500 to 1500 m a.s.l), fjords, valleys and plenty of small islands along the shore. It is mostly rocky with sparse tundra vegetation. (Jakobsen, 2016)

The climate in Greenland is a polar climate with extreme minimum temperatures. In winter, average temperatures over the Greenland Ice Sheet (GrIS) oscillate around -40°C and can drop to -60°C whereas they can reach -10°C during the warmest months (Przybylak, 2016). Over the ice-free area, temperatures can be relatively milder due to the lower elevation and can exceed 0°C in summer (Przybylak, 2016). While the major part of the country is under the influence of the large-scale Polar Cell, the southern tip of Greenland is influenced by the westerly winds generated by the large-scale Ferrel Cell and the associated synoptic patterns (Jakobsen, 2016). The following Sections give a more detailed overview of the Greenlandic wind regime.

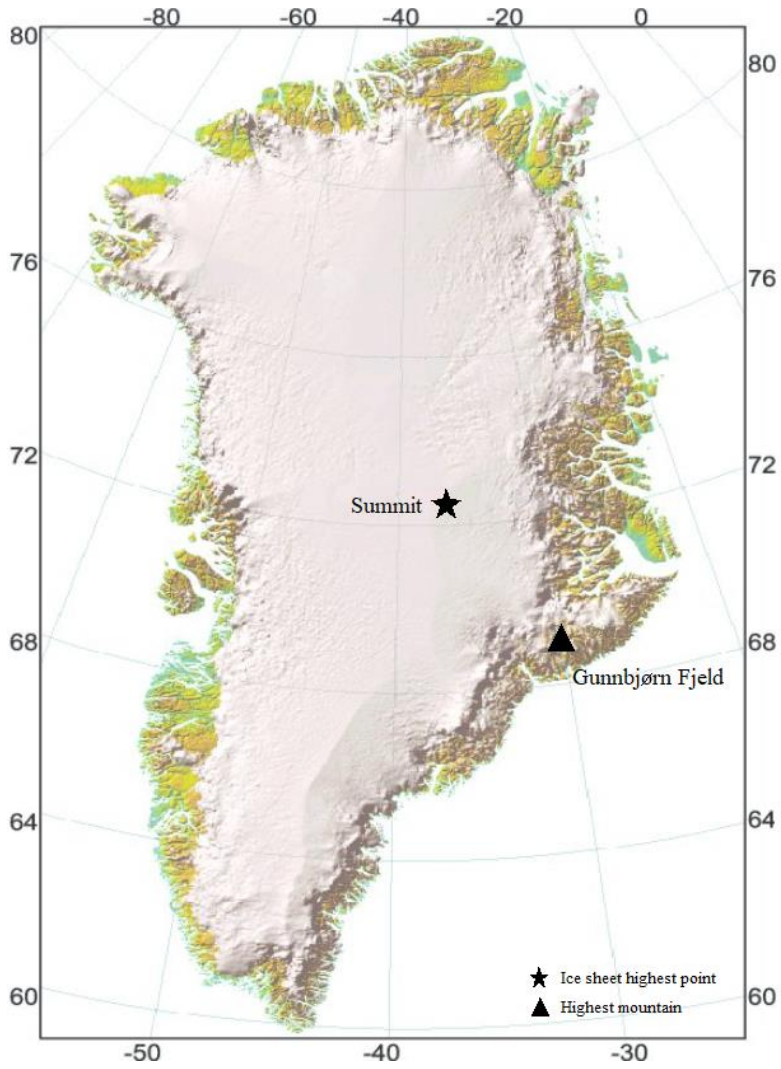

Figure 2.1: *Extent of the Greenland ice sheet. Modified from Guillevic et al. (2013). Numbers at the top and bottom indicate longitude, numbers at the left and right edge indicate latitude.*

.

2.2 Wind in southern Greenland

The observed wind regime in Greenland is a combination of katabatic winds due to the presence of the ice cap and the synoptic circulation influenced by the high topography of the island. Indeed, the very high GrIS acts as a barrier to the geostrophic flow creating high wind speed events that will be further discussed. Moreover, interactions between synoptic atmospheric features and local wind effects can either enhance or reduce the observed wind speed. All these factors explain why the southern part of Greenland is one of the windiest places in the world.

2.2.1 Katabatic winds

Katabatic winds are a common phenomenon over the GrIS (Ettema et al., 2010a; Grachev et al. 2016). Generally speaking, they occur on sloping terrains and result from a negative radiation balance at the surface which causes a downward sensible heat flux from the subjacent air layer as compensation for the radiation deficit (Gorter et al., 2013). The latter is a result of the low heat absorption of the surface in short wave radiation due to its high reflectivity combined with a lack of solar radiation and a relatively higher outgoing emission in long wave radiation (Ettema et al., 2010a; van As et al., 2014). The downward sensible heat flux leads to the cooling of the near-surface air and generates an inversion layer (Gorter et al., 2013). The lowering temperature of the air increases its density and the layer becomes negatively buoyant, creating a horizontal pressure gradient that drives the cooled near-surface air downslope combined with the action of gravity (van den Broeke et al. 1994). Figure 2.2 shows a schematic overview of katabatic winds formation. Over Greenland, the ice sheet cools the relatively warmer overlying air layer by radiative transfer and katabatic winds develop over a large part of it (Radu et al., 2019; Gorter et al., 2013). They are deflected to the right by the Coriolis force while the friction with the surface limits the speed and deviation (Ettema et al., 2010a; Gorter et al., 2013). This results in an anticyclonic quasi-permanent wind pattern above the GrIS that affects the climate of its margins (van den Broeke et al., 1994; Ettema et al., 2010a; Gorter et al., 2013).

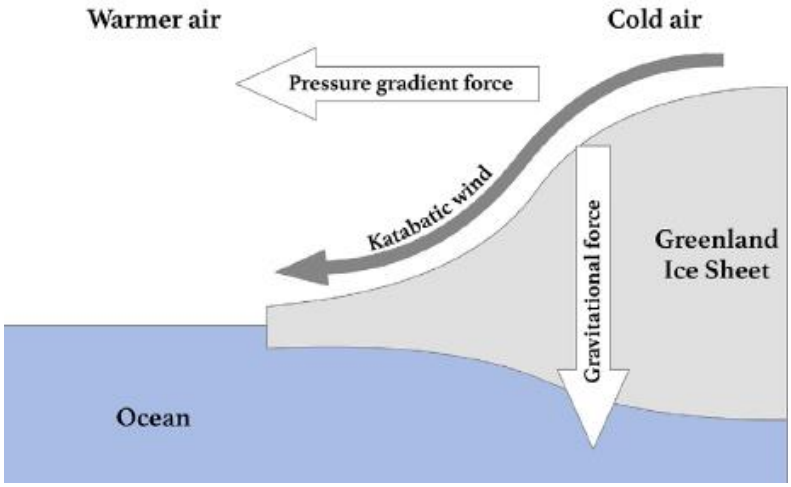

***Figure 2.2**: Illustration of katabatic wind formation from Radu et al. (2019)*

Katabatic winds are characterized by an almost constant direction (considering the deflection by the Coriolis force) and their intensity, as well as the thickness of the katabatic layer, depend on the slope steepness and length, the temperature gradient of the inversion layer and the

surface roughness (van den Broeke et al., 1994; Jakobsen, 2016). They develop in the atmospheric boundary layer (ABL, i.e., the air layer influenced by surface processes), with the inversion layer that can be as high as 400 meters above the GrIS (Radu et al., 2019; Przybylak, 2016). The maximum wind speed of the flow is found close to the surface (Ettema et al., 2010a; Grachev et al., 2016). Over the GrIS, the weakest katabatic winds are found at the top of the ice sheet where the slopes are gentle while the strongest are found near its margins in the ablation zone, especially in the south-eastern coast where slopes are the steepest (Gorter et al., 2013; Jakobsen, 2016). Besides the slope, topography can influence the katabatic winds by channelling the flow which increases its speed. This happens for example in fjords in the coastal area (van de Broeke et al., 1994; Jakobsen, 2016).

On a seasonal basis, katabatic winds are enhanced during the winter when the inversion layer temperature gradient is stronger (Gorter et al., 2013; da Silva Soares, 2016). This is explained by the fact that the cloud cover and solar heating are smaller during this season and enable a more intense radiative cooling of the surface (Ettema et al., 2010b). The cloud cover can in fact minimize the cooling by reflecting the emitted surface radiation backwards (Heinemann and Klein, 2002). In summer, the melting ice in the ablation zone keeps the near-surface air from rising above 0°C, still allowing the katabatic stream to occur by maintaining the inversion temperature gradient (van den Broeke et al., 1994; Ettema et al., 2010a). During this season, the snow-free tundra can influence the flow it receives from the ice sheet edge in different ways. Firstly, when it is daytime, the tundra heats faster than the adjacent ice, reinforcing the horizontal thermal-driven pressure gradient and therefore enhancing the wind speed. Secondly, it can be expected that warmer air is advected from the tundra to the ice sheet above the boundary layer to compensate for the downslope flow. This would strengthen the inversion temperature gradient and increase the buoyancy force thus the wind speed (van de Broeke et al., 1994).

Moreover, when flowing downslope, katabatic winds are adiabatically heated while the air pressure increases with the lowering altitude (van den Broeke et al., 1994; Jakobsen, 2016). In some cases, particularly when the tundra is covered in snow, the temperature of the flow might exceed that of the coastal surroundings. If the air at the ice cap edge is denser than the katabatic layer, the flow will be forced aloft (Jakobsen, 2016). Finally, the change in surface roughness when the air passes from flowing over the ice to the tundra can deflect the wind direction and

slow down the wind speed (van den Broeke et al., 1994; Ettema et al., 2010a). Flow patterns associated with katabatic forcing can thus become quite complex above the tundra.

Over the GrIS, katabatic wind speeds can reach 20 m/s over the strongest slopes (Heinemann and Klein, 2002), while it ranges approximately from 5 to 8 m/s on gentle ice sheet slopes (Gorter et al., 2013). Near the ice sheet margins, the average speed is around 10 m/s (Groter et al., 2013). The speed is weaker over the tundra where the surface slope is lower and the surface roughness is larger (Ettema et al., 2010a). But in cases where katabatic winds are streaming parallel to the synoptic flux, a combination of the flows can occur and lead to high wind speeds events called “piteraq” in local language. Those extreme winds can reach speeds up to 93 m/s as was once registered in Thule (northwest of Greenland) in 1972, making it the third highest wind speed ever recorded worldwide (da Silva Soares, 2016).

2.2.2 Synoptic circulation

The southern part of Greenland is affected by the North Atlantic storm track which brings along low-pressure systems forming around Newfoundland (Canada) towards the Irminger Sea (see Figure 3.1), in the vicinity of Greenland and Iceland, thanks to the Westerlies (Pickart et al., 2008). The Westerlies are westerly winds associated with the Ferrel cell that are deflected to the right by the Coriolis force in the Northern Hemisphere (Jakobsen, 2016). The storms brought by the North Atlantic storm track pass thus in most cases along the south-eastern coast of Greenland, although some might take a different path and enter the Labrador Sea along the south-western coast (Pickart et al., 2008). That is because the track of those lows depends on the position of the Baffin Bay trough which is a mid-troposphere persistent trough resulting from the large-scale Arctic circulation (Mote, 1998). It is an extension of the low-pressure system located in the northern Baffin Bay (Ettema et al., 2010b). If the trough is displaced to the East, the storms will likely take a path along the East coast of Greenland whereas they will flow along the West coast if the trough is displaced westwards (Mote, 1998). The net effect of these passing low-pressure systems is the climatological Icelandic Low that influences the south-eastern part of the country (Ettema et al., 2010b; Gorter et al., 2013). The position of this low is close to the south-eastern coast of Greenland during winter while it shifts closer to the southern coast of Iceland during summer. Its intensity is stronger in winter than in summer (Ettema et al., 2010b). Because Greenland has a very high topography with its thick ice sheet that reaches 3250 m a.s.l. (Jakobsen, 2016), the geostrophic flow associated with the low-pressure systems is blocked and distorted by the orography. This leads to the creation of

mesoscale low-level high wind speed phenomena such as barrier winds and tip jets (Harden and Renfrew, 2012).

2.2.3 Barrier winds and tip jets

Barrier winds are relatively uniform low-level winds that occur when stable air, forced towards the ice sheet by synoptic circulation, cannot rise above the steep topography and is thus deviated parallel to the coast (Gorter et al., 2013). This phenomenon is particularly present along the south-eastern coast of Greenland under the influence of the Icelandic Low (Harden and Renfrew, 2012). Tip jets, as for them, develop through the acceleration of the flow as it passes a promontory. In the vicinity of Cape Farewell, two major types of tip jets are identified based on their dominant direction: the forward (westerly) and the reverse (easterly) tip jet (Moore and Renfrew, 2005). All those wind events have a wind speed maximum located over the ocean but still influence the wind speed over the near coastal regions (Du Vivier and Cassano, 2013). Their associated circulation patterns are shown in Figure 2.3

Forward tip jets are westerly episodic low-level high wind speed events that develop when a low-pressure system is located between Greenland and Iceland (Du Vivier and Cassano, 2013). As for reverse tip jets, they occur when the parent cyclone is located south of Cape Farewell (Du Vivier and Cassano, 2013). The spatial scale of these tip jets ranges from 200 to 400 km (Moore, 2014) and their maximum wind speed, as well as that of barrier winds, can reach 45 m/s (Du Vivier and Cassano, 2013). Their lifetime, however, is relatively short, up to three days in a row for forward tip jets (Pickart et al., 2008). These high wind speed events occur on average once a week during winter (Harden and Renfrew, 2012).

As mentioned above, when barrier winds are formed along Greenlandic coasts, the air is dammed at the edge of the ice cap and forced to flow around it, generating a barrier-perpendicular pressure gradient to build up and an acceleration of the flow (Harden and Renfrew, 2012). When the air reaches the end of the barrier, the pressure rapidly decreases as the air is no longer constrained by the landmass and a new steep pressure gradient that will accelerate the flow is created, this time parallel to the barrier (Harden and Renfrew, 2012). This results in the formation of the abovementioned reverse tip jets that will further be deviated to the right by the Coriolis force, which increases with the wind speed (Harden and Renfrew, 2012).

Concerning the forward tip jets, their formation seems to be linked to the acceleration of the flow through its distortion as it curves when flowing around Cape Farewell (Moore and Renfrew, 2005). Doyle and Shapiro (1999) suggested a second mechanism where the synoptic flow encroaches on the tip of Greenland and is accelerated while moving downslope in order to conserve its Bernoulli function (in a fluid, the sum of pressure, kinetic and potential energy is a constant). Both mechanisms are involved in the formation of forward tip jets but the first one seems to be preponderant (Pickart et al., 2008).

In summer, barrier winds are enhanced by the temperature contrast between the tundra and the ice sheet. During this season, the tundra is heated by the absorption of solar radiation while the ice in the ablation zone is kept at 0°C. This results in a horizontal temperature gradient perpendicular to the GrIS edge (van den Broeke and Gallée, 1996). If the flow is directed from the ice sheet towards the tundra (for example when the wind regime is purely katabatic), the gradient is weakened because the tundra is cooled by the cold air advection. On the contrary, if the synoptic flow advects warm tundra air towards the GrIS, the temperature gradient is strengthened because the ice temperature cannot rise above melting point (van den Broeke and Gallée, 1996). To better understand the influence of the gradient on the formation of barrier winds, van den Broeke and Gallée (1996) explained this phenomenon as follows: if we consider that at the top of the ABL the geostrophic wind (V_g) is directed towards the GrIS, the horizontal temperature gradient is then strong, as explained previously. Therefore, it acquires a strong thermal wind component V_t based on the following relation:

$$\frac{\partial v_g}{\partial z} = \frac{g}{fT}\frac{\partial \theta}{\partial x} \quad (1)$$

Where T is the temperature at a given altitude, g is the gravity, f is the Coriolis parameter, x is the distance component perpendicular to the ice sheet and θ is the potential temperature. The potential temperature is defined as the temperature of an air layer adiabatically brought down to the 1000 hPa pressure level. This variable is useful to compare air layers that are located at different elevations (Gorter et al., 2013). The thermal wind is the vectorial difference between two geostrophic winds at two different altitudes ($V_t = \frac{\partial v_g}{\partial z}$). Considering equation (1), the geostrophic wind at the surface is found to be deviated from the one at the top of the ABL. If we take into account the enhanced deviation of the surface wind owing to the surface roughness and the presence of the topographic barrier, the real surface wind is found to be parallel to the ice sheet edge (van den Broeke and Gallée, 1996). The summer barrier winds are thus stronger

thanks to the temperature gradient between the tundra and the ice sheet than barrier winds caused by orographic deviation only (van den Broeke and Gallée, 1996).

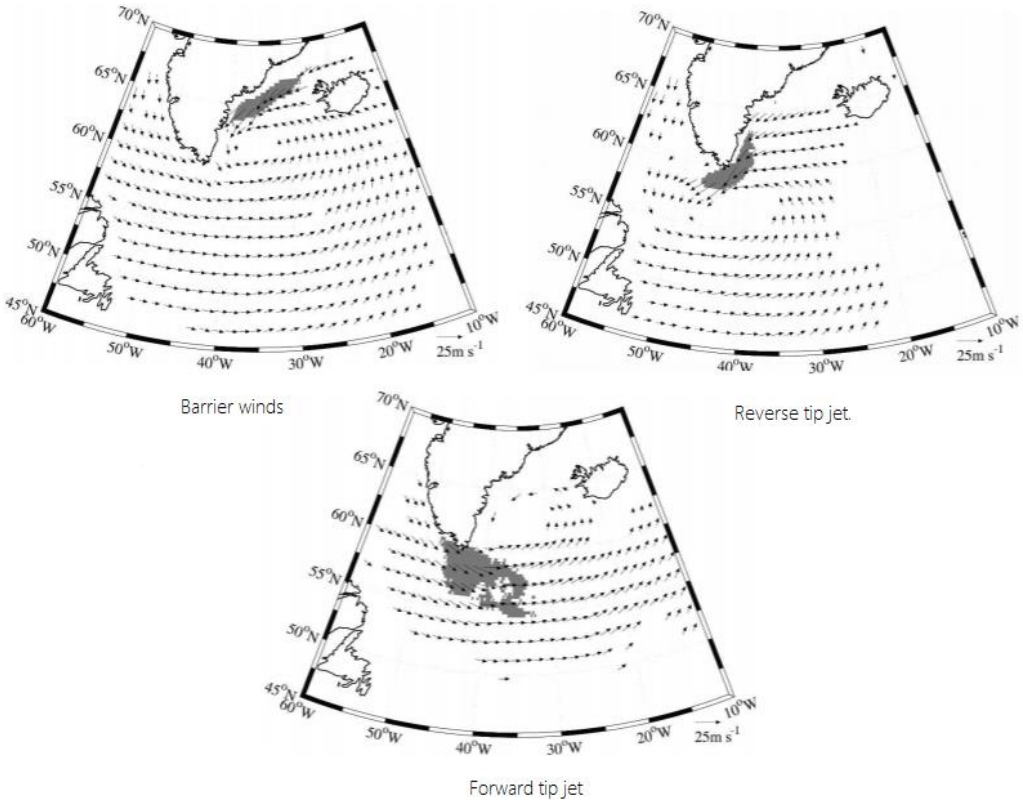

***Figure 2.3**: Barrier wind, forward and reverse tip jets, from Moore and Renfrew (2005). Composite image of the 10 m wind of 1999-2004 winter months (December-January-February). The wind vectors represent the 99% statistically significant circulation. The shading represents the areas where the wind speed is in excess of 15 ms^{-1}.*

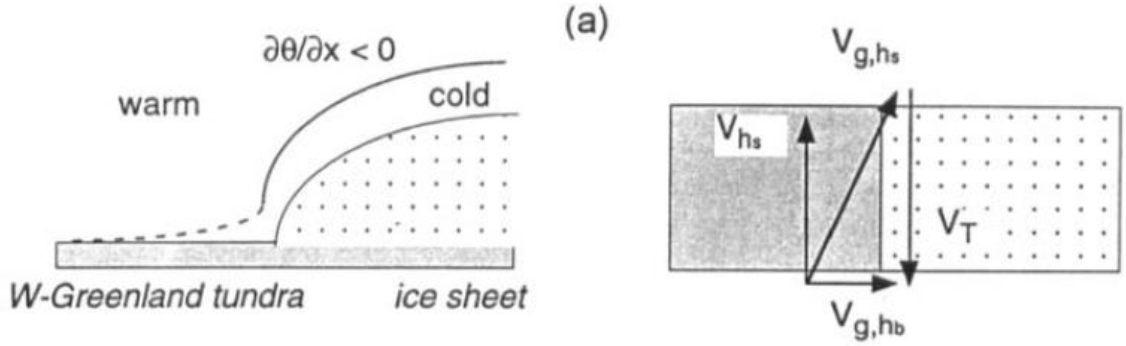

***Figure 2.4:** Illustration of summer barrier barrier in Greenland where $V_{g,hs}$ is the geostrophic wind at the surface, $V_{g,hb}$ is the geostrophic wind at the top of the ABL, V_T is the thermal wind and V_{hs} is the real wind at the surface (van den Broeke and Gallée, 1996)*

2.3 Wind variability

On a seasonal basis, winds in southern Greenland are stronger in winter than in summer. As seen in Section 2.2.1, katabatic winds are stronger during this season thanks to a highly developed temperature inversion layer. The frequency of cyclones passing over the area is also higher during winter (Przybylak, 2016) leading to potentially more recurrent barrier and tip jets events. That is due to the fact that the polar vortex is stronger in winter, moving the North Atlantic storm track further to the North than in summer (Jakobsen, 2016). In summer, a lower katabatic forcing and a lower frequency of cyclones that generate tip jets and barrier winds explain the slower observed wind speeds in South Greenland.

In terms of interannual variability, it has been shown that the frequency of tip jets and barrier winds is linked to the North Atlantic Oscillation (NAO) index (Harden et al., 2011). The NAO index can roughly be defined as the pressure difference between the Azores Anticyclone and the Icelandic Low, meaning that cyclonic activity is more intense in the North Atlantic Ocean with positive NAO values (Laurila et al., 2021). When the NAO is high, this leads to a higher occurrence of more intense passing cyclones over the region. Laurila et al. (2021) analysed the present-day wind speed trend over Greenland and its surroundings over the 1979-2018 period using the ERA-5 reanalysis data (see Section 3.3 for more details about ERA-5). They found no significant wind speed trend over that period except a high interdecadal variability driven by the NAO.

Finally, it can be expected that over the GrIS, the wind speed will tend to decrease with climate change (Gorter et al., 2013). Indeed, katabatic forcing should be reduced over the ice sheet due to a smaller radiation deficit at the surface, except in summer over the ablation zone where the near-surface air is kept at 0°C by the melting ice while the upper air layer would experience a temperature increase, reinforcing the temperature inversion gradient of the ABL. As for the ice cap margins, they might experience a wind speed increase and stronger summer barrier winds (Franco et al., 2013). This would be due to the fact that the temperature contrast between the tundra and the ice sheet would be reinforced, creating a stronger pressure gradient between the two areas, and thus enhance the thermal forcing of the winds over the ice-free area (Franco et al., 2013).

Adding to this reduction in katabatic forcing, Jung and Schindler (2019) predicted a general decrease in mean wind speed over the Northern Hemisphere by the end of the 21st century. This decrease might be explained by the fact that due to global warming, the meridional temperature gradient between the poles and the mid-latitudes driving the large-scale wind speed in the Northern Hemisphere is predicted to be reduced (Jung and Schindler, 2019). This is because the Arctic is expected to warm faster than the lower latitudes due the ice-albedo feedback (Serreze and Francis, 2006). With rising temperatures, a decrease in the sea-ice and snow cover extent give way to more heat absorbing surfaces leading to a warming amplification (Serreze and Francis, 2006). This phenomenon is also known under the name "Arctic Amplification" (Serreze and Francis, 2006).

2.4 Wind modelling history in southern Greenland

This section gives a literature review of recent studies about the use of RCM in the evaluation of the Greenlandic wind climate and their findings about the importance of spatial resolution for modelling accuracy, together with a literature review about the use of these models to study the long-term wind speed trends and future changes in Greenland.

Concerning mesoscale modelling of wind speed in Greenland, multiple studies using different RCMs such as Polar MM5 (Polar version of the 5th generation Mesoscale Model) (Bromwich et al., 2001), RACMO2 (Regional Atmospheric Climate Model, version 2) (Ettema et al., 2010a, Ettema et al. 2010b; Gorter et al., 2013 ; da Silva Soares, 2016), WRF (Weather model for Research and Forecasting) (Du Vivier and Cassano, 2013; Jakobsen, 2016) and NORLAM (Norwegian Limited Area Model) (Heinemann and Klein, 2002) have been conducted to evaluate the near-surface wind regime at different spatial resolutions and time scales. As for MAR, although it has already been used over Greenland in multiple studies and has been proven to be well suited for polar climates (Franco et al., 2013, 2016; Hanna et al., 2021; Payne et al., 2021) and to accurately simulate the GrIS surface mass balance and surface melt (Fettweis et al., 2006, 2017; Fettweis, 2007; Tedesco and Fettweis, 2020), its wind speed outputs have seldom been studied. Radu et al. (2019) used it for data retrieval in order to compare the wind resource complementarity between Greenland and Europe as already mentioned in Section 1.1. In their study (see Figure 2.5), MAR was run over the southern tip of Greenland at a resolution of 5 km over the period 2008-2017, forced with the ERA-5

reanalysis (see Section 3.3). However, the MAR wind speed outputs have only been validated against *in situ* observations in Antarctica by Gallée et al. (2013) and in Greenland by Delhasse et al (2020). Gallée et al. (2013) have used MAR to simulate the snow erosion by wind in Antarctica over the Adélie Land, at a spatial resolution of 5 km. In that region, the model seemed to have a good wind speed behaviour when compared with observation data. But in contrast to Greenland, Antarctica does not have a tundra with highly complex topography as it almost entirely covered by its ice sheet. As discussed in Section 1.1, Delhasse et al. (2020) performed this evaluation at a 15 km resolution only above the GrIS which has a very different terrain from the adjacent tundra.

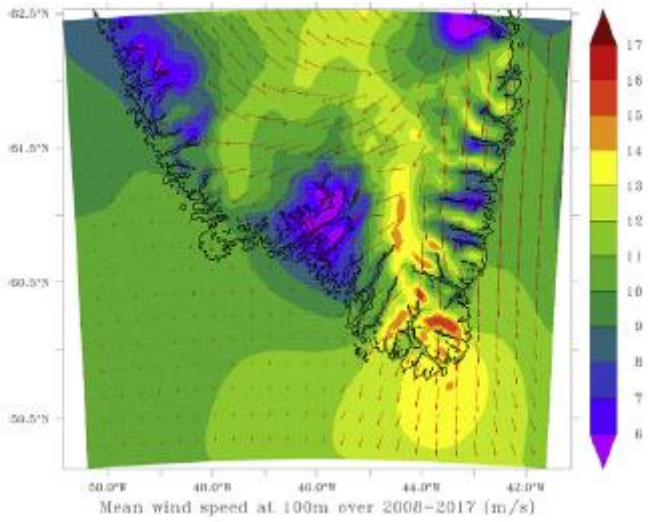

Figure 2.5 *Results of wind speed modelling with the MAR at a 5 km resolution from Radu et al. (2019). The results show the mean wind speed 100 m above ground over the period 2008-2017. Wind speed maxima can be identified where katabatic winds add up to the synoptic flow.*

Regarding the above-mentioned previous studies of wind speed in Greenland, it appeared that medium-coarse spatial resolutions (such as 40 km with Polar MM5) were sufficient enough to accurately model the katabatic winds over the relatively homogeneous ice sheet surface, except on the steep slopes of the ablation zone (Bromwich et al., 2001). However, much finer resolutions were needed to accurately model the wind speed in the complex ice sheet margins, where small scale topography features are present and can affect the wind flow, and to represent high wind speed events such as barrier winds and tip jets (Du Vivier and Cassano, 2013; Ettema et al., 2010a; Jakobsen, 2016). In their study, Du Vivier and Cassano (2013) compared WRF simulations of high wind speed events over southern Greenland and the adjacent Irminger Sea

at spatial resolutions of 10, 25, 50 and 100 km with case studies of satellite-observed tip jets and barrier winds. They showed that spatial resolutions of 50 and 100 km were too poor in the representation of those events, while high resolutions of 10 and 25 km had good and similar results in terms of wind speed. As a matter of fact, the smoothed topography and smaller slope gradients of the low resolutions did not have a sufficient blocking effect on the synoptic flow to generate a realistic pressure gradient build-up and the associated barrier and tip jets high wind speeds (Du Vivier and Cassano, 2013).

Furthermore, with the use of the RACMO2 model over the whole Greenland, Ettema et al. (2010)a and Gorter et al. (2013) concluded that the spatial resolution of 11 km gave satisfying results, although it could not precisely resolve the topography of the GrIS edges. At this resolution, the smoothing of the relief could still be a slight source of errors (Ettema et al., 2010a). Finally, Jakobsen (2016) used the WRF model in non-hydrostatic mode (in contrast to this study where MAR is run in hydrostatic mode, see section 4.1 for more details) in a 2 km resolution nested domain over Cape Farewell for January 2009. He concluded that for highly precise modelling purposes, which is not the case in this study, this resolution still showed errors due, again, to the smoothing of the topography by the model, although the results were consistent with the observed data. Nevertheless, he judged that mesoscale modelling still has a high potential in wind power resources assessment by giving a detailed view of the general wind pattern in this area.

Additionally, only a few studies have evaluated the long-term temporal variability of wind speed in Greenland (Gorter et al., 2013; Laurila et al., 2021; Jung and Schindler, 2019). Gorter et al. (2013) is the only known study to have used a mesoscale model (RACMO2) to simulate future wind speeds over the whole GrIS by downscaling the global climate model (GCM) HadGEM2, using the RCP4.5 scenario of the CMIP5, which corresponds to a medium-range scenario of radiative forcing according to van Vuuren et al. (2011).

This state-of-the-art review shows that there is a need for further investigations regarding mesoscale modelling of the wind speed in Greenland. Firstly, using MAR in this study and validating its results over the tundra with observation data (see Section 4.2) would allow us to have better knowledge about the ability of the ULiège model to simulate wind in southern Greenland, where the Katabata project has been carried out. Secondly, the above-mentioned previous studies have shown the importance of spatial resolution in the wind speed modelling

over this region. This confirms the interest of modelling the wind speed at different high spatial resolutions to evaluate the sensitivity of the modelled results to spatial resolution (see further Section 4.2). Finally, the lack of studies on the long-term wind speed variability over Greenland highlights the necessity to further evaluate the potential future wind speed changes due to global warming and the associated Arctic Amplification.

Chapter 3: Data and study area

This Chapter shows the data that were used to investigate the different objectives of this study. First, the study area, consistent for each part of the methodology is presented, followed by detailed explanations about the observation data used to validate MAR. Then, an overview of ERA-5 reanalysis and Earth System Model (ESM) outputs that have been used to force MAR (see Chapter 4) will be given.

3.1 Delimitation of the study area

The area of interest in this study is the southern tip of Greenland, Cape Farewell. As seen in the previous Chapter, it is one of the windiest places on Earth as a consequence of a combination of katabatic winds from the GrIS and local effects such as barrier winds and tip jets. The selected area is located between 59.5° and 64.5° North and between 40° and 52° West. Figures 3.1 and 3.2 show the location of the study area.

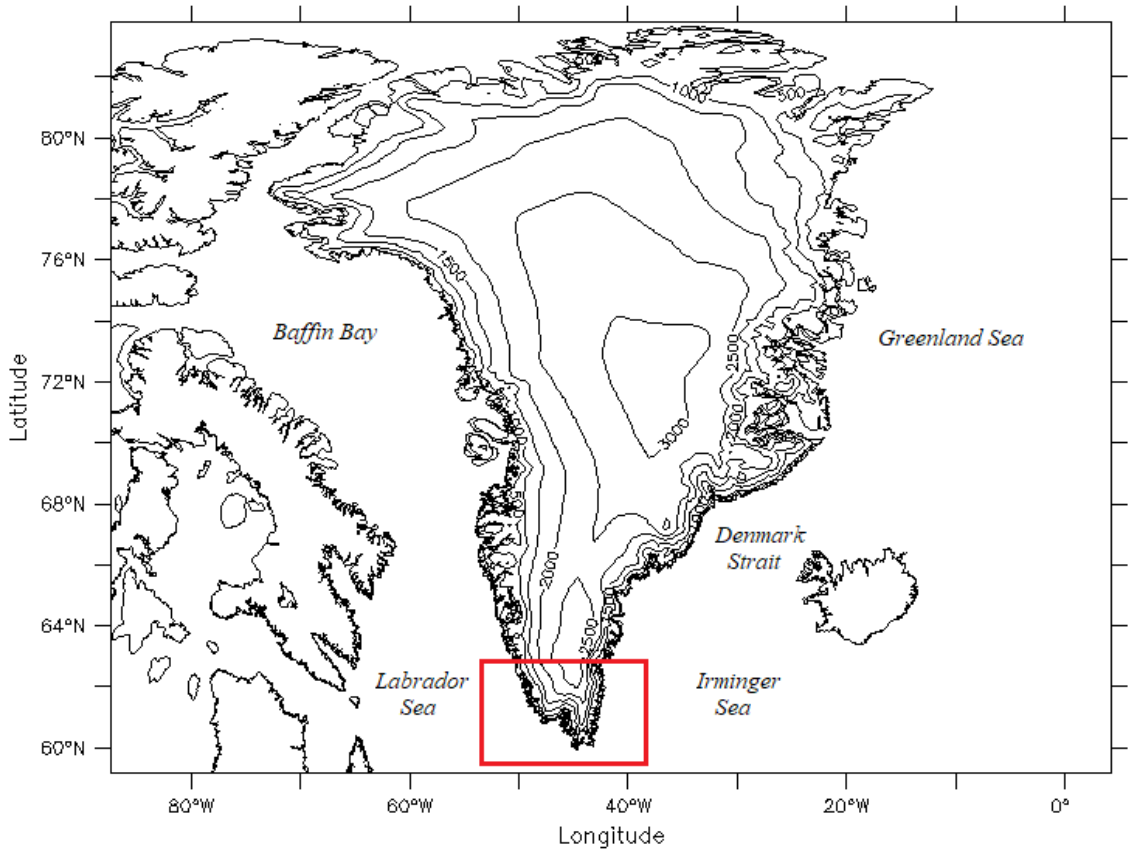

Figure 3.1: *Map of Greenland and surrounding seas. The red box represents the area of interest. Contour lines (height in meters) are only represented for Greenland.*

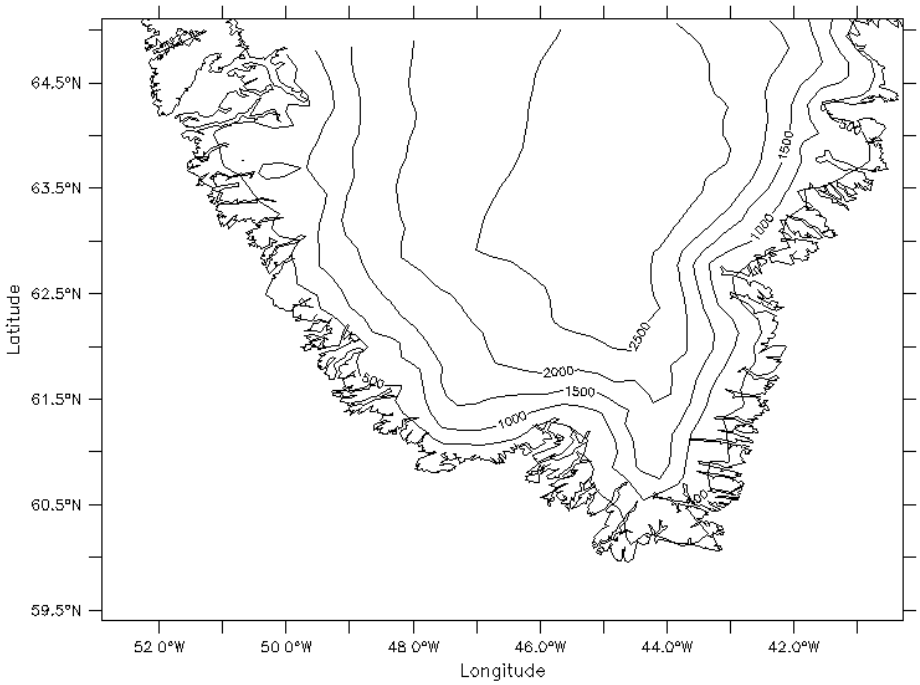

Figure 3.2: *Area of interest: land borders and contour lines (height in m). Zoom of the red box in Figure 3.1.*

3.2 Observation Data

The observation data used in this study are *in situ* measurements obtained from multiple weather stations located in the study area. This data will be used in Section 4.2 of the methodology, in the assessment of the spatial resolution importance on the MAR wind speed outputs and their validation. Two datasets were obtained. The first one, which will be referenced to as the reference dataset, comes from three different databases: the Program for Monitoring of the Greenland Ice Sheet (PROMICE), the Danish Meteorological Institute (DMI) and the National Oceanic and Atmospheric Administration (NOAA). The second dataset comes from the three Katabata project weather stations. These are described in the following sections.

3.2.1 Reference dataset

Data from this section are hourly wind speed values from 01/01/2016 00:00 to 31/12/2018 23:00 UTC. This time period was chosen because it had the most complete datasets from the selected weather stations. A total of 10 stations from the PROMICE, DMI and NOAA databases contribute to this dataset.

3.2.1.1 PROMICE

The PROMICE data were collected from three automatic weather stations (AWSs) situated in the study area, namely QAS_L, QAS_M and QAS_U. These stations are located on the southernmost part of the Greenland ice sheet in the ablation area (see Figure 3.3). They are all located relatively close to each other but at different elevations (see Table 3.1). The AWSs measure a series of variables including horizontal wind speed, sensor height and GPS location. The instrument used to measure wind speed (in ms^{-1}) is a wind monitor manufactured by R.M. Young, model 05103-5 (Fausto and van As, 2019). The climatic variables are measured every ten minutes and are thereafter transmitted as hourly averages. The GPS data, as for them, are recorded every 6 hours (Fausto and van As, 2019). The data used in this Chapter are the third version of the hourly datasets of the above-mentioned stations for the years 2016, 2017 and 2018, except for QAS_M which has only been active since 11/08/2016 and which had a very incomplete dataset for the year 2017. Therefore, only the 2018 dataset was used for this station. The data were downloaded on 10/11/2020 from https://promice.org/PromiceDataPortal/api/download/f24019f7-d586-4465-8181-d4965421e6eb/v03/hourly/csv . These stations were used by Delhasse et al (2020) to validate MAR above the GrIS but the authors used daily mean instead of hourly observations such as in this study.

Because the stations are located on the edge of the ice sheet where snowfall accumulation is high, the height above the surface at which the variables are measured is variable, as the base of the station is gradually buried under snow during winter. Theoretically, the height measured by the height sensor would be 3.1 m if the station were not to sink into the snow. The wind monitor measures the wind speed 0.4 m above height sensor (Fausto and van As, 2019). Furthermore, the position of the stations is not perfectly constant because they are driven by the flow of the ice on which they stand. Additionally, the stations might be moved or levelled during spring maintenance visits which might lead to height fluctuations for some data as well (Fausto and van As, 2019). Finally, because of the very high wind speed events that can occur in the southern part of Greenland, it may happen that stations fall on the ground, resulting in missing or erroneous data (Fausto and van As, 2019).

3.2.1.2 DMI

Six stations from the DMI weather stations network were used in this study, namely Angisoq (ANG), Ikerasassuaq (IKS), Ikeramiuarssuk (IKM), Narsarsuaq Radiosonde (NAR), Nunarsuit (NUN) and Ukiviik (UKI) which are all located in the tundra surrounding the GrIS. Their

coordinates as well as elevation are listed in Table 3.1. When looking at their location on Google Earth Pro, stations ANG, IKS and UKI are all located on small islands a few kilometres off the coasts. Station IKM is located along the coast at the mouth of a fjord while station NAR, is located in the inner land at the foot of a glacier valley. As for NUN station, a lack in coordinate precision locates it in the middle of the ocean, approximately 15 km away from the coast. However, this unprecise location should not be a problem in the further analysis (when looking for the corresponding MAR pixel, see Section 4.2.3) considering that its real location is probably along the coast facing the open ocean and no topographic obstacle that could potentially alter the wind speed value is present between the likely real location and the given location. It should be noted that only the IKS station is mapped in Google Earth Pro, all other stations are not visible.

These stations record climatic variables, including horizontal wind speed, automatically as well and are transmitted as raw data, which means they do not undergo any quality check or other procedure (DMI, 2021a). Typical sources of errors in the datasets are due to wear and tear of the measuring instruments or to exposure to extreme weather events. Nevertheless, maintenance visits are regularly performed to avoid instrument degradation (DMI, 2021a). Concerning the wind speed, it is measured at a height of 10 m above ground level (a.g.l.) for every station in meters per second, recorded every 10 minutes (DMI, 2021b). The chosen parameter was hourly mean of wind speed. The datasets in the chosen time period were available for 2016, 2017 and 2018 for stations ANG, IKM, NUN and UKI, 2016 and 2017 for station IKS and were only available for year 2018 for station NAR. Those can be downloaded on https://dmiapi.govcloud.dk/, in the “metObs” service. It should be noted that by the time this study was conducted, the available version of the datasets was version 1 of metObs. Since then, version 1 has been depreciated and version 2 is now available.

All the DMI data used in this study can also be found on the NOAA downloading site: https://www.ncei.noaa.gov/access/search/data-search/global-hourly?pageNum=4 (accessed on 16/12/2020) where they are accompanied by a quality check index but where station coordinates are less precise than the ones given on the DMI site. Anyway, the quality check index, which will be further discussed in the next section, has been reviewed for the DMI data and it appeared that all non-missing data were of good quality except one or two values which were thus removed from the datasets.

3.2.1.3 NOAA

Only one station from the NOAA weather station network (except those corresponding to DMI stations discussed in the previous section) was present in the study area. This station, which is the anemometer of the Paamiut Aerodrome, is located on the south-western coast of Greenland and is referred to as Fredickhab station (FRE) (such is this station's name in the NOAA database). Its coordinates and elevation are also listed in Table 3.1. It should be noted that the coordinates given by NOAA are imprecise for this station. Indeed, the station appears to be standing in the water when checking for its position on Google Earth Pro. Fortunately, its real position can be checked on https://aim.naviair.dk/ (consulted on 10/07/2021), where a plan of the aerodrome as well as the position of the anemometer can be found. Table 3.1 shows the coordinates of the FRE station replaced in Google Earth based on the information from Naviair.dk.

Data from the NOAA stations network comes from the Integrated Surface Data (ISD) database. In the yearly station datasets, the wind speed is expressed in meters per second and is multiplied by a factor ten. The associated quality code takes the following values:

0=passed gross limits checks
1=passed all quality control checks
2=suspect
3=erroneous (NOAA, 2018)

When checking for the quality of the data (as done for DMI stations as well, see previous section), it appeared that the vast majority of non-missing data had a quality code of 1. Only one or two values per dataset were qualified as "suspect" and were thus removed. For further analysis purposes, the wind speed in the FRE datasets were scaled to a factor 1.

3.2.1.4 Station locations

The locations of the stations for which the observation data has been described in the previous sections are shown in Figure 3.3 and their coordinates as well as elevation is listed in the following Table:

***Table 3.1**: weather stations characteristics. Longitude and latitude are expressed in decimal degrees. Position of PROMICE stations last updated in 2020 (https://promice.org/PromiceDataPortal/).*

Abbreviation	Station name	Longitude	Latitude	Elevation (m)	Database
ANG	Angisoq	-45.1461	59.9911	14	DMI
FRE	Fredickshab	-49.6761	62.0166	19	NOAA
IKM	Ikeramiuarsuk	-42.0678	61.9364	40	DMI
IKS	Ikerasassuaq	-43.1653	60.0553	88	DMI
NAR	Narsarsuaq	-45.4400	61.1575	3.9	DMI
NUN	Nunarsuit	-48.4544	60.7636	31	DMI
QAS_L	QAS_L	-46.8493	61.0308	280	PROMICE
QAS_M	QAS_M	-46.8330	61.0998	630	PROMICE
QAS_U	QAS_U	-46.8195	61.1753	900	PROMICE
UKI	Ukiivik	-50,4058	62,5789	20	DMI

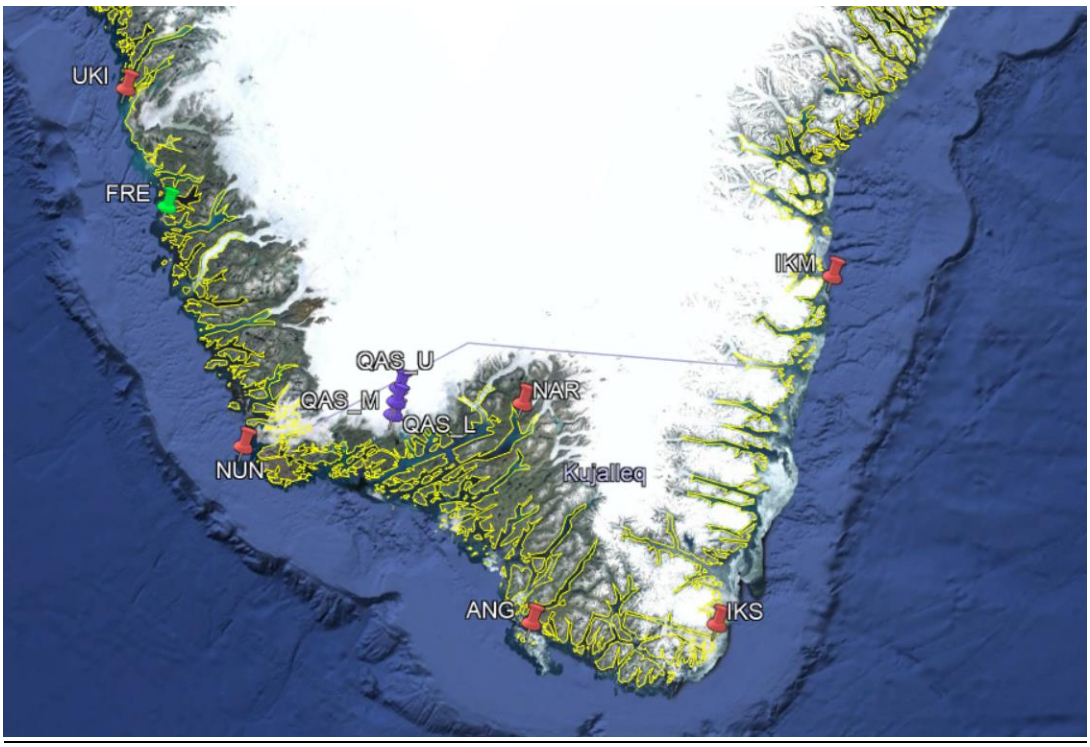

***Figure 3.3**: Location of the stations: red markers represent DMI stations, blue markers represent PROMICE stations and the green marker represents the NOAA station. (Source of image: Google Earth Pro)*

3.2.2 Katabata dataset

3.2.2.1 Katabata

Stations from this section are part of the Katabata project, developed and conducted by Dr. Xavier Fettweis and Prof. Damien Ernst from ULiège, which aims at increasing the availability of *in situ* observations of katabatic winds at the southern tip of Greenland. In contrast to the existing stations from villages and airports which are located in areas relatively sheltered from the wind, the Katabata stations have been established so as to be located directly in front of the prevailing winds, where previous test simulations of the MAR model have identified wind speed maxima (see Figure 2.5). Observation data are thus less influenced by topographic effects that might alter the wind speed. In total, three AWS of the Finnish brand Vaisala have been installed in September 2020 in the southern tundra of Greenland by Michaël Fonder (ULiège) and his team. The stations collect temperature, humidity and wind speed values 10 m above ground, which are transmitted every 20 minutes by satellite connexion. The stations are still running at the beginning of August 2021 but have experienced multiple failures in the meantime resolved thanks to a visit of the 3 stations in July 2021. The dataset used in this study includes the observation data of these three Katabata AWS from September 2020 to December 2020.

3.2.2.2 Stations location

Two out of the three Katabata AWS have been installed on non-mountainous small islands which are ice-free during the summer. The third one is located in a glacial valley. The station coordinates are listed in Table 3.2 and Figure 3.4 shows their location. To avoid confusion with other AWS in this study, they have been renamed as listed in Table 3.2.

***Table 3.2**: coordinates of the Katabata Stations. Latitudes and longitudes are found on https://www.katabata-project.uliege.be/, elevations have been checked on Opentopomap.org*

Station	Name in this study	Longitude	Latitude	Elevation (m)
AWS 6640	KAT_6640	-45.1799167	59.9842222	36
AWS 0460	KAT_0460	-45.0676944	60.1566667	76
AWS 0680	KAT_0680	-44.0622500	60.1833056	11

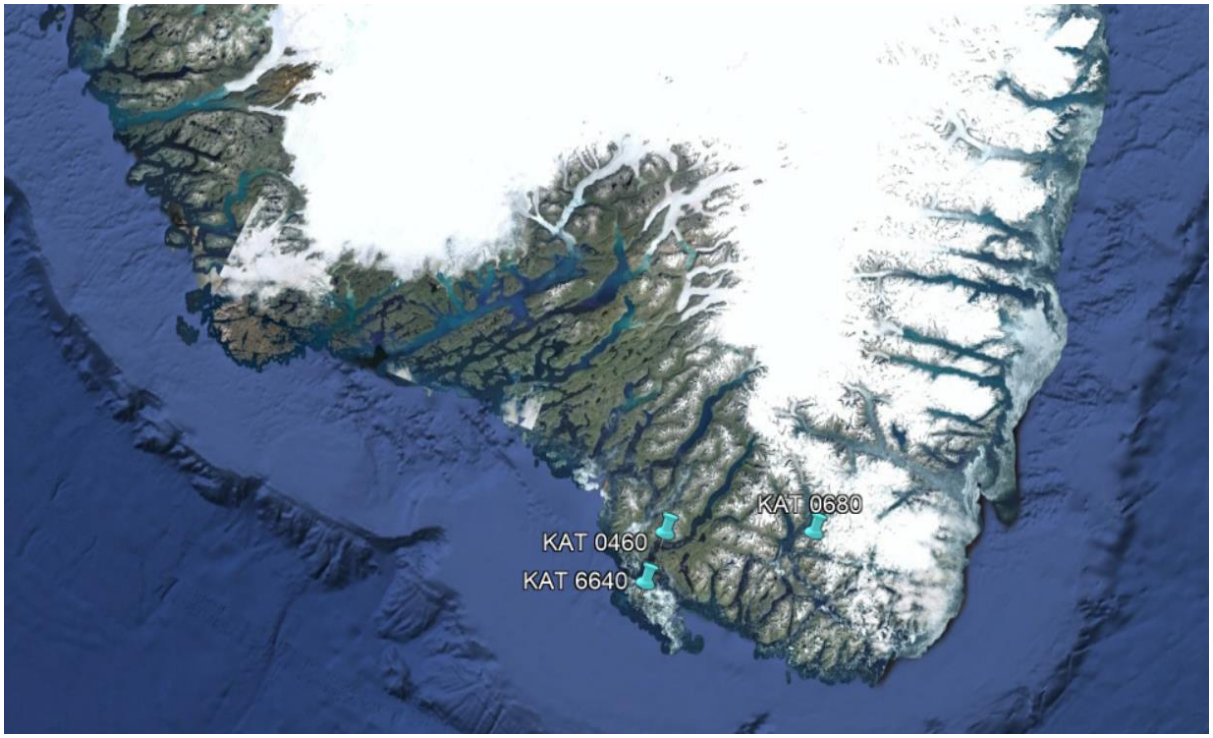

***Figure 3.4**: Location of the Katabata stations: stations are represented by the light blue markers. (Source: Google Earth Pro)*

3.3 ERA-5 Reanalysis

Atmospheric reanalyses are GCM (such as the one used by IPCC) in which observed meteorological data obtained from various sources (such as weather stations, satellites, buoys, etc.) are assimilated every 6 h in order to generate outputs that physically depict the historical 3D state of the atmosphere (Soares et al., 2020). This has the advantage of giving homogeneous (as data are based on the same model) and continuous information about the entire Earth's surface and its different atmospheric layers, in contrast to observation data which can be limited in space and time. Several climatological and surface variables are evaluated in reanalyses, including temperature, wind speed, and atmospheric pressure (Olauson et al., 2018) and obviously, the accuracy of a reanalysis is better in regions with a higher availability of observation data. (Reanalysis.org, 2010)

Reanalyses are often used in climate modelling, especially when using a RCM, to prescribe the initial conditions of the model and to force every 6 h its boundary conditions (see Section 4.1). In this study, ERA-5, the 5th generation of global atmospheric reanalysis produced by the European Centre of Medium-Range Weather Forecasts (ECMFW), will be used to force MAR.

In contrast to its predecessors ERA-40 and ERA-Interim, ERA-5 has finer spatial resolution (31 km compared with 80 km for ERA-Interim), hourly output and more vertical layers (137 extending from surface to 0.01 hPa pressure level) thanks to the use of an improved version of the ECMWF Integrated Forecast System model (IFS 41r2) (Soares et al., 2020). The ERA-5 products, which are updated every three months, are currently available from 1950 to a couple of days before the current date. The ERA-5 reanalysis uses a reduced Gaussian grid, which means that the number of grid points vary with the latitude to keep the separation distance between two points relatively constant (Olauson et al., 2018). A detailed description of the ERA-5 configuration can be found in Hersbach et al. (2018).

Studies have shown that ERA-5 is better suited for the estimation of wind patterns and wind power resources due to its increased temporal and spatial resolution (Olauson et al., 2018; Soares et al., 2020). In addition to the fact that it shows better performance than its predecessors, the ERA-5 reanalysis seems to be the best choice to force initial and boundary conditions of MAR (Delhasse et al, 2020).

3.4 ESM outputs

Another method to force initial and boundary conditions of a RCM is the use of ESM outputs. These are GCM, such as the one used to build ERA-5 but without any assimilation of the data, aimed at producing global outputs at coarse resolution which are a 3D representation of the Earth system close to the average climate. Their forcing into a RCM works in the same way as with reanalyses and they can be used to make climate projections. In this study, ESM outputs from the World Climate Research Program's (WCRP) Coupled Model Intercomparison Project Phase 6 (CMIP6) will be used to perform future projection with MAR. CMIP6's main purpose is to "coordinate the design and distribution of global climate model simulations of the past, present and future climate" (Eyring et al., 2016). One of its activities is to provide multi-model global projections of future climate under different development and greenhouse gas emissions scenarios [Scenario Model Intercomparison Project (ScenarioMIP)] (O'Neill et al., 2016). The CMIP6 scenarios are a combination of the new Shared Socioeconomic Pathways (SSPs) and forcing pathways similar to the Representative Concentration Pathways (RCP) that were previously used as scenarios in the CMIP5 projections (O'Neill et al., 2016). The SSPs explore five different societal development alternatives. For example, SSP1 and SSP5 predict a well-

developed world by 2100 with the difference that SSP1 is based on a sustainable economy and energy sector while SSP5 relies on a fossil fuel intensive power system (O'Neill et al., 2016). These SSPs can then be associated with a radiative forcing pathway as long as this pathway is compatible with the SSP scenario. Here, scenario SSP5-8.5 was chosen, which means that SSP5 was associated with a radiative forcing of 8.5 Wm^{-2} by 2100. This scenario can be considered as an updated version of the RCP8.5 scenario of CMIP5, which was the scenario with the highest radiative forcing by 2100 (Hanna et al., 2021). CMIP6 projection scenarios start in 2015 and end in 2100, in contrast to those of CMIP5 which started in 2006 (O'Neill et al., 2016). Over 1950-2014, the Historical scenario representing the observed climate is used.

To evaluate future wind speed changes in southern Greenland, MAR will be forced with an ensemble of model outputs from CMIP6 (see Section 4.3.1). The ESMs are the following: CESM2, CNRM-ESM2-1, CNRM-CM6-1, UKESM1-0-LL and MRI-ESM2-0 as in Hanna et al. (2021) and Hofer et al. (2020). The first four models are among the CMIP6 models that have the highest Effective Climate Sensitivity (ECS) (Payne et al., 2021). ECS is an estimation of the mean temperature increase at equilibrium if the carbon dioxide concentration of the atmosphere was doubled in the model (Meehl et al., 2020; Payne et al., 2021). The five selected models have an ECS of 5.2°C, 4.8°C, 4.8°C, 5.3°C and 3.2°C respectively (Meehl et al., 2020). The general range of ECS in CMIP6 models varies from 1.8°C to 5.6°C (Meehl et al., 2020). Selecting the "worst-case" scenario of global warming and models with a relatively high ECS will allow us to estimate to what extent the wind speed field of South Greenland can vary with climate change and give an idea to wind farm companies of what they should expect if they invest in the region.

Chapter 4: Methodology

4.1. The MAR model

4.1.1. Overview

The Modèle Atmosphérique Régional (MAR) is a RCM especially designed for polar regions. It was created by Dr. Hubert Gallée from the University of Louvain-la-Neuve and is now being updated by the ULiège. It has extensively been used over Greenland, particularly in the evaluation of the surface mass balance of the ice sheet (Fettweis et al., 2006, 2017; Fettweis, 2007; Franco et al., 2013, 2016; Tedesco and Fettweis, 2020). MAR is a 3D atmosphere-snowpack model coupled with the 1D SISVAT scheme (Soil Ice Snow Vegetation Atmosphere Transfer) which allows the modelling of surface processes (Gallée et al., 2013, Fettweis et al., 2017). A full description of the atmospheric part of MAR can be found in Gallée and Schayes (1994), who used it to simulate katabatic winds over the Antarctic ice sheet, and in Gallée (1995). The SISVAT scheme is described in De Ridder and Gallée (1998) and in Gallée et al. (2001). A summary of the different modules and schemes used in MAR can be found in Fettweis et al. (2017). The general scheme of MAR is illustrated in Figure 4.1.

The primitive equations of the atmospheric dynamics are resolved by the model following the hydrostatic approximation (Gallée et al., 2013). This approximation is valid as long as the model's resolution is not finer than 5 km, meaning that the scale of the vertical circulation is negligible compared with the horizontal circulation scale (Gallée et al., 2013). The vertical coordinate system is a normalized pressure system, where the pressure at a given point (σ) is given by:

$$\sigma = p - p_t / p_s - p_t \qquad (2)$$

where p is the pressure at a given altitude, p_t is the pressure at the top of the modelled atmosphere and p_s is the surface pressure (Gallée and Shayes, 1994). Because pressure decreases exponentially with height, the layers of the σ-coordinate system are thinner near the surface for a constant σ interval which leads to more precise results in the lower troposphere. MAR can then interpolate its outputs at given altitudes a.g.l. in m, which have to be specified in the model set up. In total, the model consists of 24 vertical layers, with the first layer being at 2 m above the surface.

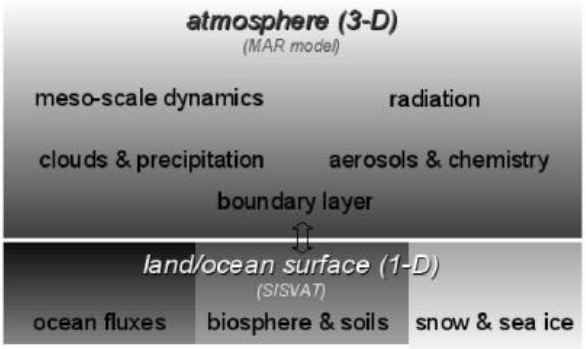

***Figure 4.1**: MAR general description (Fettweis, 2006).*

4.1.2. Model initialisation

RCMs need to have their initial and boundary conditions specified in order to run properly. In this study, these conditions have been forced at a 6 h interval in the version 3.11 of MAR by the ERA-5 reanalysis in the comparison with *in situ* observations and in the version 3.9 of MAR by ESM outputs in the future projections (ERA-5 and ESMs will be hereafter referred to as large-scale models). For initial conditions, every grid cell of the 3D model's domain is forced by large-scale model values. For boundary conditions, the relaxation zone (i.e. the boundary region between the large-scale model and the RCM) consists of a 7-pixel band at the edge of the MAR domain. This is the zone where temperature, wind and humidity fields are forced every 6 hours at each vertical level. Because the topography is a lot more smoothed in the large-scale models due to their huge spatial resolution, in contrast to MAR, the boundary region is considered to be a 15-pixel band to take into account this transition when evaluating the outputs. Only the results from grid cells outside of this border area will be examined hereafter. Finally, the sea surface temperature (SST) and ice-cover above the ocean are also prescribed every 6 h over the MAR ocean grid cells at its surface level.

In addition to lateral forcing, MAR includes an upper-air relaxation zone above 10 km a.s.l. This zone consists in a vertical succession of stratospheric layers in which temperature and wind fields from large-scale models are forced over their entire horizontal extent. In this study, the number of layers in the upper-air relaxation zone has been set to 4, which is the default number. This upper-air relaxation zone is important for the model to account for the interannual variability resolved by the large-scale models (van den Berg and Medley, 2016).

To initialize the domain, the model's grid is built by NESTOR (Nesting Organization for the Preparation of Meteorological and Surface Fields in Regional Climate Models), the pre-processor of MAR, which then interpolates atmospheric data from large-scale models or reanalysis onto the MAR grid and compiles surface data such as vegetation type and topography of the study area. The model configuration used for the different simulations will be detailed in the respective sections of the methodology, namely Sections 4.2.1 and 4.3.1.

4.2. Part 1: Impact of the spatial resolution on wind speed

4.2.1. MAR simulations

In order to study the influence of the resolution on the MAR wind speed outputs, several simulations over the study area were conducted, from 2016 to 2018 and 2020 at a resolution of 5, 10, 15 and 20 km. The 4 different domains are shown in Figure 4.2. It was made sure that the area in which the weather stations are located is at least 15 pixels away from the edges of the MAR integration domain. The domain size and time step were adapted to the model's resolution (see Table 4.1), as the time step at which MAR resolves the primitive equations has to be adapted to the resolution so that in the given time interval, a given particle of the flow should not be able to entirely cross a grid cell (Xavier Fettweis, personal communication).

To compare the outputs with the observation data, the wind speed was simulated at levels of 2 and 10 m of altitude above ground. An elevation of 2 m has been chosen to be compared with the PROMICE data because, taking into account the height variations of AWS measurements, it seemed to be a good compromise. Indeed, although it can vary through the year from 0 to 3.5 m due to previously cited factors (see Section 3.2.1.1), the yearly average height a.g.l. of the PROMICE sensors is close to 2 m. Subsequently, the level of 10 m has been chosen because it can directly be compared with DMI, NOAA and Katabata observation data which were recorded at this same height.

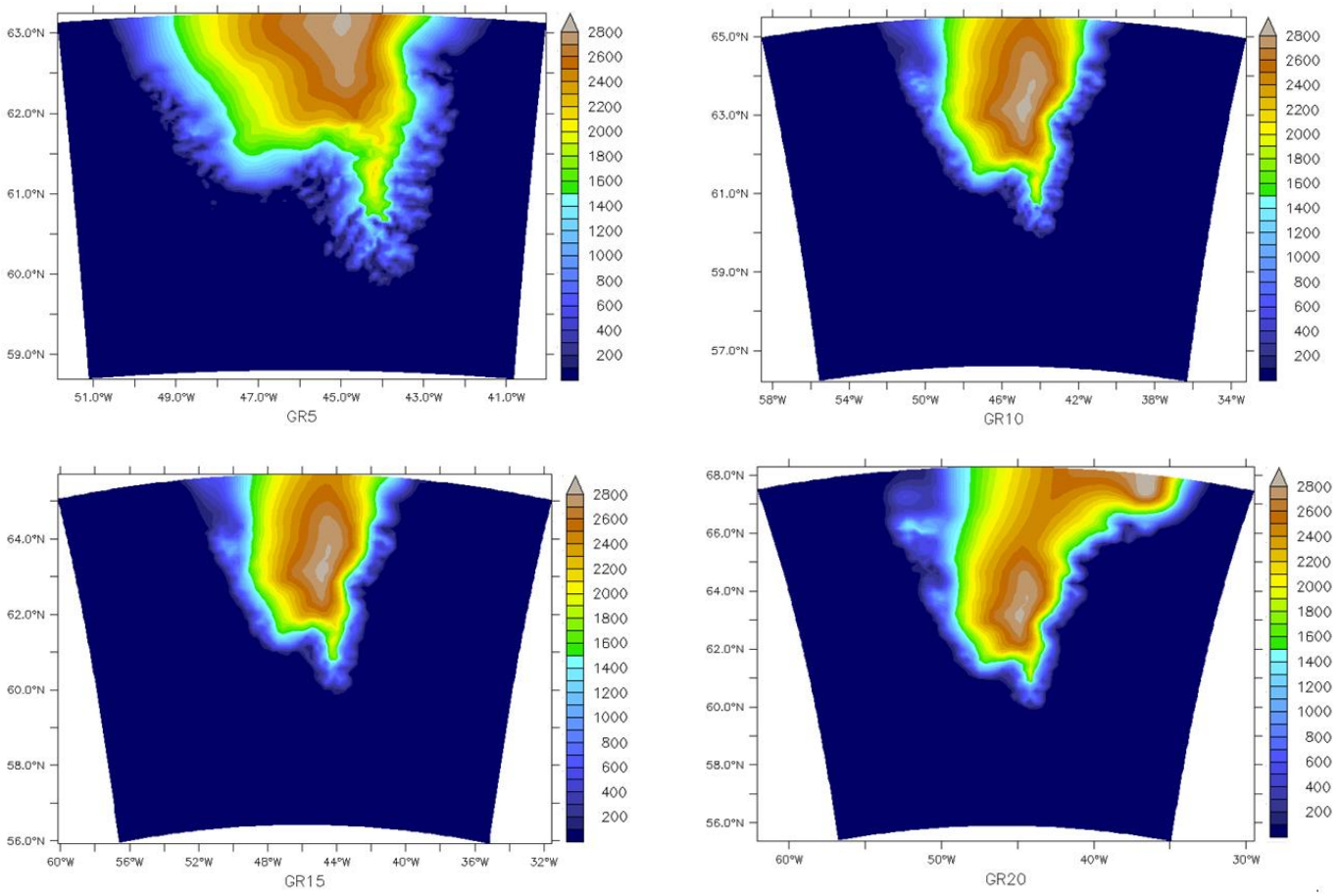

***Figure 4.2**: MAR integration domains at resolution of 5, 10, 15 and 20 km and topography (m).*

***Table 4.1:** Domain size and time step according to the spatial resolution of the model*

Name of the domain	Spatial resolution (km)	Number of grid cells (X-axis)	Number of grid cells (Y-axis)	Time step (s)
GR5	5	120	100	30
GR10	10	120	100	60
GR15	15	90	70	90
GR20	20	70	70	120

For each domain, three simulations were run to be compared with the reference dataset (see Section 3.2.1). The first one started on 1st December, 2015, at 00h00 and ended on 31st August, 2016, at 23h00. The second one was run from 1st December, 2016, 00h00 to 31st August, 2017, 23h00. The last one started on 1st December, 2017, at 00h00 and ended on 31st August, 2018, at 23h00. The first month of each simulation is considered as spin-up, i.e., the time needed by the model to relax from its initial conditions. The simulations were ended in August because

only the winter months (January, February, March) and the summer months (June, July, August) were compared with the *in situ* observations from the reference dataset. This choice has been made because the wind speed is minimal in summer and maximal in winter so these seasons are the most interesting to focus on. The results of these 12 simulations were hourly outputs.

For the Katabata stations, one simulation was run for each domain starting on 1st August, 2020, at 00h00 and ending on 31st December, 2020, at 23h00. The first month is also considered as spin-up time and the model's results were hourly outputs as well. The comparison between MAR and observation data from the Katabata dataset will be made for the months of September, October, November and December 2020 which were the months with the available data at the time this study was conducted.

4.2.2 Data processing

The next step in this part of the methodology was to remove outliers from observation data. As a matter of fact, as stations can fall down (especially PROMICE AWSs located on the ice sheet and Katabata stations, located on the tundra) or there can be trouble with sensors (such as icing), it is not impossible to have data that at first-hand look normal in the raw dataset but are in fact erroneous. To do so, the observation data were first compared with the MAR data. Although a quality check was run for some stations (see Section 3.2.1), the same procedure was applied to every station regardless of this check to facilitate the results comparison.

For each time step (here 1 hour), the difference between MAR and the station observation was calculated (missing values were excluded from this procedure). Because the GR5 domain is supposed to be the most precise, only the MAR datasets from this domain were used to be compared with those from the stations. Then, the MAR vs observations differences were classified and the 95th centile threshold was calculated for each station, for each season (for the reference dataset) of each year (2016-2018 for the reference dataset, 2020 for the Katabata dataset). Finally, all the observations for which the difference with MAR was greater than the threshold were removed from the dataset and can thus be referred to as missing values along with the true missing values.

Subsequently, a 3-hour moving average was applied over both the MAR time series and the considered observation datasets. The average was calculated on three time steps with a weight of 2 attributed to the central time step. It should be noted that for the observation datasets, the moving average was only applied for timesteps where data at *t-1*, *t* and *t+1* were not missing. If a non-missing data did not respond to the condition, its value was kept unchanged.

This removal of outliers and moving average allow to reduce the noise in the datasets. Therefore, the comparison between the different domains and the observation data is easier to assess because with less noise, the information contained within the signal will be more visible.

4.2.3 Search for the nearest pixel

To compare the observation data with the MAR results, the nearest pixel to each station had to be found for each MAR domain. To do so, the horizontal distance between the station location and the centre of each pixel was calculated. Then, for each station and domain, all pixels which were located at a distance shorter than the pixel resolution were compared and the pixel with the closest altitude to that of the station was kept. Although, depending on the domain resolution, the elevation difference might be high for some stations, it is more important to have an accurate position of the corresponding pixel rather than having a precise altitude in view of the spatial variability of wind. Moreover, as the topography of the MAR domain gets coarser with the decreasing resolution, it is expected to have larger altitude differences between stations and their MAR corresponding pixel with decreasing resolution. Additionally, because the elevation of a pixel is the mean altitude of the zone it covers, the discrepancies might be enhanced if the station is located in a topographic feature that is different from the rest of the pixel area, such as a fjord or a valley.

4.2.4 Comparison MAR-observations

Once the corresponding pixel of each station has been found for each domain, the data simulated by MAR were extracted from these pixels to be compared with the *in situ* corrected observations. Only the non-missing observation values were kept along with their corresponding MAR value. For each season of each year (2016, 2017, 2018), the correlation, root mean square error (RMSE), centred root mean square error (RMSEc) and mean bias have been calculated between the observation data and MAR for the reference dataset. The same has

been done for the Katabata stations for September-December 2020. An intercomparison of the results has then been made in section 5.1.

4.3 Part 2: Temporal variability of the wind speed over 1981-2100

4.3.1 MAR simulations

In this section, a first simulation has been run on domain GR20 (see Section 4.2.1) from 1981 to 2020 with daily outputs and one month of spin up (December 1980). This domain has been chosen because it demands less computer time than those with finer resolutions. The MAR model was also forced by the ERA-5 reanalysis. This simulation aims to see if any general wind speed change has been observed during the last 40 years and to evaluate the wind power production trend over this corresponding period. As wind power production also depends on the air density, this simulation (listed in Table 4.3) gives the air density and wind speed at 100 m a.g.l., which is a relevant hub height elevation (Soares, 2020).

To evaluate future wind speed trends, MAR, version 3.9, was forced by five ESMs (see Section 3.4) from 1950 to 2100 at a 15 km resolution over the whole Greenland. The simulations made from Hofer et al. (2020) have been used here. The time step was set at 90 seconds, such as with GR15 (see Section 4.2.1). MAR, version 3.9 as well, was also forced by ERA-5 as reference to compare the results over the 1981-2020 period before comparing the trends over the 2021-2100 period. From these simulations, the results were extracted over the study area, from 1981 to 2020 for MAR forced with ERA-5 and from 2021 to 2100 for MAR forced by the ESMs. The wind speed was available at 100 m a.g.l. but unfortunately, the air density was not simulated.

Figure 4.3 shows the domain over which these simulations were run as well as the area over which the results were extracted. Table 4.2 lists the characteristics of the domain and the extraction area. Table 4.3 lists a summary of all the different simulations used in this part of the methodology. It should be noted that as specified in Section 3.4, the Historical scenario used in the ESMs ends in 2014. However, the simulations that cover the 1981-2020 period will be hereafter referenced to as “historical” for convenience, although their outputs are under the scenario SSP5-8.5 from 2015 to 2020.

***Table 4.2**: Domain used for the simulations of MAR forced by ESMs and ERA-5 at a 15 km resolution. EGR-CUT is the area over which results were extracted from EGR.*

Name of the Domain	Spatial resolution (km)	Number of grid cells (X-axis) *	Number of grid cells (Y-axis) *	Time step (s)	Region
EGR	15	96	179	90	Whole Greenland
EGR-CUT	15	41	40	90	Cape Farewell

*Without boundary region

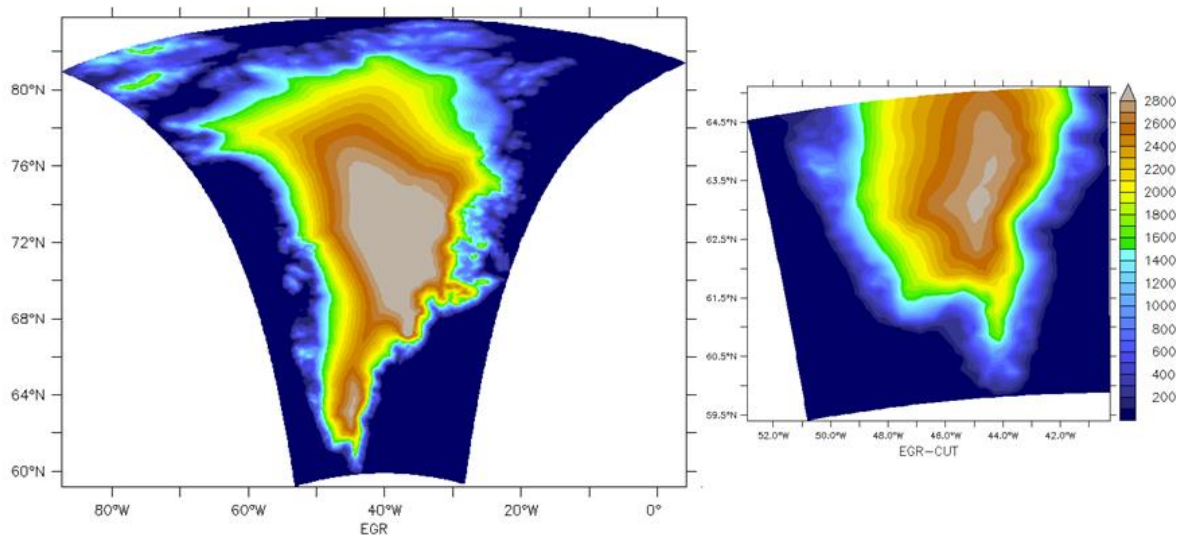

***Figure 4.3** EGR domain and EGR-CUT, extent (boundary region not shown) and topography (m).*

***Table 4.3**: MAR simulations summary*

Name	Forcing	Domain	Period	Variables of interest	MAR version
M-E5-v3.11	ERA-5	GR20	1981-2020	wind speed, air density	3.11
M-E5-v3.9	ERA-5	EGR-CUT	1981-2020	wind speed	3.9
M-CE-hist	CESM2	EGR-CUT	1981-2020	wind speed	3.9
M-CE-ssp585	CESM2	EGR-CUT	2021-2100	wind speed	3.9
M-CC-hist	CNRM-CM6-1	EGR-CUT	1981-2020	wind speed	3.9
M-CC-ssp585	CNRM-CM6-1	EGR-CUT	2021-2100	wind speed	3.9
M-CM-hist	CNRM-ESM2-1	EGR-CUT	1981-2020	wind speed	3.9
M-CM-ssp585	CNRM-ESM2-1	EGR-CUT	2021-2100	wind speed	3.9
M-UK-hist	UKESM1-0-LL	EGR-CUT	1981-2020	wind speed	3.9
M-UK-ssp585	UKESM1-0-LL	EGR-CUT	2021-2100	wind speed	3.9
M-MRI-hist	MRI-ESM2-0	EGR-CUT	1981-2020	wind speed	3.9
M-MRI-ssp585	MRI-ESM2-0	EGR-CUT	2021-2100	wind speed	3.9

4.3.2 Data processing

In order to calculate the wind speed changes, the daily outputs of all the simulations listed in Table 4.3 had first to be converted into monthly means in order to compute yearly and seasonal means. Summer means include the months of June, July and August while winter means include the months of January, February and March. All these calculations have been done in the Ferret software. It should be noted that ESMs do not use the same calendar. CESM2 has a calendar without leap years, CNRM-CM6-1, CNRM-ESM2-1 and MRI-ESM2-0 have a calendar with leap years and UKESM1-0-LL has a calendar of 360 days where all months have 30 days. The monthly means have thus been calculated accordingly.

4.3.3 Data distribution evaluation

Before calculating the wind speed trends, an evaluation of the data probabilistic distribution was conducted. It is important to do so because significance tests can depend on it and because the wind speed is one of the few climatological variables that is not normally distributed, at

least for hourly and daily averaged data. For the latter, the wind speed distribution is very likely to be asymmetrical, as in the Weibull distribution (Bilir et al., 2015). Moreover, the wind speed distribution has not yet been studied on a seasonal and a yearly basis. Therefore, three simulations were used to investigate this question: M-E5-v3.9, M-MRI-hist and M-CE-hist. The two Historical ESM-forced simulations have been randomly selected. A Shapiro-Wilk normality test was applied on the time series from 3 randomly selected pixels, using the yearly and seasonal means. It should be noted that as the Shapiro-Wilk test is not recommended for samples with more than 50 observations (Ghasemi and Zahediasl, 2012), it was not applied on the monthly mean samples (where n=480). Indeed, on large samples, the null hypothesis is very likely to be rejected even if the deviation from normality is small (Ghasemi and Zahediasl, 2012). Instead, the normality of the monthly means distributions was described thanks to the calculation of their skewness and kurtosis.

The Shapiro-Wilk normality test evaluates the correlation between an observed sample and a theoretical sample derived from a normally distributed population that have the same mean and standard deviation (STD) (Ghasemi and Zahediasl, 2012). The samples have to be sorted in ascending order (Güner et al., 2009). The null hypothesis, i.e., the sample follows a normal distribution, is tested with the *W* statistic, calculated as follows:

$$W = \frac{(\Sigma_i a_i y_i)^2}{\Sigma_i (y_i - \bar{y})^2} \quad (3)$$

Where *y* is the element number *i* of the observed sample, $\bar{y}$ is the observed sample mean and *a* is the coefficient of the element number *i* of the observed sample (Güner et al., 2009). Coefficients *a* are calculated thanks to a linear regression between the observed sampled values and the values of the theoretical normally distributed sample sorted in ascending order (Güner et al., 2009). The Shapiro-Wilk test has been conducted in R software using the function "shapiro.test()". This function gives back the value of the *W* statistic and its associated p-value. If the p-value is lower than 0.05, the null hypothesis is rejected with a 95% confidence level and it can be assumed that the sample is not normally distributed.

The skewness is a measure of the asymmetry of a given distribution. A positive skewness indicates that the sample's histogram is right-tailed while a negative skewness indicates that it is left-tailed. A skewness equal to zero indicates perfect symmetry (Perron and Sura, 2013). On the other hand, the kurtosis is an indicator of the distribution shape. If the latter is Gaussian, its

kurtosis is equal to 3. A kurtosis higher than 3 indicates that the distribution has a higher peak near the mean than normal while a kurtosis below 3 indicates a more flattened frequency curve (Perron and Sura, 2013). These parameters were also calculated in R software using the functions “skewness()” and “kurtosis()” from the “moments” library. Mathematically, they are calculated as follows:

$$s = \frac{\sqrt{n(n-1)}}{n-2} \frac{\frac{1}{n}\Sigma_i (x_i - \bar{x})^3}{\left(\frac{1}{n}\Sigma_i (x_i - \bar{x})^2\right)^{3/2}} \quad (4)$$

$$k = \frac{n(n+1)(n-1)}{(n-2)(n-3)} \frac{\Sigma_i (x_i - \bar{x})^4}{(\Sigma_i (x_i - \bar{x})^2)^2} \quad (5)$$

Where *s* is the skewness, *k* is the kurtosis, *n* is the number of data points in the sample, x_i is the element number *i* of the sample and $\bar{x}$ is the sample mean (Ho and Yu, 2015).

4.3.4 Trends calculation

Once the distribution of wind speed values has been evaluated, the next step is to calculate the wind speed trends in South Greenland, past and future. These trends were calculated for each simulation listed in Table 4.3 using a simple linear regression, computed in Ferret software with the “regresst.jnl” module. This module gives back the slope and intercept of the regression line and the cumulated trend can then be calculated by multiplying the slope with the number of observations. The trends were evaluated for the monthly, yearly and seasonally spatially averaged time series, then for each grid cell at the levels of interest. For the M-E5-v3.11 simulation, the air density trend was assessed using the same method and the theoretical maximum wind power trend was calculated using the Betz law on the daily wind speed and air density data. This law is calculated as follows:

$$Pmax = 0.5 \times \rho \times S \times v^3 \quad (6)$$

where *Pmax* is the theoretical maximal wind power that a wind turbine can yield in W, ρ is the air density in $kg.m^{-3}$, *S* is the surface swept by the blade of the turbine in m^2 (which in this case will be fixed to 1) and *v* is the wind speed in ms^{-1}. The wind power trend was also assessed by linear regression. The significance of the cumulated trends was evaluated by comparing them to the STD of their associated time series.

Chapter 5: Results and discussion

5.1 Part 1: Influence of spatial resolution on wind speed and validation of MAR

5.1.1 Results over 2016-2018

In Annex A, detailed Tables A.1, A.2 and A.3 give the correlation, RMSE, RMSEc and bias between the stations' time series and the time series of their corresponding MAR grid cell for domains GR5, GR10, GR15 and GR20. The calculations have been made for winter (January, February, March) and summer (June, July, August) for 2016, 2017 and 2018. The bias has been calculated as the mean difference between the model and the observations. Mean correlations, bias, RMSE and RMSEc per year and spatial resolutions are listed here in Tables 5.1, 5.2, 5.3 and 5.4.Tables 5.5 gives the averaged RSME in % of the averaged STD (of the observation data) while Table 5.6 lists the mean observed wind speed per year and its associated STD. The detail of the latter per station in given in Table A.4 (Annex A).

***Table 5.1**: Mean correlation per year and spatial resolution*

	WINTER				**SUMMER**			
	GR5	GR10	GR15	GR20	GR5	GR10	GR15	GR20
2016	0.84	0.77	0.74	0.73	0.76	0.70	0.66	0.66
2017	0.85	0.79	0.75	0.74	0.80	0.75	0.72	0.70
2018	0.84	0.79	0.76	0.73	0.86	0.81	0.78	0.77

***Table 5.2:** Mean bias per year and spatial resolution (ms^{-1})*

	WINTER				**SUMMER**			
	GR5	GR10	GR15	GR20	GR5	GR10	GR15	GR20
2016	1.1	1.0	1.0	1.1	0.6	0.6	0.7	0.7
2017	0.8	0.6	0.8	0.8	0.7	0.5	0.6	0.5
2018	0.5	0.3	0.5	0.7	0.3	0.1	0.2	>0.01

***Table 5.3**: Mean RMSE per year and spatial resolution (ms^{-1})*

	WINTER				**SUMMER**			
	GR5	GR10	GR15	GR20	GR5	GR10	GR15	GR20
2016	3.4	3.8	4.0	4.0	2.2	2.4	2.7	2.7
2017	3.1	3.5	3.8	3.8	2.0	2.2	2.4	2.4
2018	2.8	3.1	3.5	3.6	1.9	2.1	2.4	2.3

***Table 5.4:** Mean Centred RMSE per year and spatial resolution (ms^{-1})*

	WINTER				**SUMMER**			
	GR5	GR10	GR15	GR20	GR5	GR10	GR15	GR20
2016	2.9	3.5	3.7	4.0	1.8	2.2	2.4	2.4
2017	2.6	3.1	3.4	3.4	1.8	2.0	2.2	2.2
2018	2.6	2.9	3.2	3.3	1.8	2.0	2.2	2.1

***Table 5.5:** Mean RMSE in % of STD of the observation data.*

	WINTER				**SUMMER**			
	GR5	GR10	GR15	GR20	GR5	GR10	GR15	GR20
2016	68	77	80	81	79	85	94	93
2017	64	72	78	78	75	79	85	85
2018	64	69	77	81	61	67	74	71

***Table 5.6**: Mean observed wind speed and STD per year and season*

	WINTER		**SUMMER**	
	Mean (ms^{-1})	STD (ms^{-1})	Mean (ms^{-1})	STD (ms^{-1})
2016	8.3	5.0	4.8	3.0
2017	7.7	4.9	4.8	3.0
2018	7.5	4.6	5.2	3.2

Correlation

The first observation stemming from analysis of Table 5.1 is that the correlation between the model and the stations generally improves as resolution increases. The highest mean correlation is found for summer 2018 at GR5 (R=0.86) while the lowest one is found for summer 2016 at GR15 and GR20 (R=0.66). In Table 5.1, the difference in correlation is significant (ΔR>=0.05) in each case between GR5 and the other resolutions. The discrepancies between GR15 and GR20 are always <0.05 and are only significant between GR10 and GR15 for summer 2016 (ΔR=0.06). The differences between GR10 and GR20 are in most cases significant. The mean correlations with GR15 and GR20 in summer 2016 are the only cases where R<0.70. In general, the ΔR can be ordered as follows: GR5-GR10>GR10-GR15>GR15-GR20.

Looking at the detailed Tables A.1, A.2 and A.3, the first thing to note is the unusually strong discrepancies between the correlations for station ANG (R ranging from 0.20 to 0.72 in 2016, from 0.57 to 0.85 in 2017 and from 0.60 to 0.85 in 2018). This is likely to affect the results from Table 5.1. The poor correlations in summer 2016 (Table A.1) for stations QAS_L and UKI (R<0.60) are also likely to explain why the mean correlations are lower that year in Table 5.1. The same conclusion can be drawn for summer 2017 where QAS_L correlations are <0.60 as well (Table A.2). Other than for the above-mentioned stations the correlation between MAR and the observations is in each case good (R>0.70) except for UKI-GR20 (R=0.66) in winter 2016, FRE-GR15 (R=0.65) and FRE-GR20 (R=0.64) in summer 2017, and QAS_L-GR20 (R=0.61), QAS_M-GR15 (R=0.69), QAS_M-GR20 (R=0.66) and UKI-GR20 (R=0.69) in winter 2018 (see Tables A.1, A.2 and A.3).

As to the best correlations between MAR and observations, they are found for stations NUN and IKS for 2016 and 2017, where R ranges from 0.87 to 0.92 (2016) and from 0.82 to 0.88 (2017) for IKS; and from 0.76 to 0.89 (2016) and from 0.85 to 0.92 (2017) for NUN (Tables A.1 and A.2). For 2018, the best correlations are found for NAR (R ranges from 0.81 to 0.89) and again for NUN where R ranges from 0.85 to 0.91 (Table A.3).

Still in Tables A.1, A.2 and A.3, it can be noted that the differences in correlation between GR5 and GR10 for individual stations are twice more frequently significant in winter than in summer. Stations ANG, FRE, IKM and UKI have a significant GR5-GR10 correlation difference for each winter and for two out of three summers. Station NUN has a significant

GR5-GR10 correlation difference in winter for 2016 and 2017. Finally, this difference is significant in winter 2016 for QAS_L and in winter 2018 for QAS_U. Some ΔR are significant between GR15 and GR20 but happen least frequently than between other resolutions and only in winter, with one exception (UKI). They happen for stations ANG, QAS_L and UKI. In contrast, the correlation discrepancy between GR5 and GR20 is in some case <0.05 and this happens almost exclusively in summer. It is the case for stations FRE, IKM, IKS and UKI for 2016 (Table A.1), for station IKS in 2017 (Table A.2) and for stations QAS_L, QAS_U and NUN in 2018 (Table A.3).

Mean bias

As listed in Table 5.2, the mean bias is at all times <1 ms^{-1} except for winter 2016, where it is <1.5 ms^{-1}. In comparison to Table 5.6, the mean bias always represents <15% of the mean observed wind speed over the corresponding period. These mean biases can thus be considered as small in general. Although on an individual station level, the bias can represent a larger part of the mean observed wind speed (59% at GR15 for NAR in winter 2018 and 52% at GR10 for IKS in summer 2017, for example). It can be noted in Table 5.2 that the mean bias is always positive, suggesting that MAR has a tendency to slightly overestimate the wind speed. However, when looking at Tables A.1, A.2 and A.3, the bias per station is not strictly positive. For station NUN, the bias is at all times negative. For stations such as QAS_L, UKI, ANG and IKM, the sign of the bias can vary between the seasons depending on the year. Furthermore, within the same season, the sign of the bias can vary between the different resolutions, as is the case e. g. for stations QAS_L and UKI in 2018 (Table A.3). Yet, the bias remains principally positive. The highest bias in absolute value is found for station IKS for 2016 and 2017 (respectively 3.2 and 3.5 ms^{-1}) and for station FRE for 2018 (2.5 ms^{-1}). Finally, it can be noted that the mean bias is not necessarily higher as the resolution gets coarser, unlike the correlation (see Table 5.1).

RMSE and RMSEc

First of all, it can be noted from Table 5.3 that the RMSE is larger in winter than in summer regardless of the resolution because the STD is larger in winter. As found in Table 5.5, the RMSE is always smaller than one STD, suggesting that it is insignificant. Nonetheless, the RMSE slightly increases as the resolution gets coarser. The highest RMSE is found for GR20 (4.0 ms^{-1}) for 2016 and the lowest is found for GR5 in 2018 (1.9 ms^{-1}). When looking at the stations individually, all have similar RMSE for the different resolutions, between 1 and 5 ms^{-1}

except for station ANG which shows odd values. For this station, in 2016, the RMSE ranges from >5ms^{-1} to 7.9 ms^{-1}, except in summer at resolution GR5 (Table A.1). For winter 2017, values of RMSE are between 5 and 7 ms^{-1} for GR10, GR15 and GR20 (Table A.2). Only GR15 has a RMSE greater than 5ms^{-1} with station ANG for winter 2018 (Table A.3). These high values of RMSE are consistent with the fact that ANG has poor correlation with MAR values. The station with the smallest values of RMSE is QAS_U, with RMSE ranging from 1.2 to 3.2 ms^{-1} for 2016 (Table A.1), from 1.3 to 2.6 ms^{-1} for 2017 (Table A.2) and from 1.5 to 2.8 ms^{-1} for 2018 (Table A.3).

Finally, Table 5.4 lists the mean RMSEc, which is the error between the model and the observations without the bias. By comparing this Table with Table 5.3, it can be noted that without the bias, the error between the model and the observation would be reduced by up to 15%. In Table 5.4, the mean RMSEc ranges from 1.8 to 4.0 ms^{-1}.

5.1.2. Results for 2020

Table 5.7 lists the correlation, RMSE, RMSEc and mean bias calculated between the observations from the three Katabata AWSs and their corresponding grid cell of the MAR for spatial domains GR5, GR10, GR15 and GR20:

***Table 5.7**: Correlation, RMSE (ms^{-1}), RMSEc (ms^{-1}) and mean bias (ms^{-1}) between the MAR and the Katabata observations for the period September-December 2020.*

		SEPTEMBER- DECEMBER 2020			
		GR5	GR10	GR15	GR20
KAT_0460	CORREL	0.89	0.86	0.87	0.84
	RMSE	2.6	3.0	3.1	3.2
	RMSEc	2.6	2.8	2.8	2.9
	BIAS	-0.04	1.1	1.3	1.2
KAT_6640	CORREL	0.89	0.84	0.82	0.74
	RMSE	2.9	3.3	3.3	3.9
	RMSEc	2.7	3.2	3.3	3.9
	BIAS	1.0	0.5	0.1	0.3
KAT_0680	CORREL	0.75	0.75	0.76	0.78
	RMSE	6.4	5.5	5.7	6.0
	RMSEc	4.9	3.9	3.5	3.3
	BIAS	4.1	3.8	4.5	4.9

***Table 5.8:** Mean wind speed and STD of the Katabata observations for the period September-December 2020.*

	MEAN (ms^{-1})	STD (ms^{-1})
KAT_0460	6.5	5.4
KAT_6640	8.6	5.6
KAT_0680	4.0	4.2

Correlation

The first observation that can be made from Table 5.7 is that the correlation with MAR is good for all spatial resolutions (R>0.70). As was the case with the mean correlation for the reference dataset (Table 5.1), the correlation decreases as the resolution gets coarser, except for station KAT_0680 where the ΔR is not significant (ΔR<0.05) between all resolutions. For KAT_0460, the ΔR is significant between GR5 and GR20 (ΔR=0.05). For KAT_6640, the ΔR is significant between GR5 and all the other resolutions. It is also significant between GR10 and GR20 (ΔR=0.10) and between GR15 and GR20 (ΔR=0.08). Station KAT_0680 has the lowest resolutions compared to the other KAT stations. Compared with the reference dataset (Table 5.1), the correlation between MAR and the KAT stations are in general slightly better.

Mean Bias

Furthermore, when comparing Tables 5.7 and 5.8, the mean bias represents maximum 20% of the mean wind speed for station KAT_0460 and maximum 12% of the mean wind speed for station KAT_6640. This suggests MAR slightly overestimates the wind there as it is the case for the reference dataset (see Section 5.1.1). However, for station KAT_0680, the mean bias represents between 95 and 120% of the mean wind speed. The wind speed there thus tends to be significantly overestimated by the model. As was the case for the reference dataset, the mean bias seems to be independent from the spatial resolution.

RMSE and RMSEc

Concerning the RMSE, stations KAT_0460 and KAT_6640 have insignificant RMSE for all resolutions. These RMSE represents 70% or less of their respective STD when comparing Table 5.7 with Table 5.8. However, the RMSE of KAT_0680 is greater than one STD for every spatial resolution. Without the bias, the error between MAR and the observations is reduced by less than 10% for stations KAT_6640 and KAT_0460 when comparing their RMSE with corresponding RMSEc. For KAT_0680, the error is reduced by 24, 28, 38 and 45% for GR5, GR10, GR15 and GR20 respectively when going from RMSE to RMSEc. The RMSEc of KAT_0680 is only greater than one STD for GR5.

5.1.3. Discussion

In this section, the results from Sections 5.1.1 and 5.1.2 will first be discussed in regard to the results from Delhasse et al (2020) who validated MAR wind speed outputs above the GrIS. Then, a discussion will be made on the impact of the spatial resolution on the wind speed in the Greenlandic tundra. Finally, the unusual results from individual stations will be discussed.

Validation of MAR

Based on the results from Section 5.1.1 and 5.2.1, it is safe to say that MAR is fairly in line with the observations, taking into account the highly complex topography of the tundra. In general, the mean correlations between modelled and observed wind speed were good ($R>0.70$, with a few exceptions), the mean bias was less than 15% of the averaged observed mean wind speed and the mean RMSE was never greater than one STD of the averaged observed wind speed for the reference dataset. For the Katabata dataset, only station KAT_0680 had significant bias and RMSE, although it had good wind speed correlation. The two other KAT

stations had similar values than the reference dataset. As already mentioned, their correlation with MAR was even slightly better, although we should keep in mind that observations were compared for a different season.

For the reference dataset, the correlations found in Table 5.1 at GR15 are similar to those found by Delhasse et al. (2020) at the same resolution (R=0.80 on annual average and R=0.74 on summer average over the period 2010-2016). For the mean bias, those found by Delhasse et al. (2020) are 1.3 ms^{-1} on annual average and 1.0 ms^{-1} on summer average. However, it should be noted that these values are the mean bias calculated between the 10 m modelled wind speed and the observed wind speed recorded at approximately 3 m a.g.l by PROMICE stations. Considering this elevation a.g.l difference, it is no surprise that MAR overestimates the wind speed in Delhasse et al. (2020) and that these bias values are greater than those found for the reference dataset at GR15 (see Table 5.2). However, these authors also compared the 2 m modelled wind speed, which is at a closer level a.g.l. to the PROMICE anemometers, with the observed wind speed. At that level, they found a slight underestimation of the wind speed by MAR (-0.2 and -0.3 ms^{-1} on annual and summer average respectively). But this negative bias seems logical if the values of MAR are extracted at a slightly lower level than that of the stations. Taking all these mean bias values found by Delhasse et al. (2020) into account, it is suggested that the overestimation of MAR over the tundra is greater than over the GrIS, if we consider that for the reference dataset, the modelled wind speed has been compared with observations measured at the same level above ground (Table 5.2). This would be a consequence of the topography smoothing by the model that more strongly impacts the tundra. Anyway, the mean bias of MAR over the tundra stays small as seen in Section 5.1.1.

Concerning the RMSE, the values found by Delhasse et al. (2020) range between 2.0 and 2.3 ms^{-1} on annual average and between 1.6 and 1.8 ms^{-1} on summer average over the period 2010-2016 when comparing the 2 m and 10 m wind speed respectively with the PROMICE observations over the GrIS. At GR15 for the reference dataset (Table 5.5), the RMSE ranges from 3.2 to 3.7 ms^{-1} for winter and from 2.2 to 2.4 ms^{-1} for summer between 2016 and 2018. The summer RMSE is significantly stronger over the tundra than over the GrIS but in any cases, these errors were insignificant in Delhasse et al. (2020) as for the reference dataset in regard to one STD. The same goes for the RMSEc.

Impact of spatial resolution on wind speed

The fact that results are in general better for GR5 than for GR20 in Sections 5.1.1 and 5.1.2 is most probably linked to the fact that the topography is more strongly smoothed by the model for GR20 than for finer resolutions (Du Vivier and Cassano, 2013). When analysing the correlation difference between the different spatial resolutions, the modelled results do not improve linearly with the increasing resolution. For example, the accuracy increase is not significant when going from GR20 to GR15, most probably because, at GR15, the complex topography of the tundra is not significantly better resolved than for GR20. However, when going from GR10 to GR5, the improvement in wind speed correlation between the model and the observations is significant ($\Delta R>0.05$). Moreover, this improvement seems to be even more significant in winter than during summer. This suggests that the resolution has a greater impact on the wind speed outputs of the model in winter when the wind speed is higher.

Problematic stations

At an individual station level, Delhasse et al. (2020) found that over the period 2010-2016, daily data from station QAS_L had a correlation with the modelled 2-m wind speed of 0.68 on summer average. Poor correlation ($R<0.60$) with the modelled 2-m wind speed was also found for hourly data from station QAS_L in the reference dataset over the period 2016-2017 in summer. However, because the correlation in summer 2018 with QAS_L is >0.78 for all resolutions, the reason behind the poor summer correlations calculated for the previous years is probably a malfunction within the station instrumentation rather than the inability of MAR to accurately model the wind speed at that location. As a matter of fact, QAS_L is located on the ablation zone of the ice sheet where the topography is more homogenous than for the adjacent tundra. An influence of the relief on the results is thus unlikely in this case. Besides, station QAS_U is located nearby QAS_L (16 km, measured based on locations from Figure 3.3), though at a different elevation, and does not show this kind of poor correlations. This fact also suggests that the height at which measurements were taken compared with the 2-m wind speed simulated by MAR do not play a major role in explaining these differences. It might also be that the UKI station experienced problems with its sensor during summer 2016 as that would also explain the poor wind speed correlations for that season.

As for station ANG, the strong discrepancies in wind speed correlation between the different resolutions are hard to explain and would need further investigation. In fact, station KAT_6040 is located on the same MAR grid cell for GR10 and GR20 and does not show these kinds of

poor correlations with MAR for 2020. Both stations are located on the same island along the coast near the southern tip of Greenland, approximately 2 km away from each other (distance measured on Google Earth Pro based on the locations from Tables 3.1 and 3.2). Therefore, measurements from these stations do not seem to be directly strongly influenced by any particular topographical feature. An unresolved orographic element in lower resolutions is thus an unlikely explanation for this correlation decrease as the resolution gets coarser.

As for station KAT_0680, it is located on highly complex terrain, at the foot of a glacier valley. This might explain the higher RMSEc and bias found there compared with other KAT stations. Indeed, the fact that KAT_0680 is situated in a topographical feature that might not entirely be resolved by MAR can explain the fact that the bias and RMSEc are abnormally high for this station.

5.2. Part 2: Long-term wind speed variability

5.2.1. Wind speed distribution

Table 5.9 gives the results from the Shapiro-Wilk test conducted on time series of three randomly selected pixels from simulations M-E5-v3.9, M-CE-hist and M-MRI-hist. The Shapiro-Wilk test was applied over yearly and seasonally averaged data. For monthly means, as the test is not recommended for samples with more than 50 observations (see Section 4.3.3), the normality of the distributions is described by their skewness and kurtosis by equations (4) and (5). The pixels for which the test was applied are the same for all calculations, including skewness and kurtosis. They were randomly selected over land and their location is shown in Figure 5.1.

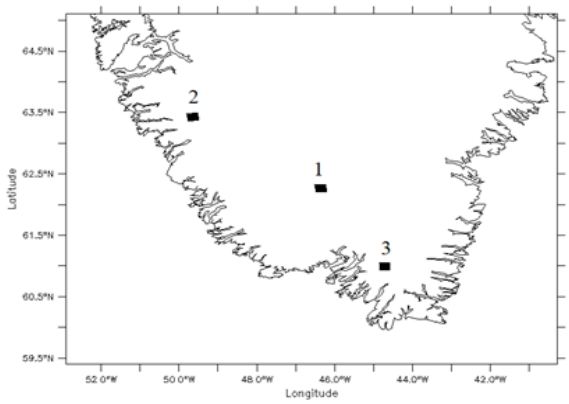

***Figure 5.1**: Location of the randomly selected onshore grid cells and their associated number.*

Table 5.9: *Results from the Shapiro-Wilk test on yearly and seasonally averaged observations from three randomly selected pixels.*

Simulation	Averaged period	Pixel number	W	p-value
M-CE-hist	Yearly	1	0.98	0.53
M-CE-hist	Yearly	2	0.98	0.78
M-CE-hist	Yearly	3	0.96	0.13
M-CE-hist	Summer	1	0.99	0.99
M-CE-hist	Summer	2	0.98	0.84
M-CE-hist	Summer	3	0.98	0.63
M-CE-hist	Winter	1	0.97	0.34
M-CE-hist	Winter	2	0.97	0.36
M-CE-hist	Winter	3	0.95	0.12
M-CE-hist	Yearly	1	0.97	0.41
M-CE-hist	Yearly	2	0.98	0.61
M-CE-hist	Yearly	3	0.98	0.72
M-MRI-hist	Summer	1	0.98	0.86
M-MRI-hist	Summer	2	0.94	0.03
M-MRI-hist	Summer	3	0.98	0.55
M-MRI-hist	Winter	1	0.98	0.62
M-MRI-hist	Winter	2	0.98	0.55
M-MRI-hist	Winter	3	0.95	0.15
M-E5-V3.9	Yearly	1	0.99	0.89
M-E5-V3.9	Yearly	2	0.90	>0.01
M-E5-V3.9	Yearly	3	0.95	0.06
M-E5-V3.9	Summer	1	0.99	0.99
M-E5-V3.9	Summer	2	0.98	0.84
M-E5-V3.9	Summer	3	0.98	0.63
M-E5-V3.9	Winter	1	0.96	0.18
M-E5-V3.9	Winter	2	0.96	0.21
M-E5-V3.9	Winter	3	0.96	0.25

It turns out from Table 5.9 that almost all time series are normally distributed with two exceptions. The null hypothesis ("data are normally distributed") is rejected with a 95 % confidence level (p-value <0.05) firstly for the summer time series of pixel number 2 from the M-MRI-hist simulation, secondly for the yearly time series of the same pixel from the M-E5-v3.9 simulation. This shows that the yearly and seasonally averaged distribution of wind speed is not strictly normal and can vary between models and pixels. However, because these non-normal distributions are not consistent for each model, the distributions can generally speaking be considered normal.

For monthly distributions, their histograms are shown in Figure 5.2. Table 5.10 gives their skewness (s) and kurtosis (k). It appears from Table 5.10 that all distributions have a positive skewness, implying that they are all asymmetrical with a tail oriented to the right. This can indeed be observed in Figure 5.2. The skewness is in each case lower than – or close to – 1. As a reminder, a normal distribution has a skewness of zero. The more the skewness is different from zero, the greater the asymmetry. The kurtosis is in most cases close to a normal kurtosis (k=3) with a few exceptions. The highest kurtosis is found for pixel number 2 for M-CE-hist (k=6.18). A kurtosis higher than 3 suggests that the shape of the distribution peaks higher than a Gaussian distribution. This is again clearly visible in Figure 5.2, especially for pixel number 2 which has the highest kurtosis for M-MRI-hist and M-CE-hist.

As suggested by Kim (2013), for large samples (n>300), it can be considered that distributions with a skewness lower than 2 (in absolute value) and a kurtosis lower than 7 do not substantially deviate from normality. In this case, the number of data points is 480 for monthly averaged wind speed distributions and the skewness and kurtosis satisfy in each case this condition.

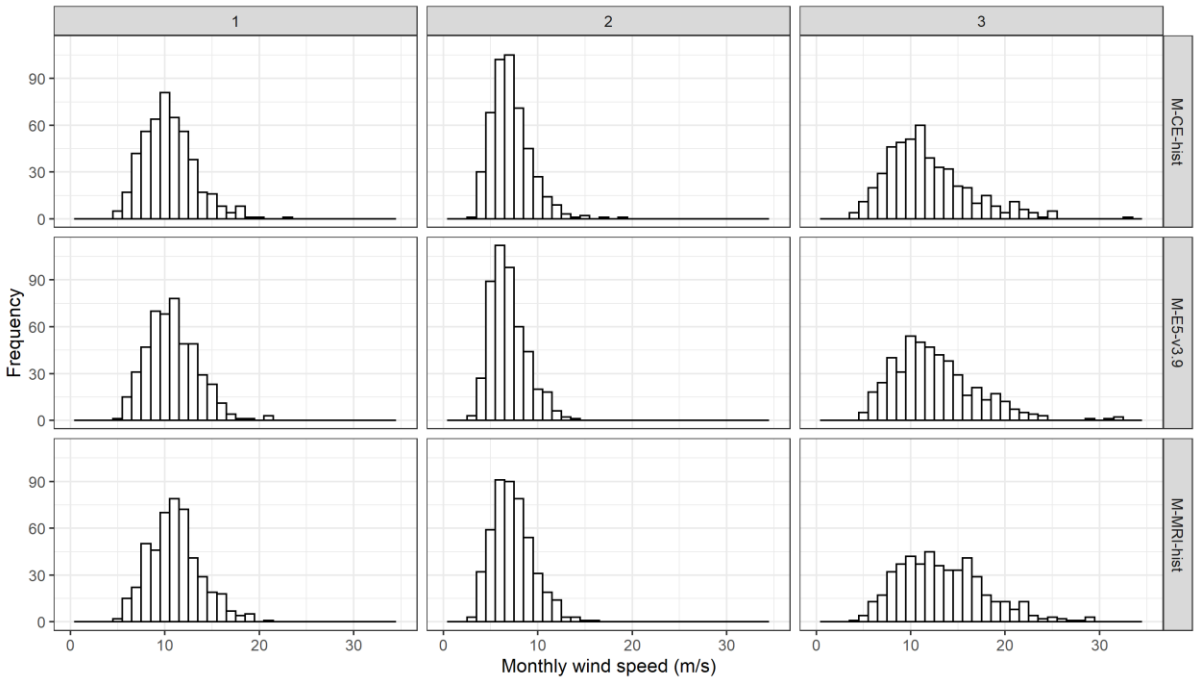

***Figure 5.2**: Frequency histograms of monthly averaged wind speed. Columns indicate the pixel number and rows indicate the simulation.*

***Table 5.9**: Skewness and kurtosis of monthly averaged wind speed data. Skewness=S, kurtosis=K.*

	Pixel #1	Pixel #2	Pixel #3
M-E5-v3.9	*s*=0.59 *k*=3.66	*s*=0.79 *k*=3.48	*s*=1.01 *k*=4.76
M-MRI-hist	*s*=0.48 *k*=3.28	*s*=0.75 *k*=3.74	*s*=0.64 *k*=3.31
M-CE-hist	*s*=0.74 *k*=3.99	*s*=1.23 *k*=6.18	*s*=1.00 *k*=4.31

Finally, it should be noted that the difference in the shape of the histograms in Figure 5.2 might be explained by the difference in wind regime between grid cells. Pixels 1 and 2 are more likely to have a dominantly katabatic wind regime whereas pixel number 3 is located closer to the southern tip of Greenland where a higher frequency of high-wind speed events such as tip jets occur (Figure 5.1). As mentioned in Section 2.2.1, katabatic winds are characterized by a steady wind speed and direction. This explains the shorter right tail of pixel 1 and 2 compared with pixel 3.

This part of the methodology consisted in a small investigation on the averaged wind speed distribution. Nonetheless, these results give an insight into how much the wind speed distribution deviates from normality. This is useful in the assessment of wind speed trend significance. As a matter of fact, a cumulated trend can be considered significant in climatology if its magnitude is greater than one STD, assuming the data distribution is normal (Xavier Fettweis, personal communication). Based on the results from this Section, this is how the significance of the general wind speed changes will be assessed further in this work.

5.2.2. Results over the period 1981-2020

5.2.2.1. General trends

Table 5.11 lists the wind speed cumulated trends calculated by linear regression over the spatially averaged data for each historical simulation (see Table 4.3) as well as the STD, both for monthly and yearly averaged data over the period 1981-2020. All cumulated trends from Table 5.11 are much smaller in absolute value than their associated STD. These general wind speed changes can thus all be considered insignificant over the 1981-2020 period. It should nonetheless be noted that cumulated trends depend on the number of observations on which they are calculated. Over a longer period of time, they might become significant assuming that their associated STD stays the same.

As can be seen in Figure 5.3, a wind speed trend is barely noticeable over the considered time period. Nonetheless, all simulations seem to be consistent with each other concerning the general wind speed change between 1981 and 2020, although the differences between them are a source of uncertainty. The mean cumulated trends of the ensemble of the five CMIP6 ESM-forced simulations are close to the cumulated trends calculated for M-E5-v3.9, the reference simulation.

***Table 5.11**: Wind speed cumulated trends and STD for monthly and yearly averaged observations over the 1981-2020 period at 100 m a.g.l, mean for the whole study area.*

	MONTHLY		**YEARLY**	
	Cumulated trend (m/s/40yr)	STD (ms^{-1})	Cumulated trend (m/s/40yr)	STD (ms^{-1})
M-CE-hist	-0.05	1.94	-0.01	0.27
M-CC-hist	-0.20	1.99	-0.18	0.29
M-CM-hist	-0.14	2.09	-0.11	0.29
M-MRI-hist	0.07	2.00	0.10	0.27
M-UK-hist	0.22	2.06	0.26	0.30
M-E5-v3.9	-0.03	2.01	-0.01	0.24
M-E5-v3.11	-0.12	2.02	-0.09	0.25
Ensemble mean *	-0.02	1.78	0.01	0.11

* Without M-E5-v3.9 and M-E5-v3.11.

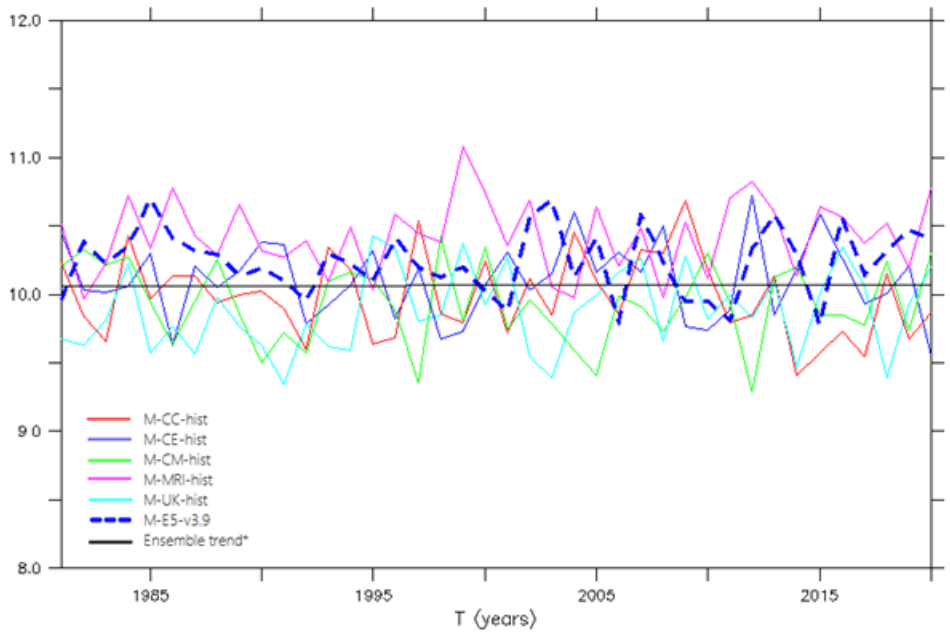

***Figure 5.3**: Yearly averaged wind speed and mean trend of the ensemble of five CMIP6 ESM-forced simulations over the 1981-2020 period at 100 m a.g.l.*

Figures 5.4 and 5.5 show the two-dimensional changes in wind speed between 1981 and 2020 for monthly and yearly averaged data respectively. The first observation that can be made regarding these figures is that in contrast to yearly means, no significant areas where the

absolute value of the cumulated trend over 40 years is greater than one STD, are present in Figure 5.4. Anyway, the wind speed change patterns are consistent for each simulation between Figure 5.4 and 5.5 but are not between simulations. Furthermore, concerning the general wind speed change on yearly means, the southernmost tip of Greenland seems to be the most frequent area with significant wind speed change, although the sign of the trend varies between simulations. Again, M-UK-hist shows the strongest change where all the western coast of the study area experiences an increase in wind speed of up to 1.7 ms^{-1} over 40 years.

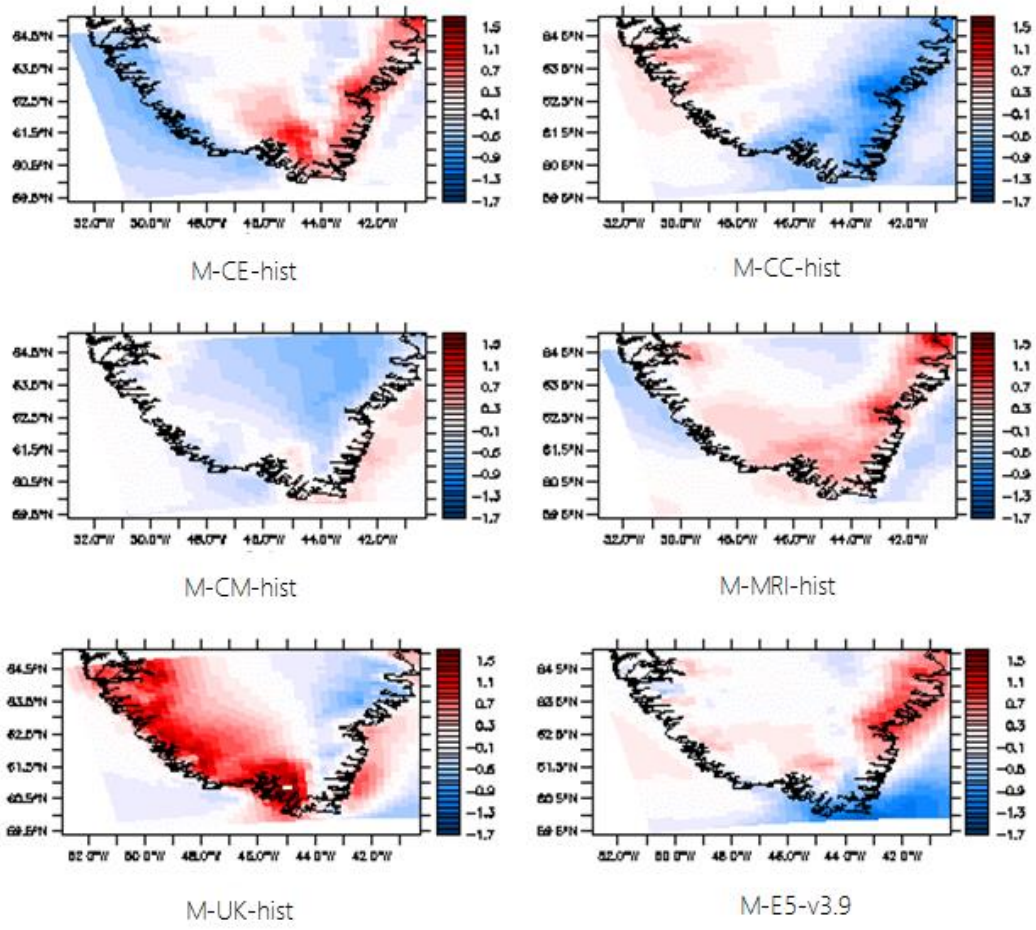

Figure 5.4*: Wind speed change calculated on monthly averaged data between 1981 and 2020 at 100 m a.g.l. No areas of significance were found. Data are expressed in m/s/40yr.*

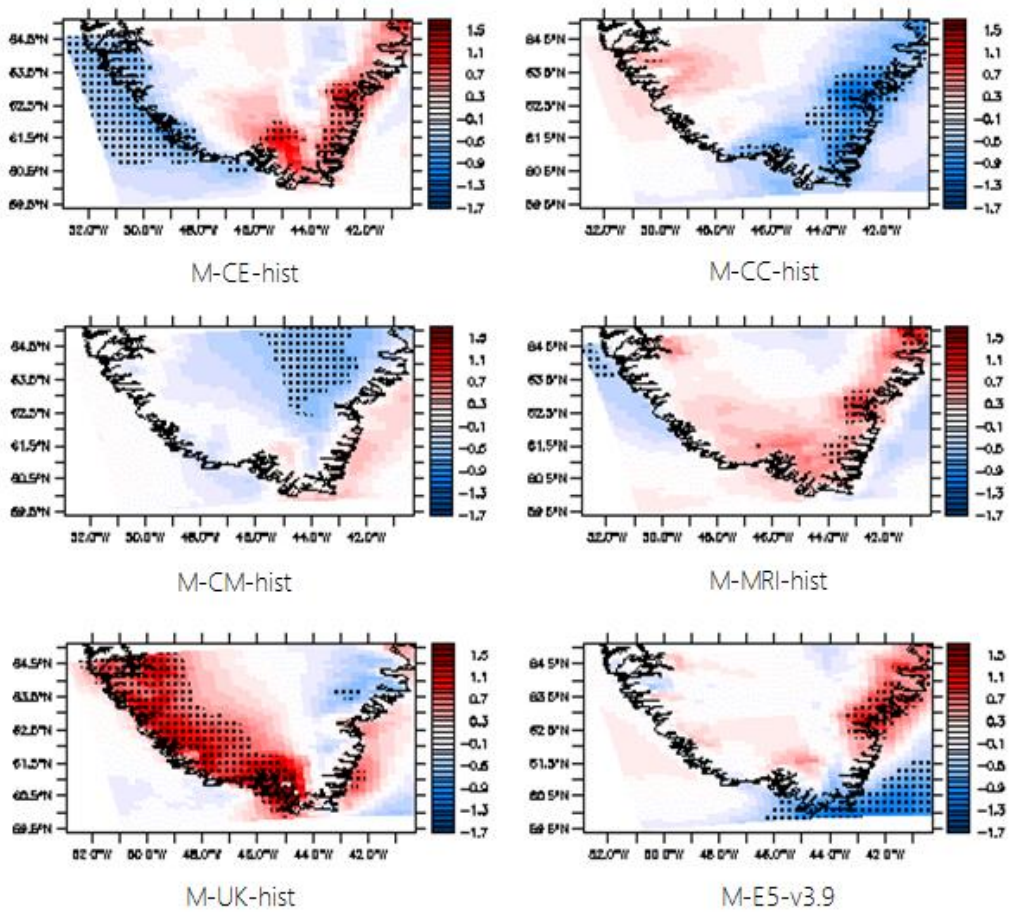

***Figure 5.5**: Same as Figure 5.4 but for yearly averaged data. Areas with a significant wind speed change are highlighted with a black dotted pattern.*

Regarding M-E5-v3.11, no significant cumulated trend in wind speed was found, as it can be seen again in Table 5.12 and in Figure 5.6. The air density however has a significant cumulated trend for the yearly means and this is clearly noticeable in Figure 5.6. As for the theoretical maximum wind power that can be yielded by a wind turbine, it has been calculated thanks to Betz's law where the area swept by the turbine's blades has been set to 1 m², as seen in Section 4.3.4. A negative cumulated trend in maximum wind power is noticeable in Figure 5.6, although Table 5.12 does not show any significance in regard to the STD.

As for two-dimensional trends, they are shown in Figure 5.7 for wind speed. Obviously, as both simulations have been forced with ERA-5, although at different spatial resolutions, cumulated trends from M-E5-v3.11 are very similar to those from M-E5-v3.9. The same area of significance can be found for both simulations in Figures 5.5 and 5.7. For monthly means, wind speed changes are once again not significant over the considered time period. Figure 5.8 shows the same cumulated trends as Figure 5.7 but for air density instead of wind speed. It can

be noted that air density has a negative cumulated trend over the whole study area, and a significant one only for the yearly averaged area. This can be explained by the fact that the air density is a function of air temperature. The warmer the air, the less dense it is. As said before (Section 1.2), temperature increases have been observed over the area by Hanna et al. (2021) of +1.7°C in summer and +4.4°C in winter for the 1991-2019 period.

Finally, Figure 5.9 shows the change in theoretical maximum wind power that can be yielded by a wind turbine between 1981 and 2020. Since the theoretical maximum wind power is a function of the third power of the wind speed, it is no surprise that its cumulated trends show the same patterns as the wind speed cumulated trends. Again, the changes in wind power calculated on the monthly means are not significant while a significant area with positive cumulated trends can be found along the eastern coast of the study area. This corresponds to the area of significant positive wind speed change over the same period for M-E5-v3.11. The area of significant negative wind speed change does not seem to significantly impact the maximum wind power at Cape Farewell. For the positive cumulated trends, they have an amplitude of around +500 W for monthly means while it is a little less for yearly means. It can be seen in Figure 5.6 that the wind speed and maximum wind power do not seem to have a significant change on the spatially averaged data between 1981 and 2020 in contrast to the air density.

Between 1981 and 2020, the mean maximum wind power calculated with Betz law (6) was 1570.00 W. The yearly cumulated trend of -55.15 W/40yr represents thus a general decrease in wind power production of approximately 3.5%. This reduction is of approximately 4.3% considering the monthly cumulated trend of -67.60 W/40yr. In Annex B, Figures B.1 and B.2 show the mean maximum wind power calculated between 1981 and 2020 per pixel and the percentage of power loss (or gain) the two-dimensional changes represent, respectively. It is clearly visible on Figure B.1 that Cape Farewell is the area with the highest wind power potential, corresponding the area of wind speed maxima identified by Radu et al. (2019). In the wind power increase area noticeable in Figure 5.9, the change in maximum wind power production between 1981 and 2020 represents up to 30% of the mean values locally. Near Cape Farewell, there has been a loss of up to 20% of the maximum wind power over the considered time period. The magnitude of these changes seems exceptionally high but we should keep in mind that according to Betz law (6): if we take the mean air density between 1981 and 2020 (=1.170 $kg.m^{-3}$) and assume it stays constant, a change in the mean wind speed of 0.1 ms^{-1}

would lead to a change of 20 W of maximum wind power. That is if we go from a wind speed value of 10.54 ms^{-1} (mean over 1981-2020) to 10.44 ms^{-1}).

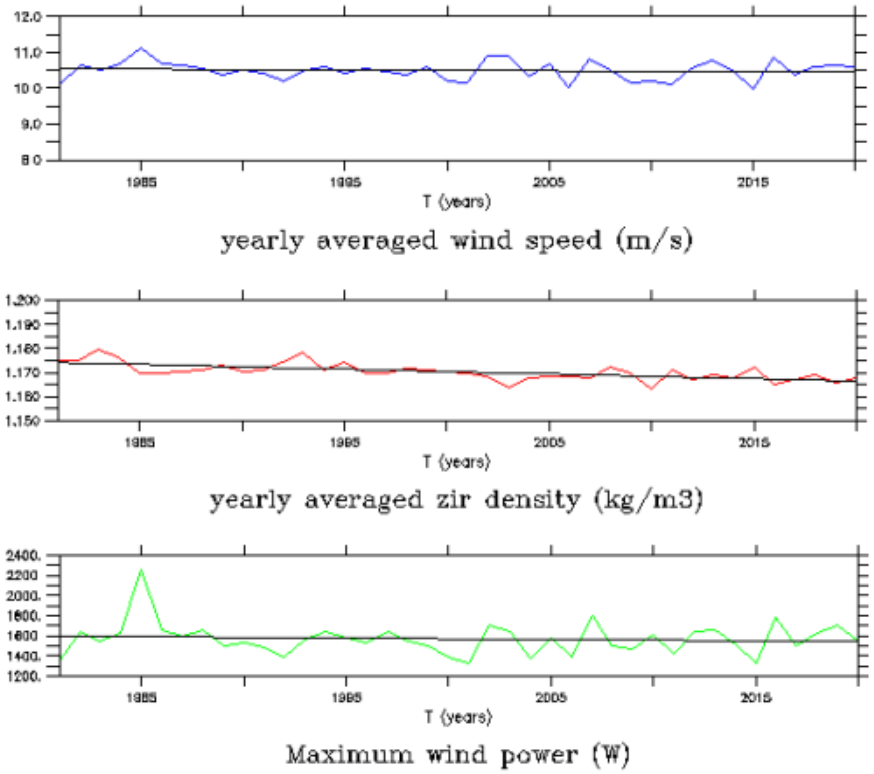

***Figure 5.6**: Yearly averaged wind speed, air density and maximum wind power over the 1981-2020 period at 100 m a.g.l. Colored lines indicate variables, black line indicates regression line.*

***Table 5.12**: Cumulated trends for monthly and yearly averaged wind speed, air density and theoretical maximum wind power for M-E5-v3.11 over the period 1981-2020.*

	MONTHLY		**YEARLY**	
Parameter	Cumulated trend (/40yr)	STD	Cumulated trend (/40yr)	STD
Wind Speed (m/s)	-0.12	2.02	-0.09	0.26
Air density (kg/m^3)	-0.01	0.02	-0.01	>0.01
Wind power (W)	-67.60	849.8	-55.15	126.70

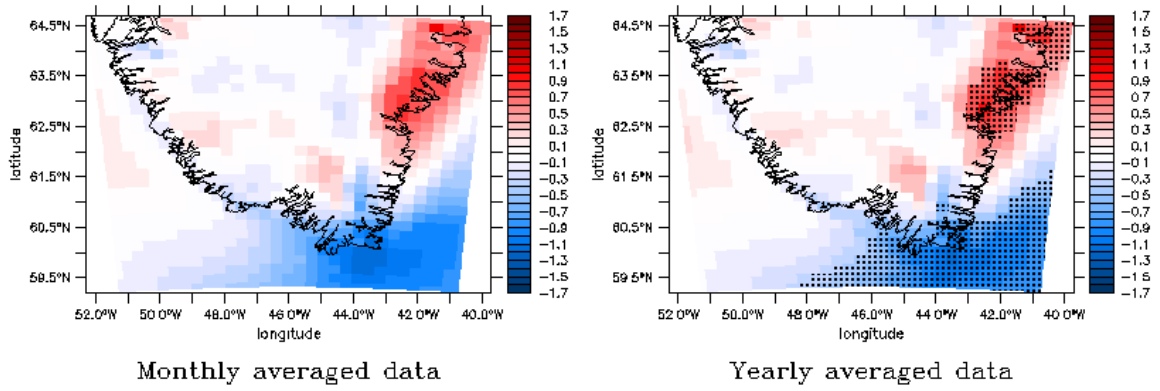

***Figure 5.7**: Wind speed change on monthly and yearly averaged data simulated by M-E5-v3.11 between 1981 and 2020 at 100 m a.g.l. The black dotted areas indicate locations of significant change. Data are expressed in m/s/40yr.*

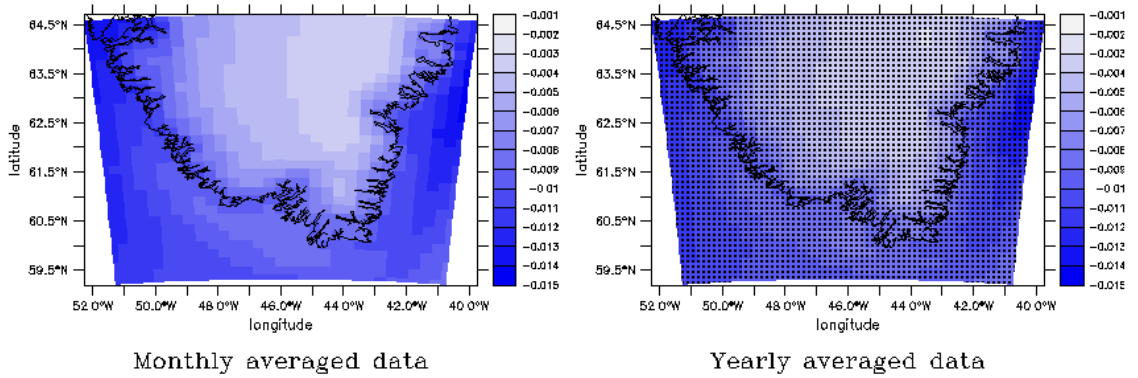

***Figure 5.8**: Same as Figure 5.7 but for air density. Data are expressed in kg/m³/40yr.*

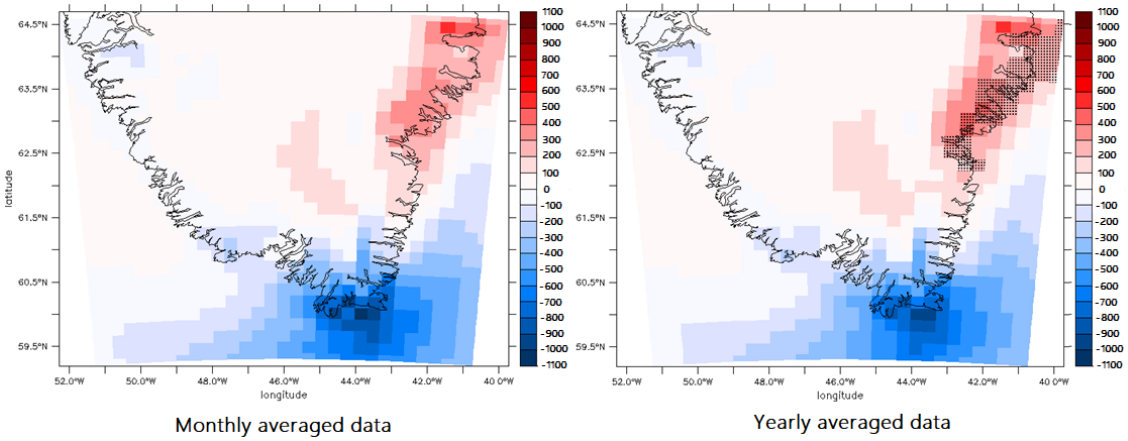

***Figure 5.9**: Same as Figure 5.7 but for maximum wind power. Data are expressed in W/40yr.*

In a nutshell, the analysis of the general wind speed changes over the 1981-2020 period show that these changes are insignificant for spatially averaged data. On a two-dimensional basis, only cumulated trends calculated for yearly means show areas of significance. This will be further discussed in Section 5.2.4. However, wind speed change patterns between simulations are highly contrasted and so is the significance of the changes. The same area can have a significant positive wind speed cumulated trend in some simulations while it can have a significant negative one in others.

For M-E5-v3.11, the two-dimensional wind speed change patterns are the same as for simulation M-E5-v3.9. Concerning the wind power, one area of significance has been found for yearly averaged data on the eastern coast of the study area corresponding to an area of significant wind speed change. These results should however be carefully interpreted considering that the wind speed change patterns are highly contrasted between all the different simulations for the considered time period. In the end, no clear wind speed general change has been identified in South Greenland between 1981 and 2020 for monthly and yearly mean.

5.2.2.2. Seasonal trends

Table 5.13 lists the same information as Table 5.11 but this time for summer and winter time series. As a reminder, the winter times series consists of the succession of all the winters of the considered time period. All the other seasons were excluded. The same principle goes for summer time series. The data were averaged over the months of January, February and March of each year for the winter and June, July and August for the summers. The same findings emerge as for Table 5.11. All these cumulated trends are again smaller in absolute value than their associated STD. It can thus again be considered that on a spatially averaged level, the wind speed general changes given by the different simulations are insignificant over the period 1981-2020.

Table 5.13: *Wind speed cumulated trends and STD for seasonally averaged observations over the period 1981-2020 at 100 m a.g.l., mean for the whole study area.*

	WINTER		**SUMMER**	
	Cumulated trends (m/s/40yr)	STD (ms^{-1})	Cumulated Trends (m/s/40yr)	STD (ms^{-1})
M-CE-hist	-0.02	0.70	-0.14	0.47
M-CC-hist	-0.53	0.67	0.22	0.40
M-CM-hist	-0.39	0.57	-0.07	0.42
M-MRI-hist	0.55	0.89	0.12	0.38
M-UK-hist	0.07	0.74	0.38	0.45
M-E5-v3.9	0.27	0.74	-0.14	0.47
M-E5-v3.11	0.06	0.76	0.33	0.47
Ensemble Mean*	-0.06	0.71	0.10	0.42

*without M-E5-V3.9 and M-E5-v3.11

Regarding two-dimensional wind speed changes, patterns are once again contrasting between simulations. Looking at Figure 5.10, simulations M-CC-hist and M-CM-hist have completely opposite wind speed change patterns. M-UK-hist modelled positive wind speed changes on almost the entire study area with again significant cumulated trends on the western coast. M-MRI-hist and M-CC-hist have similar patterns but they do not have the same areas of significance. It is however interesting to note that the areas of significant summer wind speed change between 1981 and 2020 are for the vast majority positive and located over the tundra or at the edges of the GrIS, although their location varies between the different simulations.

Concerning winter wind speed change patterns (Figure 5.11), these changes have a higher amplitude than for summers, although the patterns are also contrasting. M-MRI-hist and M-E5-v3.9 show an increase in wind speed almost over the whole study area while M-CC-hist and M-CM-hist show a general decrease. M-UK-hist shows again a relatively strong wind speed increase over the western coast of up to >+2.40 m/s/40yr. It is interesting to note that for three simulations, CRNMC-hist, M-MRI-hist and M-E5-v3.9, the eastern coast of the study area has significant winter wind speed changes. However, the sign of the cumulated trend is

positive for M-E5-v3.9 and M-MRI-hist while it is negative for M-CC-hist. The same goes for the western coast where M-UK-hist modelled a significant wind speed increase while M-CE-hist modelled a significant decrease over the considered time period.

The same observations as for Section 5.2.1.1 can be made here. No clear wind speed trends were identified on the spatially averaged data. The two-dimensional trend patterns were also contrasting between simulations. However, it is likely that the GrIS margins and adjacent tundra, especially the southern tip of Greenland, have experienced a wind speed increase over the 1981-2020 period when only considering summers. As a matter of fact, the majority of simulations show a positive wind speed change at Cape Farewell although it is not always significant (Figure 5.10). In contrast, winter trend patterns were inconsistent between the different simulations.

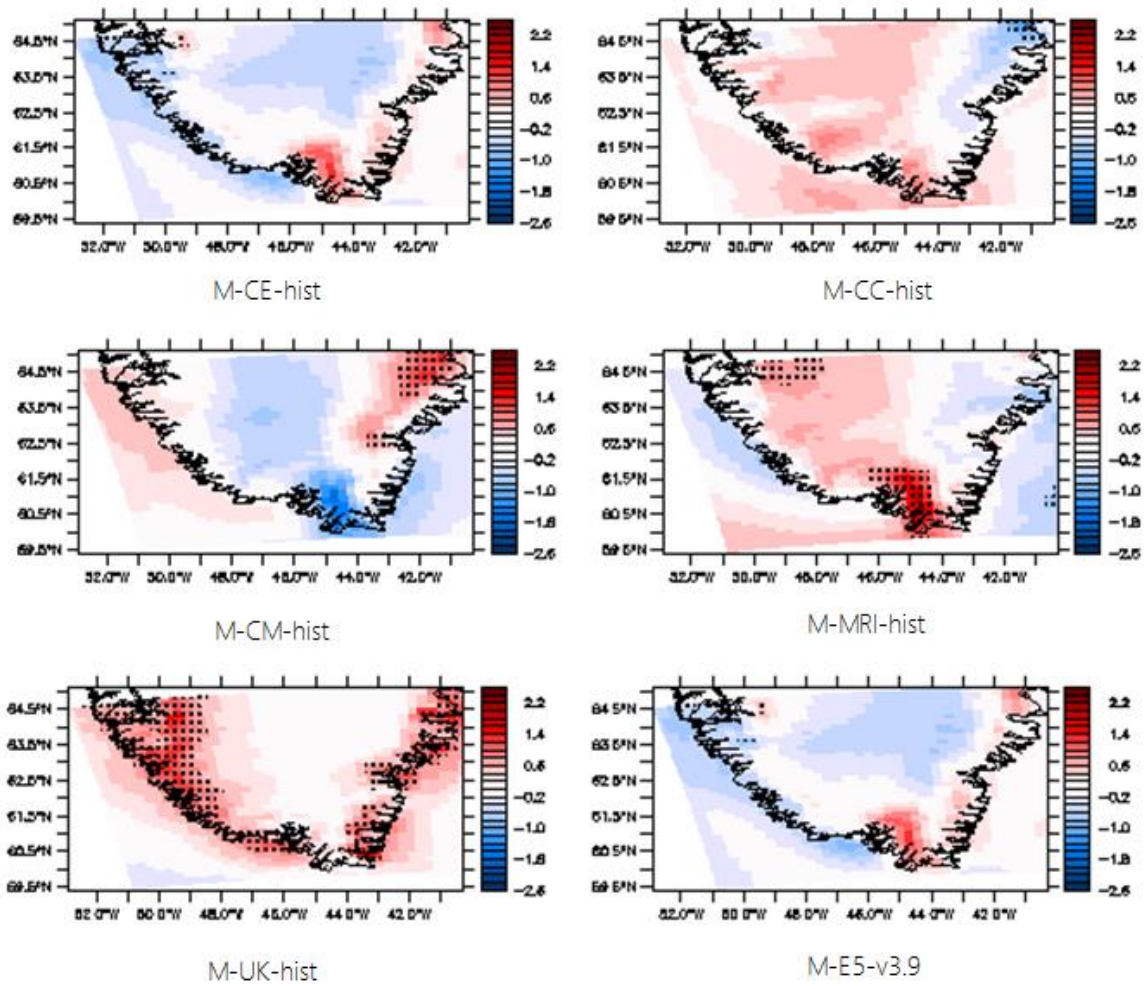

***Figure 5.10**: Summer wind speed change between 1981 and 2020 at 100 m a.g.l. Area of significant change are highlighted by a black dotted pattern. Data are expressed in m/s/40yr.*

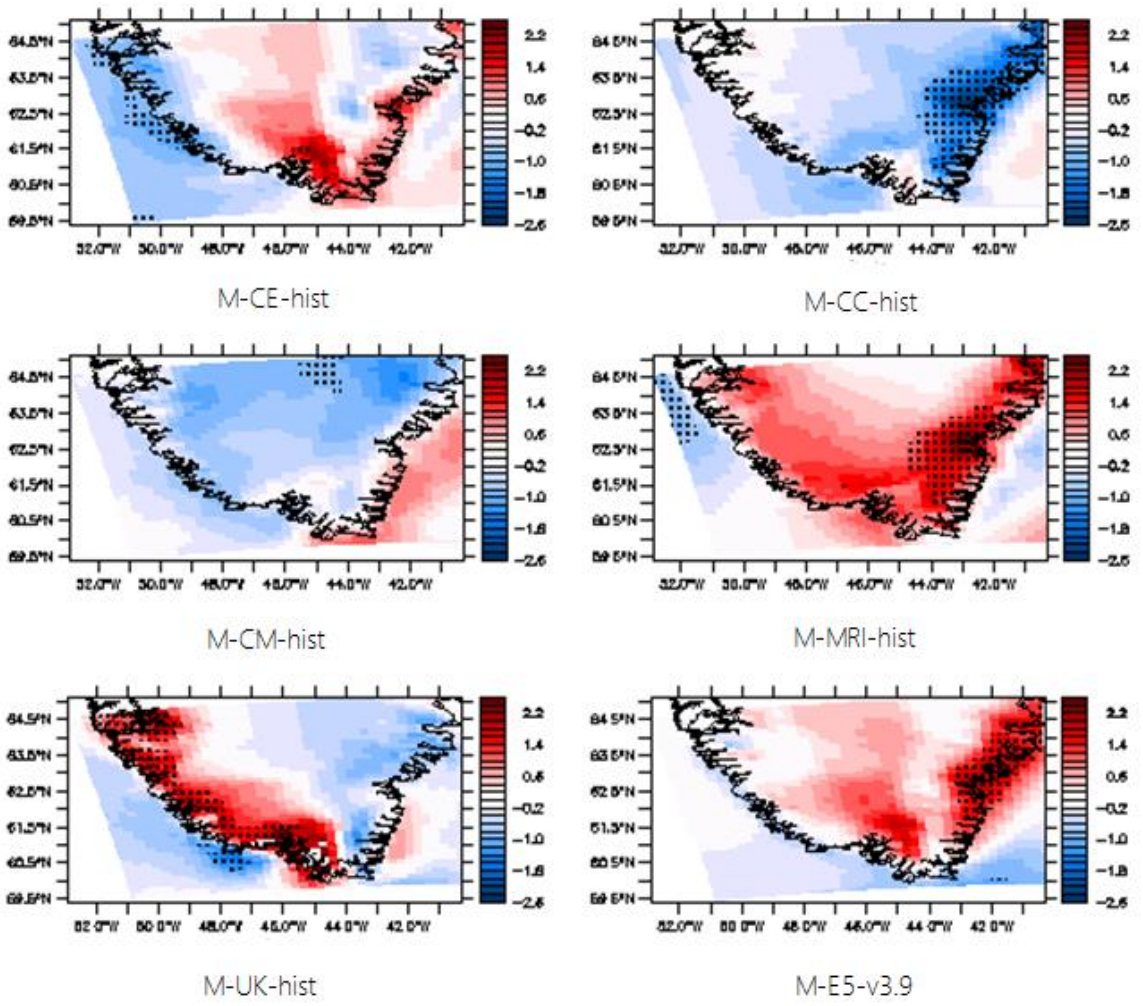

***Figure 5.11**: Same as Figure 5.10 but for winter.*

5.2.3 Results for 2021-2100

5.2.3.1 General trends

Table 5.14 lists the wind speed cumulated trends over the 2021-2100 period for monthly and yearly averaged data as well as their associated STD. Unlike for Section 5.2.1.1, all the simulations seem to agree on the sign of the cumulated trend, it is negative in each case. Three trends are significant as their magnitude is greater than one STD. All three are found for yearly means for simulations M-CE-ssp585, M-MRI-ssp585 and M-UK-ssp585. The greatest trend is found for M-MRI-ssp585 : -0.66 m/s/80yr and -0.65 m/s/80yr respectively for monthly and yearly means. The cumulated trends of the ensemble of the five CMIP6 ESM-forced simulations are -0.44 m/s/80yr (monthly) and -0.43 m/s/80yr (yearly) over 2021-2100 and are significant for the yearly averaged data. The latter is clearly noticeable in Figure 5.12 where

the same observation can be made as for Figure 5.3. The simulation M-MRI-ssp585 seems again to systematically model slightly higher wind speeds compared with the other simulations. Generally speaking, all simulations seem to be in a relatively good agreement with each other.

Table 5.14: *Wind speed trends and STD for monthly and yearly averaged observations over the period 2021-2100 at 100 m a.g.l., mean for the whole study area.*

	MONTHLY		**YEARLY**	
	Cumulated trend (m/s/80yr)	STD (ms^{-1})	Cumulated trend (m/s/80yr)	STD (ms^{-1})
M-CE-ssp585	-0.65	1.64	-0.64	0.36
M-CC-ssp585	-0.22	1.92	-0.21	0.36
M-CM-ssp585	-0.34	2.06	-0.33	0.33
M-MRI-ssp585	-0.66	1.92	-0.65	0.40
M-UK-ssp585	-0.34	1.79	-0.32	0.32
Ensemble mean	-0.44	1.62	-0.43	0.35

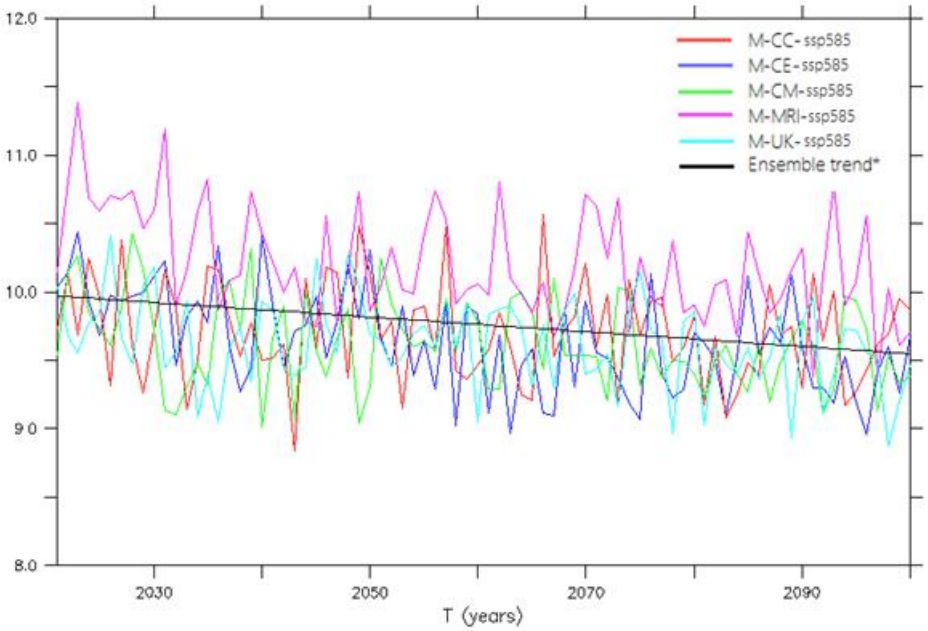

Figure 5.12 *: Yearly averaged wind speed and mean trend of the ensemble of the five CMIP6 ESM-forced simulations of the 2021-2100 period at 100 m a.g.l.*

A decrease of -0.43 m/s/80yr would cause a decrease of 80.46 W/80yr if we assume that the air density stays constant over 80 years (taking its mean value of 1.170 $kg.m^{-3}$ between 1981 and 2020). We also assume in this calculation that the wind speed goes from 10.54 ms^{-1} to 10.11 ms^{-1} in the Betz equation (6). This decrease represents approximately 5.1% of the mean maximum power of 1570.00 W calculated between 1981 and 2020. However, as seen in Section 5.2.2.1, there might be areas of increased wind power and the negative trend of air density is likely to continue in the future.

Regarding the two-dimensional wind speed changes, Figure 5.13 shows them calculated with the monthly averaged data over the 2021-2100 period at 100 m a.g.l. An interesting thing to note is that compared with Section 5.2.1.1, the wind speed change patterns seem to be in agreement between the different simulations. This is probably due to the fact, among others (see Section 5.2.4), that the cumulated trends here have been calculated for a longer period of time with thus more data points than for the 1981-2020 cumulated trends. Looking at Figures 5.13 and 5.14, while a large part of the study area experiences a wind speed decrease, two areas of positive wind speed change are consistently present over the study when comparing the different simulations, except for M-MRI-ssp585. These are located on the northern-east coast and in the northern-west of the study area. These areas are in each case significant in Figure 5.14. As was already the case in Section 5.2.1.1, the two-dimensional cumulated trends calculated for monthly averaged data are never greater in absolute value than one STD. Finally, it seems that the southern tip of Greenland is likely to experience a significant decrease in wind speed in the future (see Figure 5.14). It should be noted that the positive cumulated trends on the northern east coast and the negative cumulated trend on the southern tip of the study area are wind speed trend patterns that are similar to those calculated for M-E5-v3.11 and M-E5-v3.9 for the period 1981-2020 (see Figures 5.4, 5.5 and 5.7).

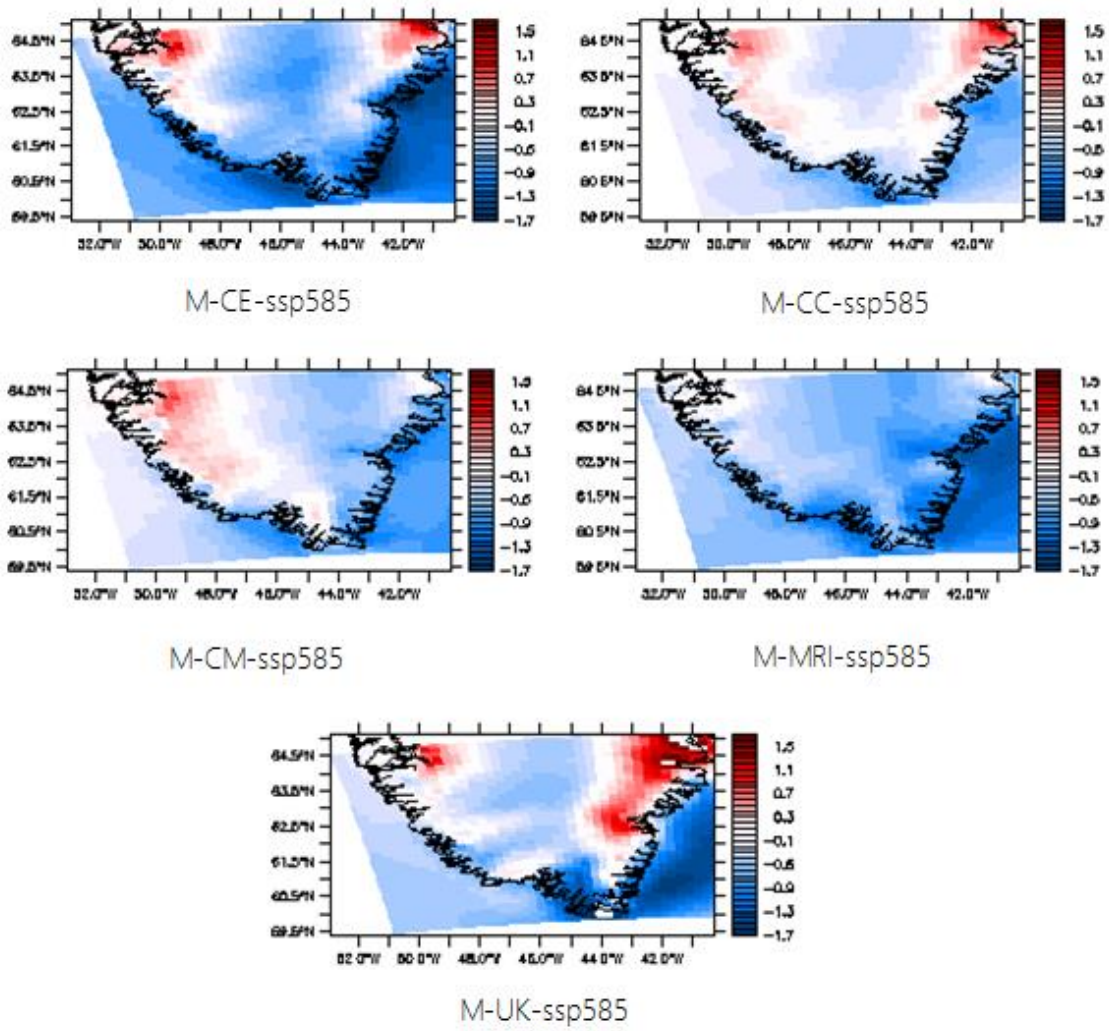

Figure 5.13 *: Wind speed changes calculated with monthly averaged data between 2021 and 2100 at 100 m a.g.l. No area of significance was found. Data are expressed in m/s/80yr.*

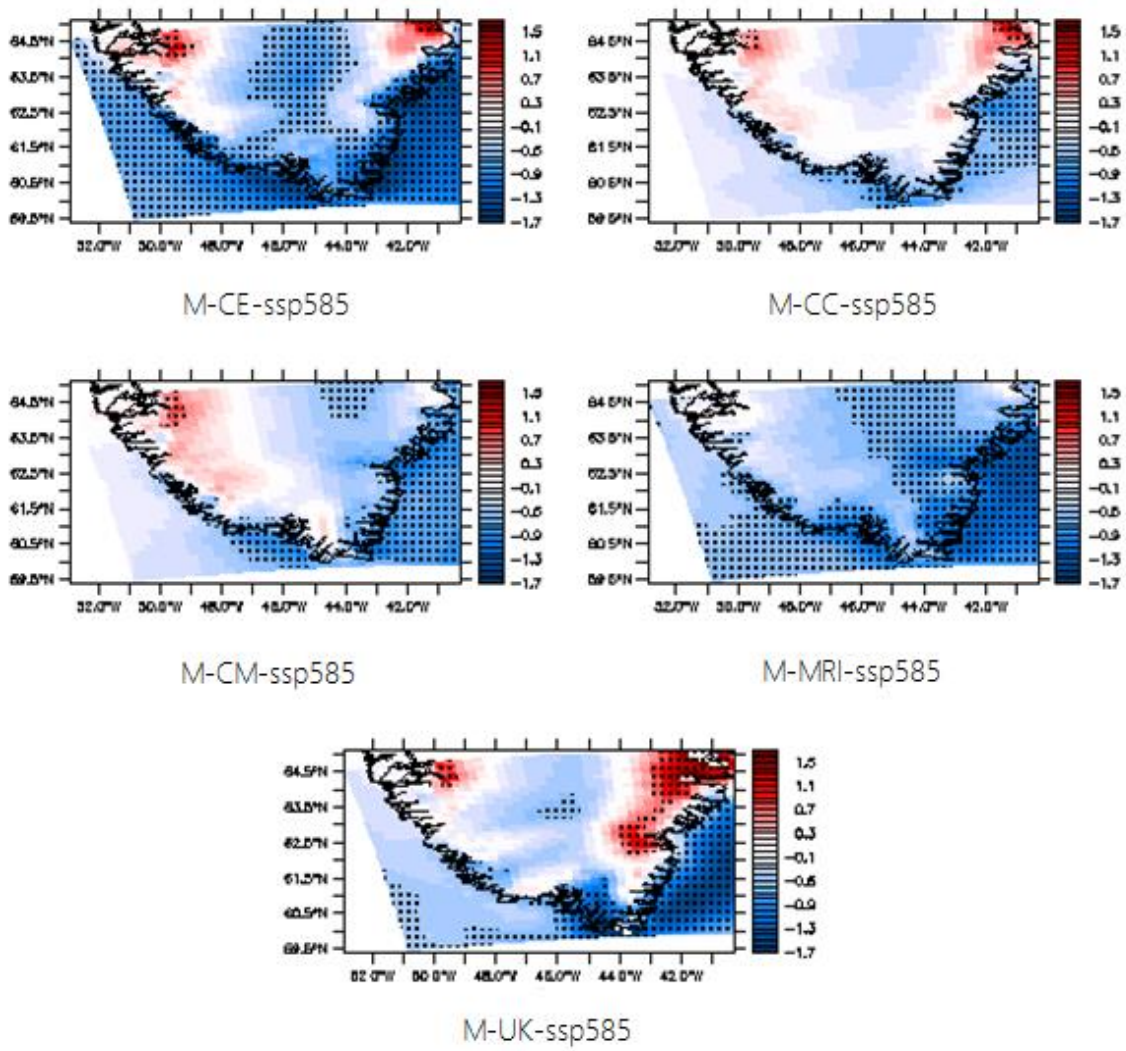

***Figure 5.14**: Same as Figure 5.13 but for yearly averaged data. Areas of significant wind speed changes are highlighted by the black dotted pattern.*

5.2.3.2 Seasonal trends

Table 5.15 lists the seasonal wind speed cumulated trends, calculated in the same way as in Section 5.2.2.2, for the period 2021-2100 at 100 m a.g.l., for the spatially averaged data. For winter, the cumulated trend with the greatest amplitude is found for M-CE-ssp585 (-1.03 m/s/80yr), followed by M-MRI-ssp585 (-0.96 m/s/80yr). Both of these trends are significant in regard to their respective STD. For summer, the trends have a smaller magnitude than winter trends and none of them is significant.

***Table 5.15**: Wind speed cumulated trends and STD for seasonally and spatially averaged observations over the period 2021-2100 at 100 m a.g.l, mean for the whole study area.*

	WINTER		**SUMMER**	
	Cumulated trend (m/s/80yr)	STD (ms^{-1})	Cumulated trend (m/s/80yr)	STD (ms^{-1})
M-CE-ssp585	-1.03	0.70	-0.07	0.47
M-CC-ssp585	-0.23	0.72	-0.24	0.48
M-CM-ssp585	-0.32	0.74	-0.18	0.43
M-MRI-ssp585	-0.96	0.81	0.04	0.48
M-UK-ssp585	-0.47	0.70	0.26	0.45
Ensemble Mean	-0.60	0.73	-0.04	0.46

As suggested from Table 5.15, no clear summer wind speed change pattern is present in Figure 5.15 except for the ocean along the eastern coast of the study area which has in three cases a negative cumulated trend, significant for M-CC-ssp585, M-MRI-ssp585 and M-UK-ssp585. The areas of wind speed increase visible in Figures 5.13 and 5.14 can be found again for M-UK-ssp585 and M-MRI-ssp585, although to a different extent. These are significant for both simulations. Anyway, except for M-UK-ssp585 the major part of the study area or even the entire area (for M-CE-ssp585 and M-CM-ssp585) has insignificant wind speed change over the considered 80 years.

As for winter (Figure 5.16), only two simulations show areas with positive significant wind speed change. These are M-UK-ssp585 and M-CM-ssp585. M-MRI-ssp585 do not show any positive change over the study area which is consistent with the fact that its spatially averaged negative cumulated trend is one of the strongest and most significant for winter. Finally, it can be seen that most of the significantly onshore decreasing wind speed areas are located over the tundra but to a small extent.

This analysis of seasonal trends shows that summer wind speed changes possibly play a role in the observed wind speed increase patterns calculated for monthly and yearly means along the GrIS edges (see Section 5.2.2.1). As for winter, the greater decrease in wind speed during this season is likely to affect the general wind speed change between 2021 and 2100. On a two-dimensional basis, it seems that some parts of the tundra in South Greenland may experience a

significant general wind speed increase during summer while others might experience a significant general wind speed decrease during the winter.

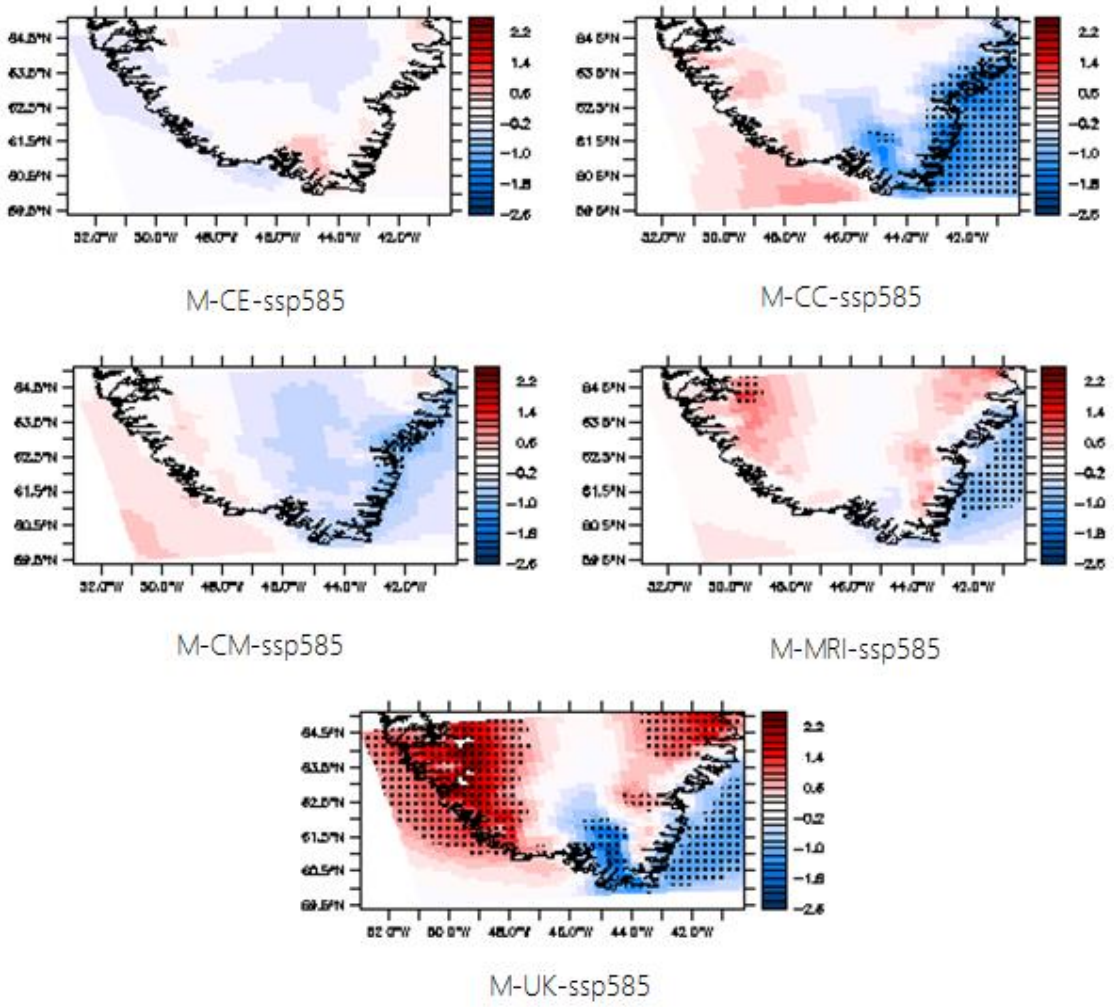

***Figure 5.15**: Wind speed trends calculated for summer time series.*

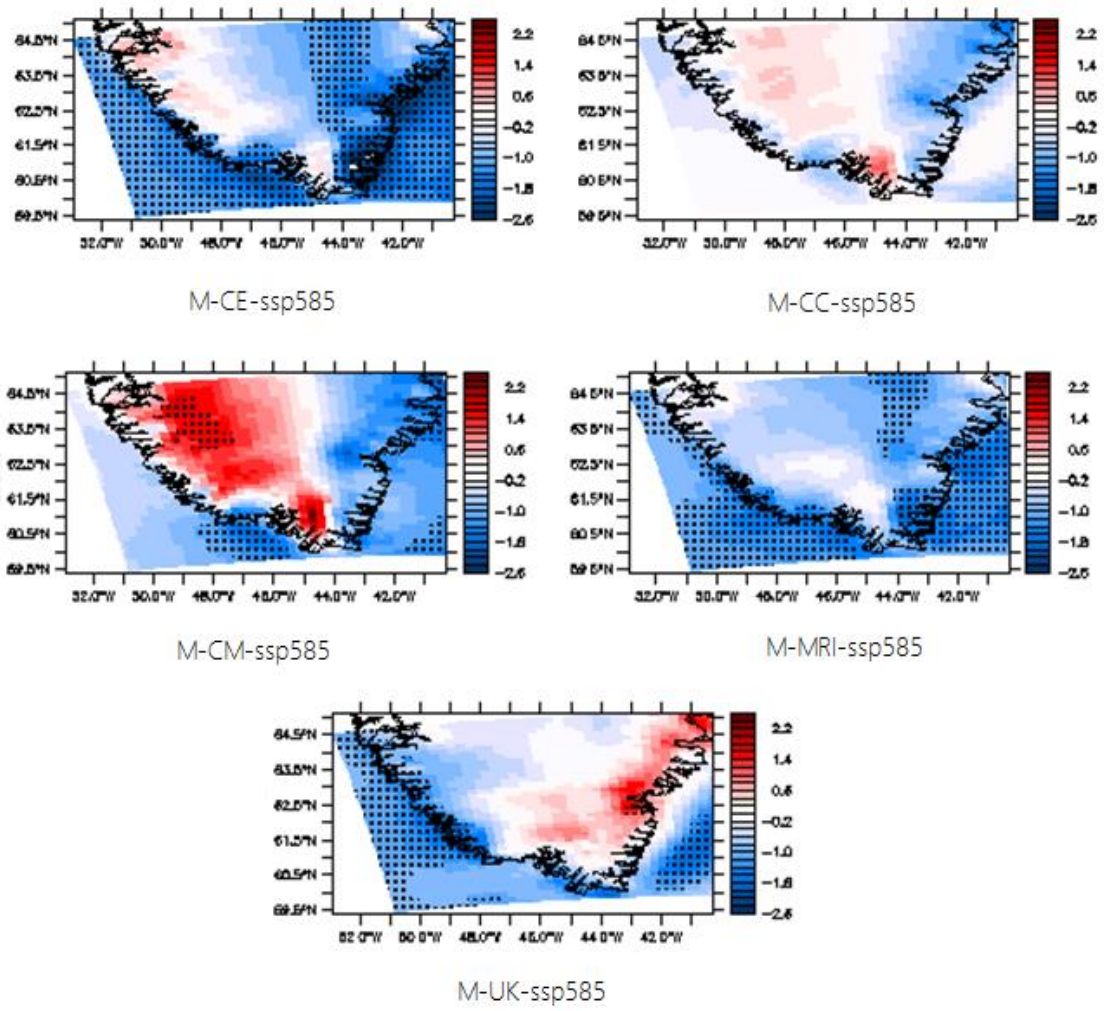

***Figure 5.16**: Wind speed trends calculated for winter time series.*

5.2.4 Discussion.

In this Section, results from Sections 5.2.2 and 5.2.3 will be discussed and compared. The first element to discuss is the fact that cumulated trends calculated over monthly means are never significant compared with yearly means. This is due to the fact that there is a seasonal variability in wind speed from one month to another that is not present in the yearly averaged data. This seasonal variability is greater than the interannual variability of wind speed and this is why cumulated trends from monthly means are never significant in regard to their STD. It should also be noted that the maximum wind power was calculated on daily means of wind speed and air density. However, the calculation would have been more accurate with hourly means because of the non-linearity of the Betz equation.

Secondly, the fact that no significant wind speed change was found at 100 m a.g.l. between 1981 and 2020 is in good concordance with the results of Laurila et al. (2021) who used ERA-5

to investigate 10 m-wind speed trends over Europe and the Northern Atlantic, including Greenland. They found no significant wind speed change either over the period 1979-2018. However, it appeared form this study that summer barrier winds might have strengthened between 1981 and 2020 as was suggested from Figure 5.9 although this is not very clear. This would be due to an enhanced temperature gradient between the tundra and the GrIS consistent with the rising temperature observed by Hanna et al (2021) over Greenland. Still, differences in modelled wind speed between the different CMIP6-forced MAR simulations constitute a source of uncertainty in the results. Furthermore, based on simulations from M-E5-v3.11, it appeared that if the barrier winds have effectively strengthen between 1981 and 2021, this has led to a non negligible increase in wind power production along the eastern coast of South Greenland. Results from ERA-5-forced simulations are likely to have more accurate results as observation data are assimilated into reanalyses (see Section 3.3), unlike ESMs.

Thirdly, the most important element to discuss is the general decrease in wind speed of -0.43 m/s/80yr projected between 2021 and 2100 as seen in Section 5.2.3. As explained in Section 2.3, this decrease can partly be due to the future weakening of the meridional temperature gradient between the mid-latitudes and the poles driving the large-scale circulation in the Northern Hemisphere (Jung and Schindler, 2019). As a reminder, this weakening in gradient strength is caused by the Arctic Amplification associated to global warming (Serreze and Francis, 2006).

Gorter et al. (2013) also found a general decrease in wind speed over the entire ice sheet between 1981-1998 and 2081-2098 (up to -0.3 m/s). As a reminder from Section 2.4, they modelled projected changes in wind speed over Greenland using a RCM forced by the CMIP5 large-scale model HadGEM2 based on a medium-range scenario of global warming (RCP4.5). They argued that this decrease is mainly due to a reduction in the katabatic forcing induced by a weakening of the inversion layer temperature gradient, except during summer (see further in the text). Moreover, Franco et al. (2013) who used the MAR forced with CMIP5 large-scale models to project future changes in the GrIS surface melt found that the cloudiness might be enhanced over Greenland with higher temperatures. This is due to the fact that warmer air can contain more water vapor (Franco et al., 2013). As indicated in Section 2.2.1, the katabatic winds are influenced by the cloud cover. If the latter was to be reduced, this would lead to a further weakening of the katabatic forcing. The difference between the wind speed decrease projected by Gorter et al. (2013) over the GrIS and by the CMIP6-forced MAR simulations is

of approximately 0.1 m/s. These differences most probably come from the fact that a milder radiative forcing scenario was used by Gorter et al. (2013) (+4.5 W/m² by 2100) compared with this study (+8.5 W/m² by 2100).

Gorter et al. (2013) also found that along the ice sheet margins, the wind speed is expected to increase over time. This is consistent with the results from Section 5.2.3.1 where two areas along the coasts were found to have a positive wind speed cumulated trend over the period 2021-2100. This is coherent with the expected stronger barrier winds at the ice sheet edges driven by an enhanced thermal contrast between the tundra and the GrIS (Franco et al, 2013). The extent of these bands of increased wind speed are however somewhat different between the projections of Gorter et al. (2013) and the projections of this work. These bands extend further to the south for Gorter et al. (2013).

Moreover, on a seasonal basis, it emerges from Section 5.2.3.2 that the winter mean wind speed is expected to decrease while the summer wind speed is expected to stay relatively constant (even to increase for some simulations). This might come from the fact that the surface temperature of the GrIS is limited to 0°C in summer due to the melting of ice and snow. With the rising of temperatures, the upper air layers would be consequently warmer therefore reinforcing the inversion layer temperature gradient and thus enhancing the katabatic forcing (Gorter et al., 2013). In winter, however, the higher temperature at the surface would lead to a weakened katabatic forcing as explained previously.

Finally, the fact that no significant trend was found over 1981-2020 compared with 2021-2100 might be explained by two reasons. Firstly, as said before, the future trends have been calculated on more data points than for the present. Assuming that the STD of the present time series stays consistent over time, the cumulated trends might have been significant if calculated over a longer period. Secondly, the temperature is projected to increase exponentially under the SSP5-8.5 scenario of the CMIP6 (Hofer et al., 2020). The temperature rising between 1981 and 2020 is thus smaller than that between 2021 and 2100. Assuming that the change in temperature affects the wind speed as suggested above, this would contribute to explain the stronger projected wind speed decrease over 2021-2100.

Chapter 6: Conclusion

6.1 General conclusions

This study was conducted in the context of the "global grid" that is aimed at building a worldwide interconnected power system. By linking regions with high renewable energy resources to one another, this would enable a reliable electricity supply in populated regions that experience resource intermittency and help the decarbonisation of the current system. As it has appeared that South Greenland has a complementary wind pattern with Europe, this region has gained increasing interest for wind farm development. Therefore, a good knowledge of the wind speed field is necessary in this area. Because it is a remote and observation scarce-region, there was a need to increase this wind field knowledge through the use of Regional Climate Models and the installation of new weather stations as was achieved with the ULiège Katabata project.

This work aimed at answering three remaining research questions concerning the wind field modelling over the southern tip of Greenland. The first objective was to validate the MAR model with *in situ* observations over the tundra where wind turbines are likely to be installed rather than over the GrIS (where MAR has already been validated by Delhasse et al. (2020)). This was done by comparing the MAR wind speed outputs with hourly observations from 10 weather stations from PROMICE, DMI and NOAA network from 2016, 2017, 2018, winter and summer. The outputs were also compared with the observation from the three AWS of the Katabata project from 2020. It appeared that the MAR wind speed is in general quite consistent with the observations. In general, the results show good correlation (R>70) with an exception for 2016 (but some stations seemed to have biased values for this year). Nonetheless the smoothing of the orography by the model leads to an overestimation of the wind speed that can be locally significant.

The second objective was to investigate the influence of the spatial resolution on MAR wind speed outputs. This was done by comparing the outputs generated at 5, 10, 15 and 20 km resolution with the observation from the same stations as for the first objective. Obviously, the results are in better agreement with finer resolutions because the complex topography features such as fjords are better resolved by the model than for coarser resolutions. For the reference

dataset, the increase of agreement between MAR and the stations is in general significant (difference in R >=0.05) when going from a 10 km to 5 km resolution compared with going from 20 km to 15 km. That is because at 15 km, this resolution is still too coarse in regard to the topographical features typical scale. For the Katabata stations, these differences in agreement between the different resolutions were less clear. The spatial resolution also seemed to have a greater impact in winter when wind speeds are higher but this is not very clear either.

Finally, the third objective was to analyse the present and future wind speed trends over the southern tip of Greenland. This was done by calculating the 1981-2020 and 2021-2100 trends on MAR simulations forced with an ensemble of five CMIP6 GCMs outputs under the emission scenario SSP5-8.5. These simulations were the same as in Hofer et al. (2020). The trends were calculated first on the spatially averaged data then in two dimensions. Before comparing the magnitude of the trends with their STD, an investigation of the wind speed distribution was conducted. On a monthly, yearly and seasonal scale, it can roughly be considered Gaussian. The wind speed trends could thus be compared with their associated STD to assess their significance. It turned out that for the present day, no significant trend could be found. The different simulations were also compared with a MAR simulation forced with ERA-5 as reference. They seemed to be fairly consistent although there were uncertainties between the different simulations.

For the future changes, it appeared that the southern tip of Greenland is likely to experience a general wind speed decrease of -0.43 m/s/80yr between 2021 and 2100 most probably due to a lower katabatic forcing over the GrIS induced by the projected increasing temperatures. This wind speed decrease is however less expected in summer. During this season, the katabatic forcing should not be weakened because the inversion layer temperature gradient is bound to be maintained by the fact that the surface temperature is kept at freezing point by the melting ice and snow. The upper layer would however be warmer and therefore conserve the strength of the inversion temperature gradient. Moreover, in contrast to the general future wind speed decrease, the edges of the GrIS and the tundra might experience stronger barrier wind due to an enhanced thermal forcing.

In terms of wind power production, the general wind speed decrease modelled between 2021-2100 is expected to cause a maximum wind power reduction. As was seen between 1981 and 2021, the mean maximum wind power has been reduced by 3.5 to 4.3 % over the study area.

This negative trend is likely to continue in the future. However, areas where barrier winds are expected to strengthen could in contrast be areas of increased maximum wind power.

6.2 Perspectives

In regard to this study, perspectives can be suggested for future work. Firstly, a more complete assessment of the monthly, yearly and seasonal wind speed means could be conducted. Although the data from this work seemed normally distributed, this might not be the case everywhere over Greenland. The normality of a distribution is however important to know in case a parametric statistical test needs to be used.

Secondly, as it was done for the present day, the future trends in air density and wind power would be interesting to evaluate as it is useful knowledge for wind farm developers. An analysis of the seasonal changes might be interesting as well, especially to investigate if the complementarity of wind regimes between Greenland and Europe will persist in the future. By the same token, this trend analysis would be useful to conduct for the wind direction as a change in this variable might significantly affect the wind speed over the complex Greenlandic tundra. A validation of the MAR wind direction outputs can therefore be suggested for future work as well.

References

Bilir, L., Imir, M., Devrim, Y. and Albostan, A. (2015). Seasonal and yearly wind speed distribution and wind power density analysis based on Weibull distribution function. *International Journal of Hydrogen Energy,* 40:15301-15310.

Bromwich, D. H., Cassano, J. J., Klein, T., Heinemann, G., Hines, K. M., Steffen, K. and Box, J. E. (2001). Mesoscale Modeling of Katabatic Winds over Greenland with the Polar MM5. *Monthly Weather Review,* 129:2290-2309.

Chatzivasileiadis, S., Ernst, D. and Anderssin, G. (2013). The Global Grid. *Renewable Energy,* 57:372-383.

da Silva Soares, J. P. (2016). *Wind Energy utilization in Arctic climate – RACMO 2.3 Greenland Climate Runs Project*. Master thesis, Uppsala University, Uppsala, Sweden.

Delhasse, A., Kittel, C., Amory, C., Hofer, S., van As, D., Fausto, R. S. and Fettweis, X. (2020). Brief communication: Evaluation of the near-surface climate in ERA5 over the Greenland Ice Sheet. *The Cryosphere,* 14:957-265.

De Ridder, K. and Gallée, H. (1998). Land surface-induced regional climate change in southern Israel. Journal of applied meteorology, 37(11):1470-1485.

DMI (2021)a. About meteorological observations. Danish Meteorological Institute. https://confluence.govcloud.dk/display/FDAPI/About+meteorological+observations. Last consulted on 10/07/2021.

DMI (2021)b. Parameters (metObs). Danish Meteorological Institute https://confluence.govcloud.dk/pages/viewpage.action?pageId=26476616. Last consulted on 10/07/2021.

Doyle, J. D. and Shapiro, M. A. (1999). Flow response to large-scale topography: the Greenland tip jet. *Tellus,* 51A:728-748.

Du Vivier, A. K. and Cassano, J. J. (2013). Evaluation of WRF Model Resolution on Simulated Mesoscale Winds and Surface Fluxes near Greenland. *Monthly Weather Review,* 141:941-963.

Ettema, J., van den Broeke, M. R., van Meijgaard, E., ven den Berg, W. J., Box, J. E. and Steffen, K. (2010)a. Climate of the Greenland ice sheet using a high-resolution climate model – Part 1: Evaluation. *The Cryosphere,* 4:511-527.

Ettema, J., van den Broeke, M. R., van Meijgaard, E. and van den Berg, W. J. (2010)b. Climate of the Greenland ice sheet using a high-resolution climate model – Part 2: Near-surface climate and energy balance. *The Cryosphere*, 4:529-544.

Eyring, V., Bony, S., Meehl, G. A., Senior, C. A., Stevens, B., Stouffer, R. J. and Taylor K. E. (2016). Overview of the Coupled Model Intercomparison Project Phase 6 (CMIP6) experimental design and organization. *Geoscientific Model Development*, 9:1937-1958.

Fausto, R.S. and van As, D., (2019). Programme for monitoring of the Greenland ice sheet (PROMICE): Automatic weather station data. Version: v03, Dataset published via Geological Survey of Denmark and Greenland. https://doi.org/10.22008/promice/data/aws

Fettweis, X. (2006). *Reconstruction of the 1979-2005 Greenland ice sheet surface mass balance using satellite data and the regional climate model MAR*. Ph.D. thesis, Université catholique de Louvain, Louvain-la-neuve, Belgium.

Fettweis, X., Gallée, H. and Lefebre, F. (2006). The 1988-2003 Greenland ice sheet melt extent using passive microwave satellite data and a regional climate model. *Climate Dynamics*, 27:531-541.

Fettweis, X. (2007). Reconstruction of the 1979-2006 Greenland ice sheet surface mass balance using the regional climate model MAR. *The Cryophere*, 1:21-40.

Fettweis, X., Box, J. E., Agosta, C., Amory, C., Kittel, C., Lang, C., van As, D., Machguth, H. and Gallée, H. (2017). Reconstructions of the 1900-2015 Greenland ice sheet surface mass balance using the regional climate MAR model. *The Cryosphere*, 11:1015-1033.

Franco, B., Fettweis, X. and Erpicum, M. (2013). Future projections of the Greenland ice sheet energy balance driving the surface melt. *The Cryosphere*, 7:1-18.

Franco, B., Fettweis, X., Lang, C. and Erpicum, M. (2016). Impact of spatial resolution on the modelling of the Greenland ice sheet surface mass balance between 1990-2010, using the regional climate model MAR. *The Cryosphere*, 6:695-711.

Gallée, H. and Schayes, G. (1994). Development of a Three-Dimensional Meso-γ Primitive Equation Model: Katabatic Winds Simulation in the Area of Terra Nova Bay, Antartica. *Monthly Weather Review*, 122:671-685.

Gallée, H. (1995). Simulation of the mesocyclonic activity in the Ross sea, Antarctica. *Monthly Weather Review*, 123(7):2051-2069.

Gallée, H., Guyomarc'h, G. and Brun, E. (2001). Impact Of Snow Drift On The Antarctic Ice Sheet Surface Mass Balance : Possible Sensitivity to Snow-Surface Properties. *Boundary-Layer Meteorology*, 99(1):1-19.

Gallée, H., Trouvilliez, A., Agosta, C., Genthon, C., Favier, V. and Naaim-Bouvet, F. (2013). Transport of Snow by the Wind : A Comparison Betwee, Observations in Adélie Land, Antarctica, and Simulations Made with the Regional Climate Model MAR. *Boundary-Layer Meteorology*, 146(1):133-147.

Ghasemi, A. and Zahediasl, S. (2012). Normality tests for statistical analysis: A guide for non-statisticians. *International Journal of Endocrinology and Metabolism*, 10(2):486-489.

Gorter, W., van Angelen, J. H., Lenaerts, J. T. M. and van den Broeke, M. R. (2013). Present and future near-surface wind climate of Greenland from high resolution climate modelling. *Climate Dynamics*, 42:1595-1611.

Grachev, A. A., Leo, L. S., Di Sabatino, S., Fernando, H. J. S., Pardyjak, E. R and Fairwall, C. W. (2016), *Boundary-Layer Meteorology*, 159:469-494.

Güner, B., Frankford, M. T. and Johnson, J. T. (2009). A Study of the Shapiro-Wilk Test for the Detection of Pulsed Sinusoidal Radio Frequency Interference. *IEEE Transactions on Geoscience and Remote Sensing*, 47(6):1745-1751.

Guillevic, M., Bazin, L., Landais, A., Kindler, P., Orsi, A., Masson-Delmotte, V., Blunier, T., Buchardt, S. L., Capron, E., Leuenberg, M., Martinerie, P., Prié, F. and Vinther, B. M. (2013). Spatial gradients of temperature, accumulation and δ^{18}O-ice in Greenland over a series of Dansgaard-Oeschger events. *Climate of the Past*, 9:1029-1051.

Hanna, E., Cappelen, J., Fettweis, X., Mernild, S. H., Mote, T. L., Mottram, R., Steffen, K., Ballinger, T. J. and Hall, R. (2021). Greenland surface air temperature changes from 1981 to 2019 and implications for ice-sheet melt and mass-balance changes. *International Journal of Climatology*, 41(1):E1336-E1352.

Harden, B. E., Renfrew, I. A. and Petersen, G. N. (2011). A Climatology of Wintertime Barrier Winds off Southeast Greenland. *Journal of Climate*, 24:4701-4717.

Harden, B.E. and Renfrew, I. A. (2012). On the spatial distribution of high winds off southeast Greenland. *Geophysical Research Letters*, 39:14806-14812.

Heinemann, G. and Klein, T. (2002). Modelling and observations of the katabatic flow dynamics over Greenland. *Tellus*, 54A:542-554.

Hersbach, H. et al. (2018). Operational global reanalysis: progress, future directions and synergies with NWP including updates on the ERA5 production status. ECMWF ERA Report Series. doi:10.21957/tkic6g3wm.

Hitz, S. and Smith, J. (2004). Estimating global impacts from climate change. *Global Environmental Change*, 14:201-218.

Ho, A. D. and Yu, C. C. (2015). Descriptive Statistics for Modern Test Score Distributions: Skewness, Kurtosis, Discreteness and Ceiling Effects. *Educational and Psychological Measurements*, 75(3): 365-388.

Hofer, S., Lang, C., Amory, C., Kittel, C., Delhasse, A., Tedstone, A. and Fettweis, X. (2020). Greater Greenland Ice Sheet contribution to global sea level rise in CMIP6. *Nature Communications*, 11:6289-6300.

IPCC (2021). *Climate Change 2021: The Physical Science Basis. Contribution of Working Group I to the Sixth Assessment Report of the Intergovernmental Panel on Climate Change* [Masson-Delmotte, V., P. Zhai, A. Pirani, S. L. Connors, C. Péan, S. Berger, N. Caud, Y. Chen, L. Goldfarb, M. I. Gomis, M. Huang, K. Leitzell, E. Lonnoy, J. B. R. Matthews, T. K. Maycock, T. Waterfield, O. Yelekçi, R. Yu and B. Zhou (eds.)]. Cambridge University Press. In Press

Jakobsen, K. R. (2016). *Renewable Energy Potential of Greeland with emphasis on wind resource assessment.* Ph.D. thesis, Technical University of Denmark, Roskilde, Denmark.

Jung, C. and Schindler, D. (2019). Changing wind speed distributions under future global climate. *Energy Conversion and Management*, 198:1111841.

Kim, H-Y. (2013). Statistical notes for clinical researchers: assessing normal distribution (2) using skewness and kurtosis. *Restorative Dentistry & Endodontics*, 38(1):52-54.

Laurila, T. K., Sinclair, V. A. and Gregow, H. (2021). Climatology, variability, and trends in near-surface wind speeds over the North Atlantic and Europe during 1979-2018 based on ERA5. *International Journal of Climatology*, 41:2253-2278.

Meehl, G. A., Senior, C. A., Eyring, V., Flato, G., Lamarque, J-F., Stouffer, R. J., Taylor K. E. and Schlund, M. (2020). Context for interpreting equilibrium climate sensitivity and transient climate response from the CMIP6 Earth system models. *Science Advances*, 6(26):eaba1981.

Moore, G. W. K. and Renfrew, I. A. (2005). Tip Jets and Barrier Winds: A QuickSCAT Climatology of High Wind Speed Events around Greenland. *Journal of Climate*, 18:3713-3725.

Moore, G. W. K. (2014). Mesoscale Structure of Cape Farewell Tip Jets. *Journal of Climate*, 27:8956-8965.

Moore, G. W. K., Renfrew, I. A., Harden, B. E and Mernild, H. (2015). The impact of resolution on the representation of southeast Greenland barrier winds and katabatic flows. *Geophysical Research Letters*, 42:3011-3018.

Mote, T. L. (1998). Mid-tropospheric circulation and surface melt on the Greenland ice sheet. Part II: Synoptic circulation. *International Journal of Climatology*, 18:131-145.

NOAA (2018). Federal climate complex data documentation for Integrated Surface Data (ISD). National Oceanic and Atmospheric Administration. https://www1.ncdc.noaa.gov/pub/data/noaa/isd-format-document.pdf

Olauson, J. (2018). ERA5: The new champion of wind power modelling? *Renewable Energy*, 126:322-331.

O'Neill, B. C., Tebaldi, C., van Vuuren, D. P., Eyring, V., Friedlingstein, P., Hurtt, G., Knutti, R., Kriegler, E., Lamarque, J-F., Lowe, J., Meehl, G. A., Moss, R., Riahi, K. and Sanderson, B. M. (2016). The Scenario Model Intercomparison Project (ScenarioMIP) for CMIP6. *Geoscientific Model Development*, 9:3461-3482.

Payne, A. J. et al. (2021). Future sea level change under CMIP5 and CMIP6 scenarios from the Greenland and Antarctic ice sheets. *Geophysical Research Letters*, doi:10.1029/2020GL091741.

Perron, M. and Sura, P. (2013). Climatology of Non-Gaussian Atmospheric Statistics. *Journal of Climate*, 26:1063-1083.

Przybylak, R. (2016). *The Climate of the Arctic.* 2nd ed. Springer International Publishing. Atmospheric and Oceanographic Science Library, vol. 52, 300 p. doi:10.1007/978-3-319-21696-6

Pickart, R.S, Våge, K., Moore, G.W.K., Renfrew, I.A., Ribergaard, M.H and Davies, H.C. (2008). Chapter 26: Convection in the Western North Atlantic Sub-Polar Gyre: Do Small-Scale Wind Events Matter? *in* Dickson, R.R, Meincke, J., Rhines, P. (eds.). *Arctic-Subarctic Ocean Fluxes: Defining the Role of the Northern Seas in Climate*. Dordrecht: Springer, p 629-652.

Radu, D., Berger, M., Fonteneau, R., Hardy, S., Fettweis, X., Le Du, M., Panciatici, P., Balea, L. and Ernst, D. (2019). Complementary assessment of south Greenland katabatic flows and West Europe wind regimes. *Energy*, 175 :393-401.

Renalysis.org (2010). Advancing reanalysis. http://reanalyses.org/. Consulted on 19/07/2021.

Serreze, M. C. and Francis, J.A. (2006). The Arctic on the fast track of change. *Weather*, 61(3):65-69.

Soares, P. M. M., Lima, D. C. A. and Nogueira M. (2020). Global offshore wind energy resources using new ERA-5 reanalysis. *Environmental Research Letters*, 15:1040a2.

Tedesco, M. and Fettweis, X. (2020). Unprecedented atmospheric conditions (1948-2019) drive the 2019 exceptional melting season over the Greenland ice sheet. *The Cryosphere*, 14:1209-1223.

van As, D., Fausto, R. S., Steffen, K., Ahlstrøm, A. P., Andersen, S. B., Andersen, M. L., Box, J. E., Charalampidis, C., Citterio, M., Colgan, W. T., Edelvang, K., Larsen, S. H., Nielsen, S., Veicherts, M. and Weidick, A. (2014). Katabatic winds and piteraq storms: observations from the Greenlandic ice sheet. *Geologic survey of Denmark and Greenland bulletin*, 31(31):83-86.

van den Berg, W. J. and Medley, B. (2016). Brief communication: Upper-air relaxation in RACMO2 significantly improves modelled interannual surface mass balance variability in Antarctica. *The Cryosphere*, 10(1):459-43.

van den Broeke, M. R., Duynkerke, P. G. and Oerlemans, J. (1994). The observed katabatic flow at the edge of the Greenland ice sheet during GIMEX-91. *Global and Planetary Change*, 9:3:15.

van den Broeke, M. R. and Gallée, H. (1996). Observation and simulation of barrier winds at the western margin of the Greenland ice sheet. *Meteorological Society*, 122:1365-1383.

van Vuuren, D. P., Edmonds, J., Thomson, A., Riahi, K., Kainuma, M., Matsui, T., Hurtt, G. C., Lamarque, J-F., Meinshausen, M., Smith, S., Granier, C., Rose, S. K. and Hibbard, K. A. (2011). The Representative Concentration Pathways: an overview. *Climatic Changes*, 109:5-31.

Appendix A: Correlation, Bias, RMSE and RMSEc tables between observations and MAR.

***Table A.1**: Correlation, RMSE (ms^{-1}), RMSEc (ms^{-1}) and mean bias (ms^{-1}) between the MAR and the observation for 2016*

		WINTER 2016				**SUMMER 2016**			
Stations	Parameters	GR5	GR10	GR15	GR20	GR5	GR10	GR15	GR20
ANG	CORREL	0.67	0.54	0.38	0.43	0.71	0.46	0.23	0.20
	RMSE	5.5	6.8	7.9	7.3	2.7	4.1	5.3	5.8
	RMSEc	5.1	6.3	7.5	6.8	2.7	4.0	5.2	5.5
	BIAS	2.0	2.5	2.2	2.7	0.2	0.7	1.2	1.8
FRE	CORREL	0.83	0.76	0.76	0.77	0.77	0.72	0.73	0.72
	RMSE	3.1	2.8	3.3	3.3	2.3	1.8	2.3	2.4
	RMSEc	2.3	2.7	2.7	2.7	1.6	1.6	1.7	1.8
	BIAS	2.1	0.6	1.9	2.0	1.5	0.8	1.5	1.5
IKM	CORREL	0.86	0.79	0.77	0.78	0.87	0.83	0.80	0.83
	RMSE	3.2	3.8	3.9	3.8	1.9	2.1	2.2	2.1
	RMSEc	3.0	3.5	3.7	3.6	1.8	2.1	2.2	2.1
	BIAS	1.2	1.5	1.4	1.3	-0.1	0.1	0.2	0.04
IKS	CORREL	0.88	0.87	0.88	0.89	0.92	0.88	0.88	0.89
	RMSE	4.7	4.5	4.2	4.1	3.0	3.7	3.3	3.4
	RMSEc	3.4	3.5	3.3	3.2	2.0	2.5	2.4	2.3
	BIAS	3.2	2.9	2.5	2.6	2.3	2.7	2.2	2.5
NAR	CORREL	X	X	X	X	X	X	X	X
	RMSE	X	X	X	X	X	X	X	X
	RMSEc	X	X	X	X	X	X	X	X
	BIAS	X	X	X	X	X	X	X	X
NUN	CORREL	0.88	0.80	0.76	0.77	0.89	0.85	0.84	0.83
	RMSE	3.0	3.7	3.9	4.0	1.7	2.0	2.1	2.2

	RMSEc	2.8	3.4	3.7	3.7	1.6	1.9	2.0	2.0
	BIAS	-1.2	-1.4	-1.4	-1.7	-0.4	-0.7	-0.7	-0.8
QAS_L	CORREL	0.86	0.83	0.81	0.76	0.56	0.56	0.50	0.50
	RMSE	2.2	2.8	2.7	3.3	1.8	1.8	1.9	1.8
	RMSEc	2.2	2.7	2.7	2.9	1.6	1.7	1.8	1.7
	BIAS	-0.1	0.8	0.5	1.4	-0.8	-0.7	-0.8	-0.8
QAS_M	CORREL	X	X	X	X	X	X	X	X
	RMSE	X	X	X	X	X	X	X	X
	RMSEc	X	X	X	X	X	X	X	X
	BIAS	X	X	X	X	X	X	X	X
QAS_U	CORREL	0.89	0.85	0.82	0.81	0.80	0.77	0.76	0.75
	RMSE	3.0	3.2	2.9	2.9	1.4	1.4	1.5	1.2
	RMSEc	2.3	2.6	2.5	2.6	1.1	1.1	1.1	1.2
	BIAS	2.0	1.7	1.4	1.3	0.9	0.9	0.9	0.2
UKI	CORREL	0.84	0.72	0.71	0.66	0.59	0.57	0.57	0.55
	RMSE	2.4	3.2	3.2	3.4	2.7	2.5	2.8	2.7
	RMSEc	2.4	3.1	3.1	3.4	2.4	2.4	2.5	2.5
	BIAS	-0.1	-0.7	-0.4	-0.4	1.2	0.7	1.2	1.0

***Table A.2**: Correlation, RMSE (ms^{-1}), RMSEc (ms^{-1}) and mean bias (ms^{-1}) between the MAR and the observation for 2017*

		WINTER 2017				**SUMMER 2017**			
Stations	Parameters	GR5	GR10	GR15	GR20	GR5	GR10	GR15	GR20
ANG	CORREL	0.84	0.68	0.47	0.52	0.82	0.71	0.57	0.57
	RMSE	3.4	5.0	6.7	6.1	2.4	3.1	3.6	3.7
	RMSEc	3.4	4.9	6.6	5.9	2.4	3.0	3.6	3.7
	BIAS	0.4	0.1	0.8	1.3	0.3	0.2	-0.3	0.3
FRE	CORREL	0.83	0.76	0.74	0.76	0.74	0.70	0.65	0.64
	RMSE	3.3	3.0	3.6	3.5	2.5	2.1	2.8	2.8

	RMSEc	2.4	2.8	2.9	2.8	1.9	1.9	2.2	2.2
	BIAS	2.3	1.0	2.1	2.2	1.7	0.9	1.6	1.6
IKM	CORREL	0.81	0.74	0.72	0.76	0.82	0.75	0.74	0.72
	RMSE	3.0	3.5	3.7	3.5	1.8	2.1	2.2	2.3
	RMSEc	2.9	3.4	3.5	3.3	1.8	2.1	2.2	2.3
	BIAS	0.6	1.0	1.2	1.2	0.1	0.02	0.3	0.2
IKS	CORREL	0.87	0.86	0.87	0.86	0.88	0.84	0.83	0.82
	RMSE	4.6	4.9	4.4	4.4	3.0	3.3	3.0	3.2
	RMSEc	3.3	3.4	3.1	3.2	2.1	2.3	2.2	2.3
	BIAS	3.2	3.5	3.1	2.9	2.2	2.4	2.1	2.2
NAR	CORREL	X	X	X	X	X	X	X	X
	RMSE	X	X	X	X	X	X	X	X
	RMSEc	X	X	X	X	X	X	X	X
	BIAS	X	X	X	X	X	X	X	X
NUN	CORREL	0.92	0.87	0.85	0.85	0.91	0.88	0.86	0.86
	RMSE	3.0	3.7	4.0	4.1	1.8	2.1	2.2	2.2
	RMSEc	2.7	3.2	3.4	3.4	1.8	2.0	2.2	2.1
	BIAS	-1.5	-2.0	-2.1	-2.3	-0.2	-0.6	-0.4	-0.6
QAS_L	CORREL	0.82	0.78	0.76	0.73	0.57	0.56	0.53	0.52
	RMSE	2.3	2.6	2.6	2.8	1.5	1.6	1.6	1.6
	RMSEc	2.3	2.5	2.6	2.7	1.5	1.6	1.6	1.6
	BIAS	0.1	0.3	0.2	0.7	0.1	0.3	0.2	0.04
QAS_M	CORREL	X	X	X	X	X	X	X	X
	RMSE	X	X	X	X	X	X	X	X
	RMSEc	X	X	X	X	X	X	X	X
	BIAS	X	X	X	X	X	X	X	X
QAS_U	CORREL	0.85	0.82	0.79	0.77	0.82	0.80	0.79	0.77
	RMSE	2.6	2.5	2.5	2.5	1.6	1.5	1.6	1.3
	RMSEc	1.8	2.0	2.1	2.2	1.2	1.3	1.3	1.3
	BIAS	1.8	1.5	1.3	1.2	1.0	0.9	0.9	0.2

UKI	CORREL	0.87	0.80	0.76	0.71	0.82	0.76	0.78	0.73
	RMSE	2.4	3.0	3.2	3.5	1.8	2.1	2.0	2.2
	RMSEc	2.4	2.9	3.1	3.4	1.8	2.0	2.0	2.2
	BIAS	-0.3	-0.7	-0.4	-0.8	0.3	-0.4	0.1	-0.1

***Table A.3**: Correlation, RMSE (ms^{-1}), RMSEc (ms^{-1}) and mean bias ms^{-1}) between the MAR and the observation for 2018*

		WINTER 2018				**SUMMER 2018**			
Stations	Parameters	GR5	GR10	GR15	GR20	GR5	GR10	GR15	GR20
ANG	CORREL	0.85	0.76	0.60	0.67	0.84	0.75	0.59	0.61
	RMSE	3.5	4.4	5.5	4.8	2.5	3.0	3.9	3.8
	RMSEc	3.4	4.4	5.5	4.8	2.5	3.0	3.9	3.8
	BIAS	0.8	0.4	-0.01	0.7	-0.2	-0.2	-0.7	-0.1
FRE	CORREL	0.83	0.78	0.79	0.77	0.84	0.76	0.76	0.75
	RMSE	3.0	2.6	3.2	3.6	2.6	2.2	2.7	2.7
	RMSEc	2.2	2.4	2.4	2.5	1.9	2.0	2.2	2.2
	BIAS	2.0	1.0	2.2	2.5	1.7	1.0	1.7	1.6
IKM	CORREL	0.85	0.78	0.78	0.78	0.87	0.79	0.74	0.76
	RMSE	3.3	4.2	4.2	4.2	1.9	2.4	2.6	2.5
	RMSEc	3.3	3.9	3.9	4.0	1.9	2.4	2.6	2.5
	BIAS	0.6	1.5	1.4	1.4	-0.1	-0.2	0.03	-0.3
IKS	CORREL	X	X	X	X	X	X	X	X
	RMSE	X	X	X	X	X	X	X	X
	RMSEc	X	X	X	X	X	X	X	X
	BIAS	X	X	X	X	X	X	X	X
NAR	CORREL	0.89	0.87	0.82	0.82	0.88	0.84	0.84	0.81
	RMSE	2.3	2.4	3.7	2.9	1.6	1.8	2.1	1.8
	RMSEc	2.1	2.3	2.8	2.6	1.5	1.7	1.9	1.2

	BIAS	0.7	0.5	2.3	1.3	0.5	0.6	0.9	0.2
NUN	CORREL	0.90	0.88	0.87	0.85	0.91	0.90	0.88	0.88
	RMSE	3.3	3.7	3.8	4.1	2.1	2.4	2.5	2.6
	RMSEc	2.9	3.1	3.3	3.5	2.0	2.1	2.2	2.2
	BIAS	-1.4	-1.9	-2.0	-2.1	-0.8	-1.3	-1.2	-1.4
QAS_L	CORREL	0.79	0.77	0.73	0.61	0.82	0.80	0.79	0.78
	RMSE	2.4	2.5	2.6	3.7	1.5	1.8	1.7	1.7
	RMSEc	2.3	2.5	2.6	3.3	1.5	1.7	1.7	1.7
	BIAS	-0.3	0.2	-0.1	1.5	-0.01	0.3	0.04	-0.1
QAS_M	CORREL	0.76	0.72	0.69	0.66	0.82	0.81	0.76	0.72
	RMSE	2.7	2.8	2.8	2.9	1.6	1.6	1.9	1.7
	RMSEc	2.5	2.7	2.7	2.8	1.5	1.6	1.8	1.7
	BIAS	0.9	0.8	0.7	0.4	0.4	0.4	0.5	0.01
QAS_U	CORREL	0.87	0.82	0.79	0.76	0.86	0.84	0.84	0.83
	RMSE	2.3	2.4	2.4	2.8	1.8	1.8	1.7	1.5
	RMSEc	1.8	2.2	2.2	2.6	1.4	1.5	1.5	1.5
	BIAS	1.4	0.9	0.8	1.0	1.0	0.9	0.9	0.2
UKI	CORREL	0.84	0.77	0.76	0.69	0.88	0.81	0.82	0.80
	RMSE	2.5	2.9	3.0	3.4	1.7	2.1	2.1	2.2
	RMSEc	2.4	2.9	2.9	3.3	1.7	2.0	2.0	2.2
	BIAS	-0.5	-0.5	-0.4	-0.7	0.02	-0.5	0.1	-0.2

***Table A.4**: Mean wind speed and STD per station, per year and season*

		WINTER		**SUMMER**	
		Mean (ms^{-1})	STD (ms^{-1})	Mean (ms^{-1})	STD (ms^{-1})
2016	ANG	9.7	5.8	5.4	3.4
	FRE	5.3	3.8	3.5	1.9
	IKM	8.5	5.7	5.3	3.6
	IKS	10.3	6.9	5.8	4.9
	NAR	X	X	X	X
	NUN	11.7	5.7	6.8	3.6
	QAS_L	6.7	3.9	4.1	1.8
	QAS_M	X	X	X	X
	QAS_U	7.4	3.8	3.8	1.6
	UKI	7.1	4.4	3.6	2.9
2017	ANG	9.1	6.1	6.1	3.9
	FRE	5.6	3.9	3.8	2.2
	IKM	6.8	5.0	4.6	3.1
	IKS	8.4	6.2	4.6	3.7
	NAR	X	X	X	X
	NUN	12.1	6.3	7.3	4.2
	QAS_L	6.1	3.8	3.2	1.5
	QAS_M	X	X	X	X
	QAS_U	5.8	3.0	3.7	1.9
	UKI	8.0	4.8	4.9	3.1
2018	ANG	9.8	6.0	7.2	4.3
	FRE	5.4	3.6	4.3	2.8
	IKM	8.2	6.2	5.2	3.8
	IKS	X	X	X	X
	NAR	3.9	4.4	3.4	2.9
	NUN	12.4	6.4	8.7	4.6
	QAS_L	6.0	3.7	3.8	2.5
	QAS_M	7.3	3.0	4.2	2.2
	QAS_U	7.0	3.3	4.0	2.5
	UKI	7.4	4.5	5.9	3.5

Appendix B: Mean maximum wind power between 1981 and 2020.

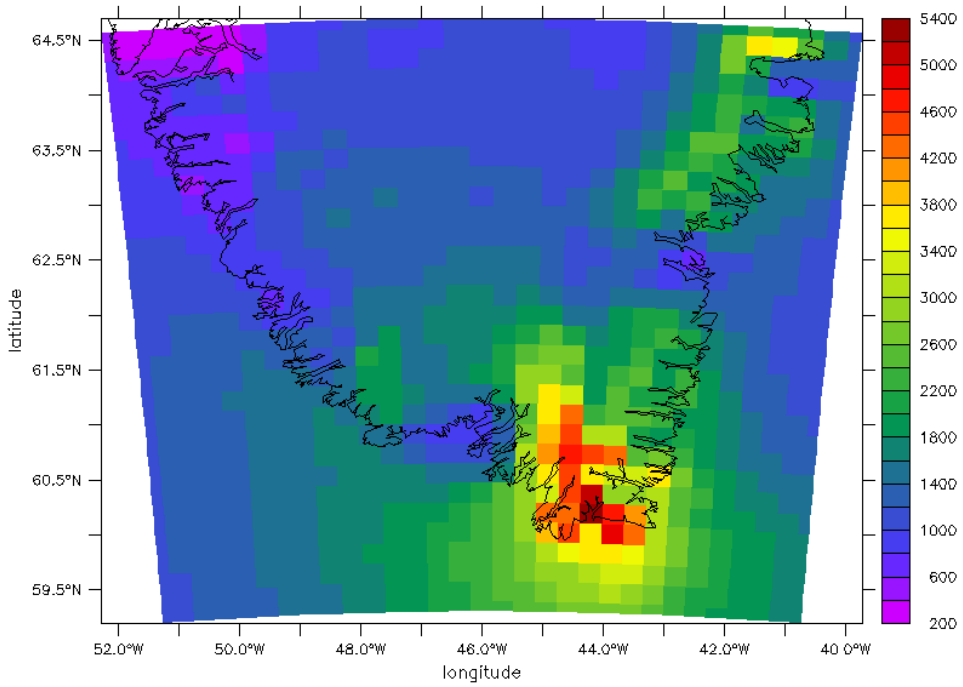

***Figure B.1**: Mean maximum wind power between 1981 and 2020 in W.*

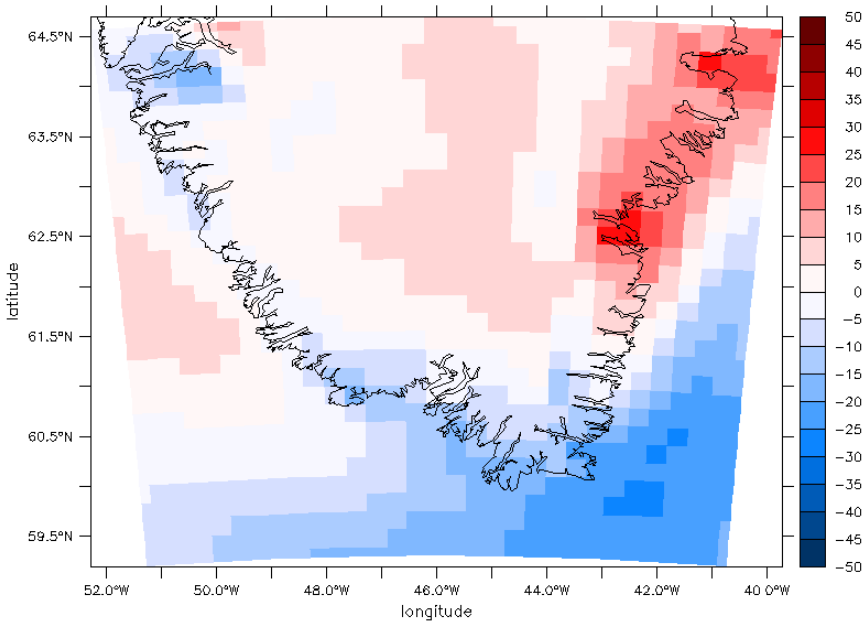

***Figure B.2**: Percentage of wind power change between 1981 and 2020 in regard to Figure B.1*